Electronic properties of the topological insulators Bi_2Se_3 and Bi_2Te_3

A

D I S S E R T A T I O N

prepared within a joint doctoral supervision agreement
(convention de cotutelle de thése)

submitted to the Victoria University of Wellington
in fulfilment of the requirements for the degree of

Doctor of Philosophy

AND

approved by the Faculty of Physics and Earth Sciences, Leipzig University,
in fulfilment of the requirements for the degree of

doctor rerum naturalium

Dr. rer. nat.

submitted by

M. Sc. Robin Gühne

born 5th February 1986 in Karl-Marx-Stadt

Examiners: Prof. Dr. Ulrich Zuelicke
Prof. Dr. Xiaolin Wang
Prof. Dr. Jan Meijer

Victoria University of Wellington
Leipzig University (date of conferment: 18th November 2019)
2020

Bibliographical Description
Guehne, Robin
Electronic properties of the topological insulators Bi_2Se_3 and Bi_2Te_3
Victoria University of Wellington, Leipzig University, Dissertation
148 P.*, 109 Ref.*, 46 Fig. (+4 in appendix), 8 Tab. (+1 in appendix), 1 appendix

Abstract
The three-dimensional topological insulators Bi_2Se_3 and Bi_2Te_3 are model systems of a new class of materials with an insulating bulk and gapless surface states. Their small band gaps and the heavy elements are essential for the topologically non-trivial band structure, but these features are similarly responsible for other remarkable properties, such as their high thermoelectric performance.

This thesis investigates the electronic properties of the topological insulators Bi_2Se_3 and Bi_2Te_3 with a broad range of experimental methods. Ferromagnetism in Mn doped Bi_2Te_3 is shown to disappear under sample sintering. A surprisingly large magnetoresistance and a charge carrier independent change in the sign of the thermopower with increasing Mn content are discussed. ^{125}Te nuclear magnetic resonance (NMR) of Bi_2Te_3 single crystals suggest an unusual electronic spin susceptibility and complex NMR shifts. The quadrupole interaction of ^{209}Bi nuclei in Bi_2Se_3 single crystals is shown to be a signature of the band inversion in quantitative agreement with first-principle calculations. Furthermore, it is proposed that the strong spin-orbit coupling of conduction electrons causes a non-trivial orientation dependent quadrupole splitting of the ^{209}Bi resonance.

Referat
Die drei-dimensionalen Topologische Isolatoren Bi_2Se_3 and Bi_2Te_3 sind Modell-Systeme einer neuen Klasse von Isolatoren mit metallischen Oberflächenzuständen. Ihre kleinen Bandlücken und die schweren Elemente sind essentiell für die topologisch nicht-triviale Bandstruktur, sind aber ebenso verantwortlich für andere bemerkenswerte Eigenschaften, wie etwa für ihre Leistungsfähigkeit als Thermoelektrika.

Diese Arbeit untersucht die elektronischen Eigenschaften der Topologischen Isolatoren Bi_2Se_3 und Bi_2Te_3 mittels zahlreicher experimenteller Methoden. Es wird gezeigt, dass Ferromagnetismus in Mn gedoptem Bi_2Te_3 durch sintern unterdrückt werden kann. Zudem werden ein überraschend großer Magnetoresistiver Effekt und ein ladungsträgerunabhängiger Vorzeichenwechsel des Seebeck-Koeffizienten mit zunehmenden Mn Gehalt diskutiert. Kernmagnetische Resonanz (NMR) von ^{125}Te Kernen in Bi_2Te_3 Einkristallen lässt auf eine ungewöhnliche elektronische Spin-Suszeptibilität and komplexe NMR Verschiebungen schließen. Es wird gezeigt dass die Quadrupolwechselwirkung von ^{209}Bi Kernen in Bi_2Se_3 Einkristallen eine Signatur der Bandinversion ist, in quantitativer Übereinstimmung mit DFT Rechnungen. Weiterhin wird argumentiert dass die starke Spin-Bahn Kopplung der Leitungselektronen zu einer nicht-trivialen Orientierungsabhängigkeit der ^{209}Bi Quadrupolaufspaltung führt.

*... P. (total number of pages)
... Ref. (Number of references in bibliography)

Acknowledgement

The present work would not have been possible without the help and support of a wide range of people. First and foremost I want to thank my supervisors Jürgen Haase, Grant Williams, and Shen Chong, who gave me this opportunity of an joint research program and guided me through the various difficulties arising from such a delicate endeavour as a PhD program in two different countries.

I am grateful to the MQF research group, in particular, my thanks go to Nataliya Georgieva, Michael Jurkutat, Gert Klotzsche, Jonas Kohlrautz, Steven Reichardt, Felix Höfer, Jakob Nachtigal for their help with NMR experiments, fruitful discussions, and memorable non-scientific activities. I also want to thank Marko Bertmer and Andreas Pöppl, as well as Henry Auer.

Similarly, I am grateful for the help of people from the Robinson Research Institute and from Callaghan Innovation. Especially, my gratitude goes to Martin Ryan, David Uhrig, and Gabriel Bioletti.

In the course of this project, I benefited a lot from discussions and the collaboration with a number of researchers. For their help, I would like to thank Jorge Ramírez-Ruiz and Ion Garate, Vŏtech Chlan, Ben Mallet, and Bob Buckley.

For their help to overcome administrative obstacles connected with a joint PhD program at two Universities, I would like to thank Susan Baeumler, Alexander Weber, and Petrik Galvosas.

I thank my parents and my brother for their support throughout the years. Equally, I would like to thank friends from both hemispheres, who always had a warm welcome for me.

I thank you, Henni, for going with me through this most challenging part of my live.

I acknowledge the funding from The MacDiarmid Institute for Advanced Materials and Nanotechnology. Similarly, I thank Leipzig University and the Deutsche Forschungsgemeinschaft for financial support.

Contents

List of Figures

List of Tables

List of abbreviations

ACT	Alternating current transport
ARPES	Angle-resolved photoemission spectroscopy
BR	Bloembergen-Rowland
CT	Central transition
DFT	Density functional theory
EFG	Electric field gradient
EPR	Electron paramagnetic resonance
FID	Free induction decay
FM	Ferromagnetic
FWHM	Full width at half maximum
HE	Hahn echo
MAS	Magic angle spinning
MPMS	Magnetic Property Measurement System
MR	Magnetoresistance
NIST	National Institute of Standards and Technology
NMR	Nuclear magnetic resonance
QL	Quintuple layer
PAS	Principle axes system
PDF	Powder diffraction file
PPMS	Physical Property Measurement System
RKKY	Ruderman-Kittel-Kasuya-Yoshida
SE	Solid echo
SNR	Standard reference material
SOC	Spin-orbit coupling
TKNN	Thouless-Kohmoto-Nightingale-den Nijs
TMS	Tetramethylsilane
TTO	Thermal transport option
WAL	Weak anti-localisation
XRD	X-ray diffraction
ZT	Figure of merit

Introduction

The discovery of topological phases of matter has sparked great interest in the scientific community [1–3]. Topological effects were thought to be referring to special quantum states of matter, realised in a few real systems. The existence of three-dimensional topological insulators that were predicted only ten years ago [4–7] and confirmed in strongly spin-orbit coupled systems with inverted band structures [8–11], marks a turning point. Since then, a whole variety of new topological states of matter have been identified. Today, there are topological superconductors, Dirac semi-metals including Weyl semi-metals, topological crystalline insulators and topological Kondo insulators [12]. Beyond the value for fundamental solid state physics, the expected applications of topological materials are numerous, ranging from modern spintronic and thermoelectric devices to superconductors and quantum computers.

Consequently, the theoretical understanding of topological phases of matter and mutual fertilisation with experimental research has grown to a central object in modern solid state physics. To this end, the investigation of topological properties of matter has created another branch of condensed matter physics fusing the research of fundamental quantum effects and materials science.

In general, topological states of matter feature a topologically non-trivial band structure, established by an odd number of inversions of bands with opposite parity. Such a band inversion gives rise to special bands with linear dispersion that cross the band gap. In topological insulators, these so-called Dirac cones appear at the interface to a trivial insulator, e.g. vacuum. In case of Dirac and Weyl semimetals, they are found in the bulk, and the two classes are distinguished by whether the Dirac cone remains two-fold degenerate or is symmetrically split[1] into its two constituent bands with opposite chirality. These additional bands host states that are described by the Dirac equation in the limit of a vanishing mass. This means elementary quantum states, i.e. massless Dirac fermions that are known from quantum field theory, can be researched directly in certain solids. Topological non-trivial states of

[1] Assuming same $\boldsymbol{k}$-values with opposite sign.

matter further nurture hopes of a realisation of Majorana states [13].

In the particular field of three dimensional topological insulators, Bi_2Se_3 and Bi_2Te_3 emerged as model representatives. Their bulk band structure is inverted at the Γ-point which essentially means a reversed order of bonding and anti-bonding states across the energy gap near the centre of the Brillouin zone. The corresponding negative band gap has no direct consequences for the physical properties of these materials which where known and researched already for decades. However, with the development of the language of topology applied to the concept of energy band structures in solids, one became aware of the subtle properties of the corresponding surface states. They are in fact the manifestation of the non-trivial band structure which thus is said to protect them topologically. In other words, they cannot be removed as long as their origin, the band inversion, remains intact.

These surface states possess a number of promising properties. The surface bands cross the band gap and thus, the surface states are gapless, or metallic. Hence, topological insulators are referred to as materials with an insulating bulk and a conducting surface. The surface states are further said to be spin-momentum locked which protects them from back-scattering,[2] an important property for future applications.

Real representations of essentially all three dimensional topological insulators, however, show frustratingly low resistivities that reflect a large number of free carriers due to the systems' high tendency to have native defects [14]. Consequently, studying the transport properties of the surface states of Bi_2Se_3 or Bi_2Te_3 is very complicated. On the other hand, the simplicity of the topology of systems like Bi_2Se_3, i.e. their single Dirac cone and the comparatively large energy gaps of up to $\sim 300\,\mathrm{meV}$, as well as the robustness of their surface states still cause a strong desire to study them nonetheless. A local probe like nuclear magnetic resonance (NMR) might be a powerful tool to study surface states, because the signal from nuclei near the boundary must be very different from the signal representing the bulk. However, in general the rather low sensitivity of NMR requires a high number of nuclei in the surface region for a measurable signal. Therefore, surface states of any kind cannot be probed with NMR in macroscopic single crystals. Only a sufficient quantity of nanoparticles will allow an experimental access to topological surface states by means of NMR, because of their high surface-to-volume ratio. Well defined nanoparticles, however, can be very difficult to synthesize and other effects such as changes in the energy band structure due to quantum confinement have to

[2] This is connected with the *chirality* of the surface states or their *spin texture* which means that the electronic spin and its momentum are in a locked perpendicular orientation to each other.

be taken into account.

Apart from first signatures from the surface states measured in nano-grained powders, a remarkable result of the few NMR studies of topological insulators – just fifteen publications in ten years [15–29] – is that the bulk NMR of Bi_2Se_3 and Bi_2Te_3 is surprisingly rich, and most of those features are still lacking proper understanding. Or, in other words, the NMR bulk states of Bi_2Se_3 and Bi_2Te_3 already presents a worthwhile but challenging exercise even beyond the need for being understood as a prerequisite for studying the NMR of the surface states.

The current project is based on a long-standing collaboration between the Felix Bloch Institute in Leipzig, Germany[3] and the MacDiarmid Institute in Wellington, New Zealand.[4] This work documents a comprehensive study of three dimensional topological insulators from single crystal syntheses and basic characterisation to the application of numerous advanced techniques, including magnetic susceptibility, transport, and NMR measurements.

The investigation of a broad spectrum of phenomena observed in macroscopic samples of the topological insulators Bi_2Se_3 and Bi_2Te_3 is documented. The main findings comprise the loss of ferromagnetic ordering in Mn doped Bi_2Te_3 after grinding and sintering, a surprisingly strong but doping-independent magentoresistance found in the same samples, and a carrier independent change in sign of the thermopower with increasing Mn content. All these effects are argued to be critically dependent on the presence of defects such as antisite disorder and vacancies.

^{125}Te NMR in Bi_2Te_3 single crystals provides clear evidence of an unusual strong indirect nuclear coupling very similar to what was found for Bi_2Se_3. The quadrupole coupling experienced by ^{209}Bi nuclei in Bi_2Se_3 is shown to be a real-space signature of the topologically non-trivial energy band structure. An orientation independent quadrupole splitting of ^{209}Bi in Bi_2Se_3 single crystals further suggests that the local electronic structure is to some extent tied to the external magnetic field via the strong spin-orbit coupling instead of reflecting the symmetries of the crystal lattice.

[3]Felix Bloch Institute for Solid State Physics, Leipzig University, Leipzig, Germany.

[4]MacDiarmid Institute for Advanced Materials and Nanotechnology, Robinson Research Institute, Victoria University of Wellington, Wellington, New Zealand.

The work is organised as follows:

Chapter 1 Topological insulators in three dimensions

Provides a brief overview of the historical developments that led to the discovery of three dimensional topological insulators. A general discussion of the chemical and physical properties of Bi_2Se_3 and Bi_2Te_3 follows, including an introduction of the concepts of band inversion and the thus emerging surface states. The chapter is closed by a comprehensive review of relevant literature that provide the basis of this thesis.

Chapter 2 Theoretical background

Provides theoretical basics for electronic properties and magnetism in condensed matter. Fundamental concepts of nuclear magnetic resonance (NMR) and the most common interactions encountered in solids are introduced.

Chapter 3 Methods I: structural, electronic, and magnetic properties

Comprises the preparation for powder X-ray diffraction (XRD), details of the experimental setup for the investigation of transport properties of a given material using a Physical Property Measurement System (PPMS), as well as the corresponding sample preparation. The working principle of a Magnetic Property Measurements System (MPMS) is introduced, and the mounting of samples.

Chapter 4 Methods II: nuclear magnetic resonance

Provides an overview of the method of nuclear magnetic resonance (NMR). The chapter summarizes details of how the numerous components of an NMR spectrometer are adjusted to ensure optimal experimental results with focus on the resonance circuit and the sample. NMR pulse sequences as well as the way the NMR shift can be determined are discussed.

Chapter 5 Sample preparation and basic characterisation

Reports first experimental results. The synthesis of single crystalline samples is discussed, followed by powder XRD measurements. The results from Hall effect measurements are presented. The chapter is closed by a tabular overview of all the samples investigated within this work, including basic properties such as lattice parameters and carrier concentration.

Chapter 6 Magnetic and electronic properties of Mn doped Bi_2Te_3 Measurements of the magnetic properties of pure and Mn doped Bi_2Te_3 single crystals are reported. The results are compared with those obtained from sintered powders and the influence of defects on the magnetism is discussed. Transport properties of sintered samples of pure and Mn doped Bi_2Te_3 are reported as obtained from resistivity, Hall effect, thermopower, and magnetoresistance measurements. The results are discussed in the light of potential effects induced by the defect chemistry of the present system.

Chapter 7 NMR of spin 1/2 nuclei: ^{125}Te in Bi_2Te_3

A detailed NMR documentation of ^{125}Te in Bi_2Te_3 single crystals is presented. The study comprises orientation dependent single crystal spectra of the two Te signals, their crystal site assignment, the corresponding powder spectra, as well as their NMR linewidths as function of the external magnetic field. The results are discussed with respect to theoretical calculations of the NMR shift in topological insulators and an indirect internuclear coupling that gives rise to extensive NMR line broadening.

Chapter 8 NMR of qaudrupole nuclei: ^{209}Bi in Bi_2Se_3

Provides a comprehensive study of the quadrupole effects observed through ^{209}Bi NMR in Bi_2Se_3 single crystals. The study comprises a variety of measurements including single crystal spectra, spectral changes due to transverse relaxation, transition selective nutation and T_2 measurements, as well as crystal orientation dependent spectra. The results are discussed on a general level and in their relation to the literature. The relationship between quadrupole interaction and the band inversion of the energy band structure of Bi_2Se_3 is analysed. The unusual orientation independent quadrupole splitting is reviewed in the context of a strongly spin-orbit coupled electronic system that sets the quantisation axis of the electric field gradient (EFG) seen by ^{209}Bi nuclei.

Conclusion and outlook

General conclusions will be drawn from the main experimental results discussed in Chs. 6, 7, and 8. It is shown how bulk properties as investigated in Ch.6 are related to the results obtained from NMR as a local probe. On this basis, potential research questions for future projects are discussed.

Chapter 1

Topological insulators in three dimensions

1.1 General understanding

Three-dimensional insulators define a class of materials featuring an insulating bulk with a metallic surface. Behind this rather simple picture of a material hides a sophisticated theoretical approach that changed the game in solid state physics during the last decades. Theoretical research and constant experimental verification go back to the 1970ies and in particular to 1980 when Klitzing et al. [30] discovered the integer quantum Hall effect in a 2-dimensional semiconductor under application of a strong magnetic field. Today, this quantum Hall system could be seen as the first topological insulator featuring a gapped energy spectrum (Landau quantisation) and gapless surface states [12].

There are numerous publications that work out the theoretical details connected with topology in solid state physics. Also, a number of comprehensive textbooks that concern topological insulators and related topics are available today [31–33]. However, as this field of research is ever changing, consulting recent research articles is strongly advised.

This thesis is focussed on the experimental investigation of bulk properties of the topological insulators Bi_2Se_3 and Bi_2Te_3. A brief timeline towards three-dimensional topological insulators along historical developments of central concepts and experimental cornerstones is provided next. It chiefly follows the review article by Ando [12].

Milestones towards topological insulators in three dimensions

1980 Discovery of integer quantum Hall effect [30].

1982 Realising the non-trivial nature of the $\boldsymbol{k}$-space of the quantum Hall system, introducing the topological invariant *TKNN*[1] or *Chern number* by Thouless et al. [34].

2004 Confirmation of the *spin Hall effect* [35].

2004-6 Proposals for *spin Hall* [36] and *quantum spin Hall* insulators [37–39], including the model material graphene with spin-orbit interaction [37].

2005 Introduction of the Z_2 formalism by Kane and Mele [38] which paved the way towards the understanding and realisation of insulators with a topologically non-trivial band structure.

2006/7 First two-dimensional topological insulator CdTe/HgTe/CdTe quantum wells proposed by Bernevig et al. [40] and experimentally confirmed by König et al. [41].

2006/8 First three-dimensional topological insulator $Bi_{1-x}Sb_x$ predicted by Fu and Kane [42] and confirmed by Hsieh et al. [8].

2009 Single Dirac-cone stoichiometric 3-dimensional topological insulator systems Bi_2Se_3, Bi_2Te_3, and Sb_2Te_3 were predicted by Zhang et al. [7] and verified by Xia et al. [9], Chen et al. [10], and Hsieh et al. [11].

1.2 Bismuth selenide and bismuth telluride

Structural properties

A number of chemical properties of Bi_2Se_3 and Bi_2Te_3 will first be introduced as they are crucial in the context of experimentally accessible real-space features and their relation to the topologically non-trivial band structure.

Fig.1.1 shows the crystal structure of Bi_2Se_3 and Bi_2Te_3. Both materials are isostructural, sharing the rhombohedral crystal structure with space group D_{3d}^5 ($R\bar{3}m$) differing only in their lattice parameters. The central building block is a

[1] Thouless-Kohmoto-Nightingale-and den Nijs

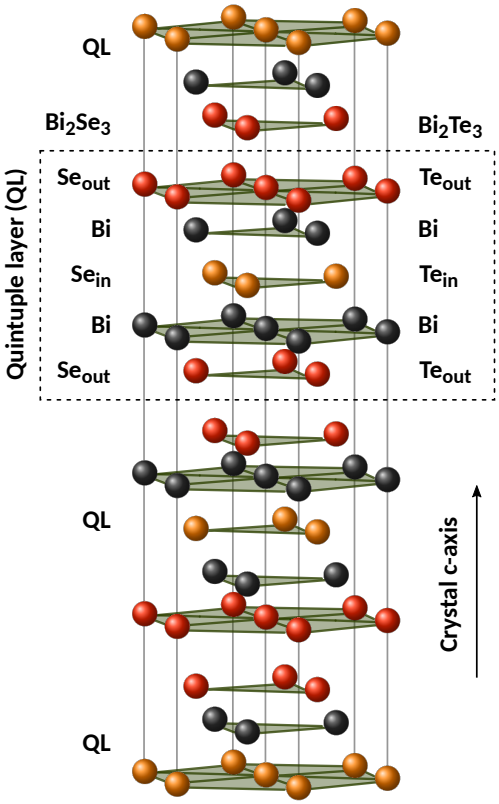

Figure 1.1 Structural unit of Bi_2Se_3 and Bi_2Te_3 consisting of three quintuple layers.

quintuple layer (QL) that consists of five sheets, i.e. Se(Te)-Bi-Se(Te)-Bi-Se(Te). The individual sheets are bonded covalently with each other to form a QL, while the QLs are connected by van-der-Waals interaction. The stacking direction defines the crystal *c*-axis, the *a* and *b*-axes are equivalent. Due to the fcc-type stacking, a unit cell (as shown in Fig.1.1) consists of three quintuple layers. For Bi_2Se_3 the *ab* and *c*-axis lattice constants are found to be ∼4.14 Å and ∼28.64 Å, respectively; while for Bi_2Te_3 they are ∼4.39 Å and ∼30.5 Å, respectively.

It is important to have a closer look at the local environment of the individual atoms in the system, because they are directly related to the NMR signals. First, the cylinder symmetry will have consequences for the symmetry of anisotropic NMR interactions, such as the NMR shift and quadrupole splitting (Sec.2.3), yielding a so-called *axial symmetry*. Next, the *inner* and *outer* positions of Se (Te) atoms within a QL are chemically non-equivalent and will thus give rise to individual resonance lines in an NMR experiment [23]. They shall therefore be distinguishable as Se_{in} (Te_{in}) and Se_{out} (Te_{out}) as shown in Fig.1.1.

From a symmetry operation viewpoint, Se_{in} (Te_{in}) and Se_{out} (Te_{out}) are non-equivalent as well. The inner Se (Te) site is the inversion centre of the Bi_2Se_3 structure. The corresponding inversion changes Se_{out} (Te_{out}) into Se'_{out} (Te'_{out}) and Bi into

Bi′. That is, there are two non-equivalent Se_{out} (Te_{out}) and two non-equivalent Bi sites in the Bi_2Se_3 (Bi_2Te_3) unit cell. However, from an NMR perspective that considers local environments only, Se_{out} (Bi, Te_{out}) and Se'_{out} (Bi′, Te'_{out}) are equivalent and cannot be distinguished.

In summary, for any NMR experiment in the present system, one expects *two* Se (Te) signals, i.e. Se_{in} (Te_{in}) and Se_{out} (Te_{out}) with an intensity ratio of 1 : 2, representing the number of sheets per QL, but only *one* Bi signal. The NMR active isotopes are ^{77}Se (spin 1/2, 7.6 % abundance), ^{125}Te (spin 1/2, 7 % abundance), and ^{209}Bi (spin 9/2, 100 % abundance). The other stable Te isotope, i.e. ^{123}Te, will not be investigated due to its low natural abundance of less than 1 %.

Chemical and physical properties

Bi_2Se_3 and Bi_2Te_3 are thermodynamically stable, solid condensates for a corresponding composition of 40 atomic % Bi and 60 atomic % Se (Te). Large single crystals can easily be synthesised with the *self-flux* method, which is crystal growth under slow cooling in a well mixed melt of Bi and Se (Te). A very commonly used method to prepare single crystalline samples is the Bridgman method [16]. An overview of the chemistry of Bi_2Se_3, Bi_2Te_3 and a number of related topological insulators can be found in Cava et al. [43].

Both materials are heavily doped semiconductors with narrow band gaps of $\sim$ 0.3 eV for Bi_2Se_3 and 0.15 to 0.17 eV for Bi_2Te_3 [12]. It is a consensus that self-doping drives the Fermi level up (or down) into the conduction (or valence) band, leaving free carrier concentrations, n, ranging between $10^{17} - 10^{20}$cm^{-3}, that give the materials their metallic conducting property [31]. The charge carriers in Bi_2Se_3 are electrons as the dominating defects are Se vacancies [44, 45]. In Bi_2Te_3, due to the very similar ionic radii of Bi and Te, antisite defects can be abound, yielding a p-type compound. If Te vacancies dominate, however, the system is an n-type semiconductor [31].

The formation of native defects cannot be avoided. However, especially the nominal composition of the melt, i.e. the molar ratio of Bi and Se (Te) initial for crystal growth, allows some control of the resulting carrier concentration [46, 47]. It is found that excess Se compensates to some extent Se vacancies, resulting in higher resistivity samples [18]. Similarly, depending on the molar ratio of Bi and Te in the Bi_2Te_3 synthesis, p-type or n-type samples can be obtained [46]. Furthermore, annealing of p-type Bi_2Te_3 single crystals under Te rich atmosphere was shown to turn the materials into n-type compounds [48].

Great efforts are taken to reduce the carrier concentrations in these topological insulators. One possibility is to tailor the majority carriers of Bi_2Se_3 and Bi_2Te_3 with doping. For example, Bi_2Se_3 doped with less than 1 % Ca turns into a p-type semiconductor, however, the carrier concentration remains high [49]. A more successful concept is to take advantage of compensating effects of electron donors and acceptors in more complex compounds, such as Bi_2Te_2Se ($n \sim 4 \times 10^{16}\mathrm{cm}^{-3}$ [31]) or $Bi_{1.08}Sb_{0.9}Sn_{0.02}Te_2S$ ($n < 3 \times 10^{14}\mathrm{cm}^{-3}$ [50]).

The incorporation of manganese into Bi_2Se_3 has significant consequences on the materials transport properties and thermoelectric performance as reported by Chong et al. [51]. Although Mn is a magnetic-dopant, they found that there is no significant change in the nature of the magnetism, which is in contrast to doping Mn in Bi_2Te_3 where Choi et al. [52] reported the presence of ferromagnetic ordering. Other studies report of a magnetic phase and supressed surface states in Cr or Fe doped Bi_2Se_3, while Pd doping of Bi_2Te_3 induces superconductivity [31].

The present study focusses on stoichiometric and non-stoichiometric Bi_2Se_3 and Bi_2Te_3 single crystalline samples investigated with NMR. Additionally, the effect of Mn doping on Bi_2Te_3 samples is studied via transport and thermoelectric properties.

1.3 Model topological insulator bismuth selenide

The topological non-trivial nature of Bi_2Se_3 (Z_2, strong topological insulator) was confirmed through *Angle-Resolved Photoemission Spectroscopy* (ARPES) in 2009 by Xia et al. [9], by measuring a Dirac-cone on the material's surface. This surface bands cross the band gap at the $\overline{\Gamma}$-point ($\boldsymbol{k} = 0$) of the Brillouin zone (Fig.1.2(b)). The Dirac-point, which is the touching point of the upper and lower half of the Dirac cone, lays well separated from the valence band within the energy gap of 0.3 eV, making Bi_2Se_3 an exceptional compound for the research of topological insulators. In contrast, the Dirac point of Bi_2Te_3 is buried within the valence band, making the surface state difficult to be distinguished from the bulk electronic states [12].

The origin for the emergence of the special surface bands is an *energy band inversion* at the Γ-point of the bulk energy band structure, which originates from a strong spin-orbit coupling (SOC) due to the heavy elements. In topological insulating systems, SOC reverses the order of bonding and anti-bonding states at the band edge (Fig.1.2(a)), i.e. bands formerly being part of the conduction band are shifted down while parts of the valance bands are shifted up. When brought in contact (real-space) with a topological trivial insulator, i.e. with normally ordered bands, the band inversion yields a Dirac-cone spanning across the gap (Fig.1.2(a)).

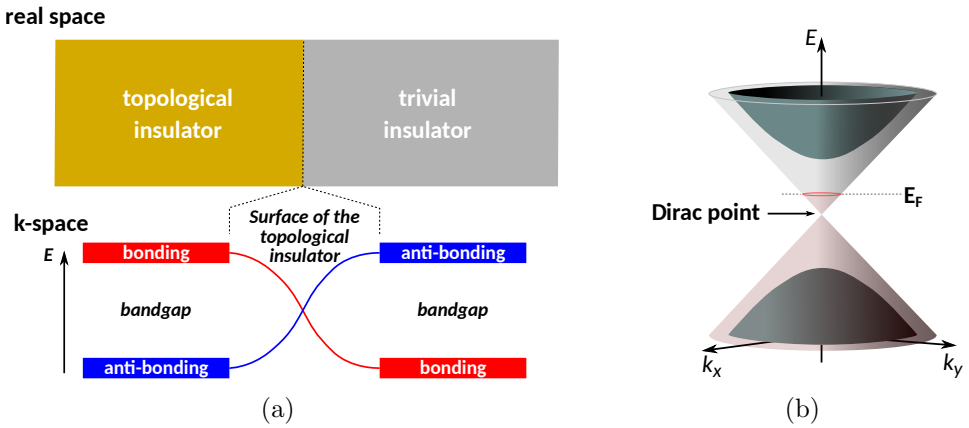

Figure 1.2 (a) Scheme of the interface between a topological and a trivial insulator. In k-space, the order of bonding and antibonding states is reversed, leading to the surface bands crossing the band gap (Dirac cone). (b) Idealised representation of a Dirac-cone in the two-dimensional k-space of the surface of a topological insulator, spanning the energy band gap.

SOC in these materials is assumed a band property rather than an atomic one. In a simplified picture, one might consider the substantial SOC in the bulk inducing the band inversion while it breaks down on the surface due to its absence in the neighbouring material.

In the particular case of Bi_2Se_3 and Bi_2Te_3, Zhang et al. [7] showed that SOC affects especially the order of Bi $6p_z$ and Se $4p_z$ orbitals which are of opposite parity and thus possess different symmetries providing the topological protection of the resulting surface states. Once spin-orbit coupling is switched on, the Bi $6p_z$-states are shifted into the valence band while the Se $4p_z$-states are shifted into the conduction band (Fig.1.3(b)). In an ideal material, the Fermi level lays within the band gap and only the valence band is occupied (at $T = 0\,\mathrm{K}$). Thus, the band inversion due to SOC must be accompanied by a slight[2] change in the relative occupation of Bi and Se orbitals in real-space.

As mentioned above, real samples show a rather low resistivity with the Fermi level intersecting the conduction (or valence) band, giving rise to a substantial number of free carriers. This fact is usually considered to be a big problem in experimental physics because the bulk transport properties conceal those of the surface states. On the other hand, the free carriers emerge on the lower edge of the band gap, namely at the Γ-point, and must therefore bear the signature of the band inversion (Fig.1.3(c)). In the present work it will be shown that a local probe like nuclear magnetic resonance (NMR) can measure the band inversion in quantitative agreement with first-principle calculations.

[2]Band inversion occurs only for a very small range of k around the Γ-point.

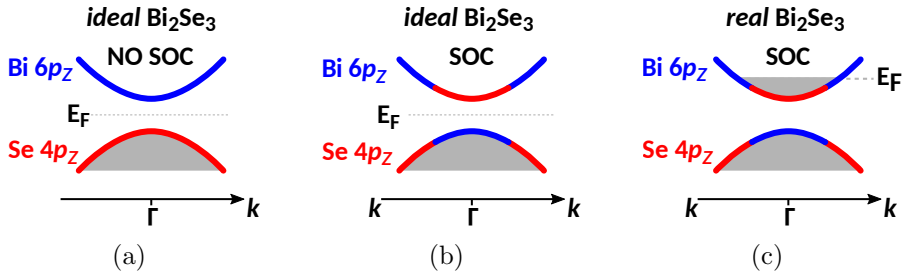

Figure 1.3 (a) Simplified band edge of Bi_2Se_3 without spin-orbit coupling and thus no band inversion. (b) The band edge with spin-orbit coupling. An inversion of parts of the conduction and valence bands (here Bi and Se p_z-states) occurs near the Γ-point. (c) Self-doping shifts the Fermi level (E_F) from the gap into the conduction band in real Bi_2Se_3 samples.

1.4 Literature review

1.4.1 Pure and Mn doped topological insulator Bi_2Te_3

This part of the project is a continuation of a study of pure and Mn doped Bi_2Se_3 carried out by the same research group. The investigation's results are presented in Chong et al. [51]. In summary, it was found that Mn doping affects the thermoelectric properties and slightly enhances the *figure of merit*, ZT.[3] In contrast to Bi_2Te_3, there was no magnetic ordering observed, instead, Mn moments order antiferromagnetically. Magnetoresistance was found to be originating from Lorentz force, while its magnetic field and temperature dependence indicates slight variations of the energy band structure compared to pure Bi_2Se_3.

Bi_2Te_3 is known as one of the best thermoelectric materials found so far. The research on this compound goes back to the 1950s. Today, the researchers focus on thin film and nano structured samples in order to optimize the transport properties. The review articles by Boulanger [53] and Mamur et al. [54] give an overview about the present state-of-the-art within the scope of thermoelectricity including historical developments.

Of particular interest for the present work are reports on magnetoresistance observed in Bi_2Te_3. There is a number of publications reporting magnetoresistance and other transport properties in thin films [55–58]. On the basis of a two dimensional transport and the presence of a strong spin-orbit coupling, the magnetoresistance is attributed to weak anti-localisation (WAL). Hor et al. [48] report the observation of a large low temperature positive magnetoresistances in macroscopic Bi_2Te_3 single

[3] An index combining electrical, thermoelectric, and thermal conductivity thermotransport to evaluate a material's thermoelectric power performance.

crystals. Similar results are found by Sultana et al. [59]. Thus, the MR in Bi_2Te_3 is complex and may depend on the sample dimensions. A clear assignment of the origin of the MR in macroscopic samples of Bi_2Te_3 is still lacking. The present study addresses this open question and provides the first study of the MR in Mn doped Bi_2Te_3 samples.

Since their recognition as topological insulators, Bi_2Te_3 and Bi_2Se_3 have rejuvenated interest and it is believed that magnetic doping can be used to manipulate their surface states by breaking time reversal symmetry, guiding the way towards new physics and potential functional devices.

Choi et al. [52] proved ferromagnetic ordering in Bi_2Te_3 when doped with 2 % Mn already in 2004. Hor et al. [60] verified the results in 2009 – then under the new perspective of a non-trivial topology – and determined the maximum Curie temperature to be $T_{\mathrm{Curie,max}} = 12\,\mathrm{K}$ for $Mn_{0.09}Bi_{1.91}Te_3$, confirming the material to be a "true dilute ferromagnet", while finding the surface states still present. In the following year, Niu et al. [61] determined the effective Mn moment to be $4.0\,\mu_\mathrm{B}$ based on calculations. They also concluded that it is a dilute ferromagnetic material and found the first indication of an opening of a gap on the Dirac-point. Finally, Watson et al. [62] reported the ferromagnetism to be independent of the chemical potential as they investigated *n*-type Bi_2Te_3 (in contrast to the former publications that investigated *p*-type Bi_2Te_3) and found an $T_{\mathrm{curie}} = 9-13\,\mathrm{K}$ for the 9 % Mn-doped samples.

In recent years, a number of groups published experimental work on Mn doped Bi_2Te_3 single crystals investigated with *Electron Paramagnetic Resonance* (EPR) [63–66]. These reports show the transition into a ferromagnetic phase for temperatures below $T_{\mathrm{curie}} \approx 12\,\mathrm{K}$, a strong evidence for an indirect coupling (RKKY[4]) among the Mn moments, and a potential formation of a spurious MnBi phase clustering in the crystals structure of Bi_2Te_3. The latter contributes as an additional ferromagnetic component to the total magnetic response.

There is a number of publications on the magnetic properties of Mn doped Bi_2Te_3 thin films. The studies report investigations of mostly monocrystalline samples of up to 70 nm thickness. Lee et al. [70] found a ferromagntic transition at about 17 K, similar to macroscopic samples. In several papers it is explicitly stated that the ferromagnetism seems not to depend on the carrier concentration [70–72], which is in direct contradiction to a RKKY coupling mediating the ferromagnetic ordering. A study carried out by Hosokawa et al. [73] investigated lightly doped thin films and potential positions of the Mn ions in the lattice. Intercalation (between two

[4]Ruderman-Kittel-Kasuya-Yoshida [67–69]

quintuple layers) and Te substitution is found to dominate.

In the context of the magnetism exhibited by Mn doped Bi_2Te_3, the underlaying coupling mechanism remains an open question, with experimental data that seems to be in disagreement with the theoretically proposed RKKY coupling. The NMR of Bi_2Te_3 may therefore offer valuable insight as an indirect coupling of *Bloembergen-Rowland* (BR) type was predicted to give rise to an extensive NMR line broadening [74], similar to what was found with ^{77}Se NMR in Bi_2Se_3 (see the following section on the NMR of spin 1/2 nuclei in Bi_2Se_3 and Bi_2Te_3).

1.4.2 NMR of the topological insulators Bi_2Se_3 and Bi_2Te_3

Spin 1/2 systems: ^{125}Te and ^{77}Se

The earliest publication on NMR of topological insulators goes back to Taylor et al. [15] reporting on ^{77}Se and ^{125}Te NMR of Bi_2Se_3 and Bi_2Te_3 powders. For ^{125}Te, they observed a Korringa-like, i.e. metal-like, behaviour at low temperatures indicating an interaction of the nuclear magnetic moments with free charge carriers, while ^{77}Se NMR shows multicomponent spin-lattice relaxtaion (T_1). These results are related to their thermoelectricity as well as topological properties of the samples.

Koumoulis et al. [17] were the first to investigate nano-crystalline Bi_2Te_3 in order to access the topologically protected surface states by the increased surface to volume ratio. Interestingly, they observed a "shoulder" growing and moving to increasingly negative shifts with decreasing particle sizes. The spin-lattice relaxation of both the main resonance and the shoulder indicates a typical metallic character (Korringa) for the latter. They argue that with decreasing particle size, i.e. below 33 nm, and increasing surface to volume ratio, the contribution of nuclei of the surface to the NMR signal becomes important. Koumoulis et al. [19] published another comprehensive NMR study of ^{125}Te NMR in powdered samples of Bi_2Te_3, Sb_2Te_3, $Bi_{0.5}Sb_{1.5}Te_3$, Bi_2Te_2Se, and Bi_2Te_2S, where NMR lineshape effects and spin-lattice relaxation as function of temperature are related to the defect chemistry and features relevant in the context of topological insulators.

The first NMR study of single crystalline Bi_2Te_3 was reported by Podorozhkin et al. [22]. They found two distinct NMR signals which were related to the two signals found in Bi_2Te_3 nanoparticles, due to similar shifts, i.e. a bulk and a surface signal, even though the surface to volume ratio was not sufficient to give rise to a surface signal. Temperature dependent measurements of the bulk signal revealed the total shift being dominated by a Knight shift contribution (interaction with free carriers) from which the activation energy was calculated.

In 30 % Cu doped Bi_2Se_3 single crystals, Matano et al. [24] observed a spontaneous breaking of the spin-rotation symmetry below the superconducting transition temperature, $T_c = 3.4K$. This confirms spin-triplet superconductivity.

With the first ^{77}Se NMR in Bi_2Se_3, Georgieva et al. [23] showed that the two chemically non-equivalent crystal sites, i.e. Se_{in} and Se_{out}, do in fact yield two distinct resonance lines with an intensity ratio of 1 : 2. Furthermore, with the aid of tight binding model calculations, an indirect nuclear dipole coupling arising from a *Bloembergen-Rowland* (BR) electronic spin susceptibility [75] was identified that induces extensive, magnetic field independent NMR line broadening. In the same year, the tight-binding model was refined and a detailed theoretical study of the Knight shift in Bi_2Se_3 and Bi_2Te_3 was published by Boutin et al. [76].

Single crystals of p and n-type Bi_2Te_3 were also investigated by Levin et al. [25], who reported an asymmetric lineshape of the ^{125}Te resonance line and attributed this "shoulder" to be arising from ^{125}Te nuclei in the close vicinity of structural defects. This conclusion is based on a substantially different T_1 of the shoulder. Seebeck coefficient measurements were employed in order to support the defect related conclusions.

Antonenko et al. [26] corrected their signal assignment reported previously [22], and related the second resonance line to the Te_{in} crystal site using the same argument as Georgieva et al. [23] for ^{77}Se in Bi_2Se_3. They further estimated the activation energy of the intrinsic carriers from the Knight shift and found an intriguing lineshape effect at low temperatures.

Choi and Lee [28] and Choi et al. [29] employed a new method to investigate the surface states of Bi_2Se_3 and Bi_2Te_3 using ^{77}Se and ^{125}Te NMR in nanopowders mixed with insulating Al_2O_3 nanoparticles. With an increasing Al_2O_3 to topological insulator mass ratio, they observed an additional NMR signal accompanied by an increasingly metallic behaviour which is attributed to the surface states.

In summary, there is a number of open questions connected with the NMR of spin 1/2 nuclei in Bi_2Te_3 and Bi_2Se_3. Especially the NMR linewidth, shift (anisotropy), and relaxation (T_2) has not been addressed in detail. From model calculations, a similar indirect coupling mechanism as observed in Bi_2Se_3 is expected for ^{125}Te in Bi_2Te_3, giving rise to large, field independent NMR linewidths [74]. As mentioned above, this should have direct consequences for the interaction of local moments associated with magnetic impurities as in the case of Mn doped Bi_2Te_3. In the current study, field dependent ^{125}Te NMR experiments in Bi_2Te_3 single crystals are used to answer this question of an exotic indirect coupling mechanism of the nuclear magnetic moments.

Quadrupole nuclei: ^{209}Bi

^{209}Bi NMR has only been reported for Bi_2Se_3 so far. Young et al. [16] reported a peculiar tranversal decay (T_2) anomaly of the quadrupole split ^{209}Bi spectrum in Bi_2Se_3 single crystals, i.e. a significant increase of the spin-spin relaxation time as one moves from the centre of the quadrupole pattern to the outer satellites. They further concluded that the Bi signal stems entirely from the bulk and no trace of a surface signal was found in macroscopic single crystals. The highly sensitive quadrupole NMR let them evaluate the quality of various crystal growth methods, concluding that crystal synthesis using the self-flux method and a Se-rich melt yields the best result. Based on temperature dependent measurements they argued that the free carrier concentration, n, drives the spin-lattice relaxation in this system.

Nisson et al. [18] followed with ^{209}Bi data of crystals obtained from various methods and Bi/Se precursor ratios. They found a clear n-dependence of the NMR shift and linewidth, with the latter interestingly *decreasing* with increasing carrier concentration, n. The hyperfine constant for bismuth was determined to be A$\sim$ 27 μeV, and they argue that there is only minor shift-effect for Bi nuclei near surface. In contrast to Young et al. [16], they found a rather weak temperature dependence of bismuth T_1. In a second paper the same group reported results on nano, micro and single crystalline Bi_2Se_3 [20]. While the spectra of nano structured and microscopic samples show no significant differences, a match between averaged single crystal and powder patterns was not achieved. So they employed a sophisticated selection rule that favours some orientations of the single crystal when simulating a powder average. The effect was attributed to an "anomalous magnetic response arising from surface currents associated with topologically protected states".

Using ^{209}Bi NMR shift at magnetic fields up to 30 T, Mukhopadhyay et al. [21] reported full spin polarisation in low carrier density single crystals of Bi_2Se_3, and further determined the effective electronic g-factor and the contact hyperfine term.

Together, the reports draw a rather controversial picture of ^{209}Bi in Bi_2Se_3. Basic NMR features, as the quadrupole splitting, the NMR linewidth and relaxation remain unclear. Most important, the orientation dependent ^{209}Bi quadrupole spectra are not understood. As will be shown, the effect of a distributed transverse decay (T_2) has been underestimated, resolving the reported discrepancy of single crystal and powder spectra. A careful study of ^{209}Bi NMR in Bi_2Se_3 single crystalline samples with various carrier concentrations as well as powders will be discussed in the present work. From these results, the first comprehensive room temperature study of a quadrupole nuclei in a topological insulator is presented.

Chapter 2

Theoretical background

2.1 Electronic properties of solids

2.1.1 Resistivity

In the general expression of *Ohm's law* the resistivity, $\boldsymbol{\rho}$, relates the current density, $\boldsymbol{J}$, in a system to the corresponding electric field, $\boldsymbol{E}$,[1]

$$\boldsymbol{E} = \boldsymbol{\rho}\boldsymbol{J} \ , \tag{2.1}$$

with

$$\boldsymbol{\rho} = \begin{pmatrix} \rho_{xx} & \rho_{yx} \\ \rho_{xy} & \rho_{yy} \end{pmatrix} \ . \tag{2.2}$$

It is enough to regard the system in two dimensions in the following discussion, there is no z-component for either $\boldsymbol{E}$ or $\boldsymbol{J}$. With current I_x driven through the sample connecting contacts in x-direction, the current density is $\boldsymbol{J} = (J_x, 0, 0)$ and, thus, the components of $\boldsymbol{E}$ become

$$E_x = \rho_{xx} J_x \tag{2.3}$$

and

$$E_y = \rho_{xy} J_x \ . \tag{2.4}$$

The latter equation (2.4) is zero in case of an isotropic material or in the absence of a magnetic field. With a uniform resistivity, ρ_0, throughout the sample under

[1] Comprehensive background can be found in Ashcroft and Mermin [77]

investigation, the scalar definition of a Voltage between two contacts located at distance l in x-direction is $V = E/l$. With J being the driving current I divided by the cross-section area of the sample, $A = h \cdot w$, (2.3) becomes Ohm's law,

$$V = \rho_0 \frac{l}{A} I \equiv RI \ , \tag{2.5}$$

with R being the measured resistance and $h \times w \times l$ give the sample dimensions.[2] The resistivity is further related to the carrier mobility, $\mu = v_x/E_x$ – the proportionality factor relating the electric field E_x to the resulting carrier drift velocity v_x – as

$$\rho_0 = \frac{1}{ne\mu}, \tag{2.6}$$

via the carrier concentration n. The mobility is proportional the carrier's *mean free path*. Note, with $[\mu] = m^2/(Vs)$, the mobility has the dimension of an inverse magnetic field.

2.1.2 Hall Effect and carrier concentration

With the application of an external magnetic field along the z-direction, $\boldsymbol{B} = (0, 0, B_z)$, charge carriers, q, travelling through the sample with drift velocity $\boldsymbol{v} = (v_x, 0, 0)$ will be subject to a *Lorentz force*,

$$\boldsymbol{F} = q(\boldsymbol{E} + \boldsymbol{v} \times \boldsymbol{B}) \ . \tag{2.7}$$

For the steady state, $\boldsymbol{F} = 0$, and it follows the total electric field is given by

$$\boldsymbol{E} = \begin{pmatrix} E_x \\ E_y \end{pmatrix} = \begin{pmatrix} \rho_{xx} J_x \\ v_x B_z \end{pmatrix} \ . \tag{2.8}$$

Thus, an external magnetic field $\boldsymbol{B}$ adds an additional component of the electric field through its effect on moving charge carriers, known as the *Hall effect*. With the current density, $\boldsymbol{J} = -ne\boldsymbol{v}$, i.e. $J_x = -nev_x$ with n being the carrier density and e the elemental charge, and equations (2.4) and (2.8) it follows that

$$E_y = \rho_{xy} J_x = v_x B_z \tag{2.9}$$

[2] $h$eight$\times w$idth$\times l$ength

and thus

$$R_{\mathrm{H}} \equiv \frac{\rho_{xy}}{B_z} = -\frac{1}{ne} \ . \tag{2.10}$$

Equation (2.10) gives the definition of the *Hall coefficient* R_{H}. The corresponding *Hall voltage* is defined as $V_{\mathrm{H}} = -E_y w$. And with

$$v_x = -\frac{J_x}{ne} = -\frac{I}{ne(h \cdot w)} \tag{2.11}$$

and (2.8), it assumes

$$V_H = \frac{IB_z}{neh} \ . \tag{2.12}$$

Therefore, by measuring the Hall voltage at a given magnetic field the carrier concentration, n, of the system under investigation can be determined. The relations given above represent the simplest case of a single carrier type transport (here electrons). In general, carriers with different mobilities, μ, (that includes effective masses m_e^* as well as scattering) and travelling directions (electrons and holes) may contribute to the total transport, making the determination of individual concentrations much more difficult.

In Bi_2Se_3 and Bi_2Te_3 the transport is assumed to come from a single carrier type, either electrons or holes, and is commonly described and experimentally evaluated using either equation (2.10) or (2.12) throughout the literature. Such a simplification is supported by the in most cases linear dependence of the Hall resistivity with the applied magnetic field.

2.1.3 Magnetoresistance

With the simple approach used above to derive the Hall effect, it can be shown that the system's resistivity, ρ_{xx}, remains unaffected by the application of an external magnetic field, B [77]. However, almost all real materials exhibit changes. That is, some of them show an increase of ρ_{xx} with B, whereas others behave oppositely, with a decrease in resistivity. The coupling of transport properties to magnetism is referred to as *magnetoresistance*. Depending on the relative orientation of B with respect to the current I, one differentiates between transverse ($I \perp B$) and longitudinal ($I \parallel B$) magnetoresistance (MR).

MR is typically given in percent as the relative change of the resistivity with

respect to the resistivity at zero magnetic field, $\rho(0)$,

$$MR\ [\%] = \frac{\rho(B) - \rho(0)}{\rho(0)} \times 100\ . \tag{2.13}$$

Depending on the origin, a MR can be negative or positive, i.e. the resistivity either decreases or increases with the magnetic field.

Today a whole variety of underlaying effects that yield magnetoresistance is known. The *ordinary* MR is positive and usually observed in metals and is related to an altering of the carrier pathway due to Lorentz force. It is smaller in case of $I \parallel B$ than at $I \perp B$. An interplay between sample geometry and carrier pathways may give rise to a positive *geometrical* MR, which can be seen as a geometry-enhanced ordinary MR.

If more than one band is involved in the electronic transport as in doped semiconductors where electrons and holes with different mobilities or scattering rates contribute to the conduction, then a *multiband* MR may arise. In this case the total current density will be composed of a number of individual $\boldsymbol{J}_i$, i.e. $\boldsymbol{J} = \sum_i \boldsymbol{J}_i$, with each of them pointing in different directions and thus yielding an increase in the apparent resistivity. This mechanism will result in a positive MR.

Negative MR may stem from spin scattering in paramagnetic materials. Other MR mechanisms are found in multicomponent layered structures. This includes spin dependent tunnelling that gives rise to *Tunnel* MR[78] in magnetic tunnelling junctions. Large effects are also observed in layered samples with alternating nanostructured ferromagnetic and nonmagnetic materials (*Giant* MR [79]). *Anisotropic* MR [80] is found in ferromagnetic materials. It changes sign depending the orientation o the driving current with respect to the external field. It is thought to stem from spin dependent scattering of conduction electrons due to spin-orbit coupling.

MR arising from *weak* (*anti*) *localisation* [81] is studied in thin films. It originates from the interference of conduction electrons in backscattering direction that can be suppressed by a well adjusted external magnetic field. Another well known MR is the *Quantum linear* MR [82] that is argued to arise from close-to-linear dispersions (vanishing effective mass) in the energy band structure.

2.1.4 Thermoelectric power

The thermoelectric effect, or *Seebeck effect*, concerns an electric field, $\boldsymbol{E}$, that arises across a sample when a temperature gradient, ∇T, is applied. The effect is described with freely moving charge carriers. Their mobility depends on their individual temperature. In an idealised sample with a temperature gradient maintained through a

heat source and a sink, "hot" carriers (electrons) are effectively moving faster than "cold" ones, yielding a net flow towards the cold end of the sample. In consequence, charge carriers accumulate at the cold end, which gives rise to an electric field opposite to the direction of the temperature gradient. In a steady state, the charge flow due to the temperature gradient and that of the electric field compensate. The proportionality factor between the temperature gradient and the electric field is the thermopower, or *Seebeck coefficient* S, of a system [77],

$$\boldsymbol{E} = S\nabla T \ . \tag{2.14}$$

S is measured as the voltage across a given sample arising from a temperature difference between the two contacts.

In case of single carrier conduction, the sign of S reveals the sign of the charge as it depends on whether $\boldsymbol{E}$ points in the same direction as the temperature gradient or in the opposite one. In general, the situation is more complicated, e.g. when assuming more types of charge carriers with different effective masses, sign, and scattering rates.

2.2 Magnetic properties of solids

Solids are divided into different classes on the basis of their response to an external magnetic field. If the induced moments in the material are polarised in opposite direction to the external magnetic field, i.e. the field inside the material is smaller than the applied field, the compound is *diamagnetic*. If the internal moments align with the external field such that the internal field exceeds the external one, the material is *paramagnetic*. If these moments align spontaneously without an external field, the material is *ferromagnetic*. If this alignment occurs in a way that neighbouring moments cancel each other out, i.e. the spins are anti-parallel, the material it said to behave *anti-ferromagnetically*.

With these well-known classes, the magnetism in modern solid state physics is by far not depleted. In the present work, however, a focus on paramagnetism and ferromagnetism is sufficient, except for the addition of *dilute ferromagnetism*.

A typical experiment to access the magnetism in a system is to measure the magnetisation, M, arising from the application of an external magnetic field (especially the field dependence of M provides important insight). In such an experiment, the magnetic field is applied from a maximum field to the negative maximum and back, a full loop, while M is recorded as a function of field strength.

In a diamagnet, M is negative for positive fields and vice versa, and shows in most cases a linear dependence with $M = 0\,\mathrm{A/m}$ at zero field. The magnetism stems from filled shells in insulators (*Larmor diamagnetism*) or from the orbital motion of conduction electrons (*Landau diamagnetism* [77]).

A paramagnet shows the opposite behaviour to a diamagnet, i.e. with increasing field a positive magnetisation develops. Similar to diamagnetism, it is often observed to be linearly dependent on the magnetic field with no magnetisation at zero applied field. The origin can be partially filled shells (*Van Vleck paramagnetism*) or the spins of conduction electrons (*Pauli paramagnetism* [77]).

Ferromagnets exhibit a positive exchange interaction in first approximation, followed by a spontaneous alignment of their moments (in domains) even in the absence of a magnetic field. The main difference to diamagnetism and paramagnetism is that in ferromagnets (and other classes) an interaction of the magnetic moments among each other is allowed that may give rise to *magnetic ordering* and a net increase of the magnetisation. The ordering is in competition with temperature, which favours a random orientation of the moments, such that for a ferromagnet (and other magnetically ordered systems) there must exists a critical temperature, the *Curie temperature*, T_{curie}, above which the ordering is destroyed. The magnetic field dependence of a ferromagnetically ordered system exhibits a finite magnetisation even at zero field (*magnetic hysteresis*). Furthermore, ferromagnetic ordering often allows a full polarisation of the magnetic moments resulting in a saturation of the magnetisation at sufficiently high fields.

In a dilute ferromagnet, the spins are on average too far from each other to interact directly, and thus, no magnetic ordering should be observed. But through indirect exchange couplings mediated by itinerant carriers, such as in the context of an indirect nuclear dipole interaction in NMR mentioned in the next chapter, these moments can "see" each other over greater distances. The mechanism involves a coupling of the local magnetic moment with the carriers. The material behaves like a ferromagnet but with the difference of a very low density of moments, hence a dilute ferromagnet.

Antiferromagnets show a magnetic ordering where the neighboured moments point in the opposite direction (or be in a more complex arrangement) such that their magnetic moments cancel out. Ideally, there is no magnetisation, however, in real samples a much reduced magnetisation is observed under the application of an external field. The transition from a paramagnet to a antiferromagnet occurs at the so-called *Néel temperature*, T_{N}.

2.2.1 Magnetic susceptibility

As mentioned above, the magnetic susceptibility, χ, in a solid can have several origins, i.e.

$$\chi = \chi_{\text{local}} + \chi_{\text{Pauli}} + \chi_{\text{core}} + \chi_{\text{orbital}} = \chi_{\text{local}} + \chi_0 \ , \tag{2.15}$$

with the susceptibility arising from local moments ,χ_{local}, as associated with magnetic impurities, the Pauli susceptibility, χ_{Pauli} of conduction band carriers, as well as a contribution from closed shells, χ_{core}, and a contribution from the orbital electronic motion, χ_{orbital}. The latter two are related to diamagnetism, i.e. represent the above mentioned Larmor and Landau diamagnetism. In the current study of magnetically doped topological insulators with almost temperature independent carrier concentrations, the Pauli susceptibility and the diamagnetic contributions are represented by a temperature independent susceptibility, χ_0. The temperature dependence of the susceptibility is then dominated by local magnetic moments, χ_{local}, and shall therefore be discussed in more detail.

The magnetisation, M, arising from a system of N identical ions with angular momentum J subject to a magnetic field, B, is given by [77]

$$M = \frac{N}{V} g\mu_{\text{B}} J B_J(\beta g\mu_{\text{B}} JB) \tag{2.16}$$

with the *Brillouin function*,

$$B_J(x) = \frac{2J+1}{2J}\coth\left(\frac{2J+1}{2J}x\right) - \frac{1}{2J}\coth\left(\frac{1}{2J}x\right). \tag{2.17}$$

Here, N/V denotes the number of magnetic ions per unit volume, g the *Landé* or g-factor, μ_{B} Bohr's magneton, and $\beta = 1/k_{\text{B}}T$ with the Boltzmann constant, k_{B}. For sufficiently high temperatures, T, i.e. $g\mu_{\text{B}}B \ll k_{\text{B}}T$, $B_J(x)$ can be approximated as [77]

$$B_J(x) \approx \frac{J+1}{3J}x \ , \tag{2.18}$$

which yields for the corresponding magnetic susceptibility,

$$\chi = \frac{M}{B} = \frac{N}{V}\frac{(g\mu_{\text{B}})^2 J(J+1)}{3k_{\text{B}}T} \ . \tag{2.19}$$

Eq.(2.19) is known as *Curie's law*, characterizing the competition between an align-

ment of the spins due to the external field and temperature induced disorder.

In the *mean field theory* each magnetic moment "sees" the same average magnetic field arising from its environment. This approximation yields a high temperature behavior known as the *Curie-Weiss law*, which is almost identical in form to Curie's law [51, 77],

$$\chi = \chi_{\text{local}} + \chi_0 = \frac{C}{T-\theta} + \chi_0 = \frac{n_{\text{p}}\mu_0 P_{\text{eff}}^2}{3k_{\text{B}}}\frac{1}{T-\theta} + \chi_0 \ . \tag{2.20}$$

Here, the *Curie constant*, C, combines the density of paramagnetic ions, n_{p}, and their effective moment, P_{eff}, with some constants already known from Curie's law. In some ideal cases of ferromagnets, θ equals the ferromagnetic transition temperature, the *Curie temperature*, T_{Curie}.

The high temperature susceptibility of a surprisingly large number of materials with local magnetic moments can be described by equation (2.20) with sufficient accuracy. After subtracting a temperature independent, χ_0, the reciprocal $\chi(T)$ is can be used to find C, and thus either the density of magnetic ions or their effective moment can be extracted.

2.3 Nuclear magnetic resonance

2.3.1 Basic interactions

External magnetic fields

The *Zeeman interaction* describes the interaction of a nuclear spin $\boldsymbol{I}$ with an external magnetic field via the associated nuclear magnetic moment, $\boldsymbol{\mu} = \gamma\hbar\boldsymbol{I}$, as

$$\mathcal{H}_{\text{Z}} = -\gamma\hbar I_z B_0 \ , \tag{2.21}$$

where $\hbar = h/2\pi$ denotes the reduced Planck constant and γ is the isotope specific gyromagnetic ratio. The z-axis is defined by the laboratory frame. The *resonance condition*,

$$\boldsymbol{\omega}_{\text{L}} = \gamma\boldsymbol{B}_0 \ , \tag{2.22}$$

defines the *Larmor frequency* ω_{L}. In an NMR experiment, an additional, oscillating magnetic field, $\boldsymbol{B}_1(t)$, is applied perpendicular to $\boldsymbol{B}_0$,

$$B_{\text{y}}(t) = 2B_1 \cos(\omega t), \tag{2.23}$$

with the radio or *nutation* frequency (cf. section 4.3.2 and Fig.4.3)

$$\omega_{\mathrm{rf}} = \gamma B_1 \ . \tag{2.24}$$

In the classical picture, the application of $\boldsymbol{B}_1(t)$ in resonance with the spin, i.e. $\omega = \omega_{\mathrm{L}}$, yields a rotation of $\boldsymbol{\mu}$ in the *rotating frame* $(x(t), y(t), z)$ about an axis perpendicular to $\boldsymbol{B}_0$. Applying $\boldsymbol{B}_1(t)$ for a duration τ rotates $\boldsymbol{\mu}$ by an angle

$$\varphi = \omega_{\mathrm{rf}} \cdot \tau \ , \tag{2.25}$$

within the xz-plane of the rotating frame. φ will be referred to as *nutation angle*. The most simple NMR experiment uses a single $\pi/2$-pulse, such that

$$\varphi = \omega_{\mathrm{rf}} \cdot \tau_{\pi/2} = 90^\circ \ , \tag{2.26}$$

i.e. $\boldsymbol{\mu}$ is rotated into the xy-plane of the rotating (and the laboratory) frame. This experiment gives rise to the *Free induction decay* (FID).

Internal fields - NMR shift

In its real chemical environment, a nucleus will "see" an effective local magnetic field, B_{loc}, that is different from the external magnetic field B_0 due to its electronic surrounding. The difference between the external and the local magnetic field creates a frequency offset of the resonance line which is referred to as *NMR shift* (K),

$$K\ [\mathrm{ppm}] = \frac{\nu_{\mathrm{sample}} - \nu_{\mathrm{ref}}}{\nu_{\mathrm{ref}}} \times 10^6 \ . \tag{2.27}$$

The offset is measured against the resonance frequency, ν_{ref} of a reference sample. The shift arises from a variety of couplings of the nuclear magnetic moment with its electronic environment. The shift is represented as a second rank tensor,

$$\mathcal{H}_K = -\gamma\hbar \boldsymbol{I}\mathbf{K}\boldsymbol{B}_0, \tag{2.28}$$

reflecting the characteristic symmetries of the nuclear environment. A measured NMR shift can therefore be written as a sum of an isotropic and an anisotropic shift contribution,

$$K(\beta, \alpha, \eta_K) = K_{\mathrm{iso}} + K_{\mathrm{aniso}} \left[\frac{3\cos^2\beta - 1}{2} + \frac{\eta_{\mathrm{K}}}{2} \sin^2\beta \cos 2\alpha \right] \ , \tag{2.29}$$

with

$$K_{\mathrm{iso}} = \frac{K_{XX} + K_{YY} + K_{ZZ}}{3} \tag{2.30}$$

and

$$K_{\mathrm{aniso}} = K_{ZZ} - K_{\mathrm{iso}} \ . \tag{2.31}$$

Here, β and α denote Euler angles accounting for the relative orientation of $\mathbf{K}$ in its *principle axes system* (PAS) (K_{XX}, K_{YY}, K_{ZZ}) with respect to $\boldsymbol{B}_0$ (laboratory frame). The asymmetry parameter, η_K, is defined as $\eta_{\mathrm{K}} = (K_{XX} - K_{YY})/K_{\mathrm{aniso}}$. For $\eta_{\mathrm{K}} = 0$, the shift is axial symmetric as in case of Bi_2Se_3 and Bi_2Te_3 [23, 76], and equations (2.30) and (2.31) can be rewritten as $K_{\mathrm{iso}} = (K_{ZZ} + 2K_{XX})/3$ and $K_{\mathrm{aniso}} \equiv K_{\mathrm{axial}} = (K_{ZZ} - K_{XX})/3$, respectively.

Direct dipole interaction

A nuclear spin $\boldsymbol{S}$ in the vicinity of a spin $\boldsymbol{I}$ also causes variations of the local field $\boldsymbol{B}_{\mathrm{loc}}$ (seen by $\boldsymbol{I}$), because of its magnetic moment $\boldsymbol{\mu}_{\mathrm{S}}$. The *heteronuclear dipole interaction* between two unlike nuclei, i.e. $\gamma_{\mathrm{S}} \neq \gamma_{\mathrm{I}}$, can be written as [83]

$$\mathcal{H}_{\mathrm{IS}} = \frac{\mu_0}{2\pi}\gamma_{\mathrm{I}}\gamma_{\mathrm{S}}\hbar^2 \left[\frac{1 - 3\cos^2\theta}{2r^3}\right] (I_z S_z) \ . \tag{2.32}$$

Here, μ_0 denotes the permeability of the vacuum, θ is the relative angle between the internuclear vector with length r and the external field B_0.

Homonuclear dipole interaction holds for like nuclei, i.e. $\gamma_{\mathrm{I}} = \gamma_{\mathrm{I}'}$,

$$\mathcal{H}_{\mathrm{II}} = \frac{\mu_0}{4\pi}\gamma_{\mathrm{I}}^2\hbar^2 \left[\frac{1 - 3\cos^2\theta}{2r^3}\right] (3I_z I'_z - \boldsymbol{I}\cdot\boldsymbol{I}') \ . \tag{2.33}$$

The homonuclear dipole coupling is different from the heteronuclear interaction because transitions can be induced as the coupling partners are in resonance. Homonuclear dipole interaction has consequences for the excitation of an NMR signal and can give rise to *spin-spin relaxation*.

The *Method of Moments*, introduced by Van Vleck [84], assumes neighbour induced spatial fluctuations of B_{loc} resulting in a Gaussian distribution of frequencies, that is, in an NMR line broadening. The square of the distribution's linewidth is

identified as its *second moment* $\langle\Delta\omega^2\rangle$, reading [84, 85]

$$\langle\Delta\omega^2\rangle_{\mathrm{IS}} = \left(\frac{\mu_0}{4\pi}\right)^2 \frac{1}{3}\hbar^2\gamma_{\mathrm{I}}^2\gamma_{\mathrm{S}}^2 S(S+1)\frac{1}{N}\sum_{ij}\frac{(3\cos^2\theta_{ij}-1)^2}{r_{ij}^6} \ , \tag{2.34}$$

and

$$\langle\Delta\omega^2\rangle_{\mathrm{II}} = \left(\frac{\mu_0}{4\pi}\right)^2 \frac{3}{4}\hbar^2\gamma_{\mathrm{I}}^4 I(I+1)\frac{1}{N}\sum_{ij}\frac{(3\cos^2\theta_{ij}-1)^2}{r_{ij}^6} \ , \tag{2.35}$$

that is, the sum over all the pairwise interactions between nucleus i of spin $\boldsymbol{I}$ and j of $\boldsymbol{S}$ or $\boldsymbol{I}$, respectively. Thus, line broadening due to direct dipole interactions can be estimated with adequate precision if γ_{I} and γ_{S} are known, as well as the distances and relative orientations of the atoms in the crystal structure.

Indirect magnetic dipole interaction

In case *indirect magnetic dipole interaction* the coupling between nuclear moments is mediated by electronic states. This requires hyperfine couplings provided by the contact interaction of s-like electronic states. Indirect nuclear spin exchange was first developed for molecules [86, 87]. With the *Bloembergen-Rowland* (BR) [75] and the *Ruderman-Kittel-Kasuya-Yosida* (RKKY) [67–69] interaction, the theory was extended to crystalline solids. Both mechanisms involve exchange interactions of itinerant carriers. The difference is that the former, the BR coupling, requires virtual transitions from the valence band into the conduction band and is therefore related to the energy band gap. This is a behaviour usually expected for insulators. The latter, the RKKY mechanism, involves free carriers applies therefore for metals.

Indirect dipole interaction has the general form of an exchange interaction between nuclear spins, $A\boldsymbol{I}_1 \cdot \boldsymbol{I}_2$. In case of Bi_2Se_3, BR coupling has been shown to be the dominant source of extensive NMR line broadening [23], even though these materials are heavily doped degenerate semi-conductors. The interaction between spins $\boldsymbol{I}_i$ and $\boldsymbol{I}_j$ (like or unlike) can be approximated as [23]

$$\mathcal{H} = \sum_{ij} J_{ij}\boldsymbol{I}_i \cdot \boldsymbol{I}_j \ , \tag{2.36}$$

where J_{ij} denotes the exchange coupling constants derived from second order perturbation theory on the basis of contact hyperfine interaction. The resulting NMR line broadening of a resonance line (i) is then given in the terms its second moment

$$\langle \Delta\omega \rangle_i = \sum_j \frac{I_j(I_j+1)}{3\hbar} J_{ij}^2 \ . \tag{2.37}$$

An indirect dipole coupling can be identified by an magnetic field independent NMR linewidth that is particularly larger than the present direct dipole interaction. Furthermore, the indirect coupling (including J-coupling in molecules) is a *scalar* and, thus, an *isotropic* interaction, which means it is not averaged out in isotropic liquids or *magic angle spinning* (MAS).[3]

2.3.2 Electric quadrupole interaction

First order quadrupole interaction

Nuclei with spin $I > 1/2$ are subject to an interaction between their nuclear quadrupole moment, Q, and the *electric field gradient* (EFG) arising from their electronic surrounding,

$$\mathcal{H}_\mathrm{Q} = \frac{\hbar\omega_\mathrm{Q}}{6}(3I_z^2 - I(I+1)) \left[\frac{3\cos^2\beta - 1}{2} + \frac{\eta}{2}\sin^2\beta\cos 2\alpha \right] \ . \tag{2.38}$$

The *quadrupole frequency*,

$$\nu_\mathrm{Q} = \omega_\mathrm{Q}/2\pi = \frac{3e^2qQ}{2I(2I-1)h} \ , \tag{2.39}$$

measures the strength of the interaction. Here, eQ denotes the electric quadrupole moment of the nucleus and $eq = V_{ZZ}$ (including the asymmetry parameter η - cf. Eq.(2.47), and the *Euler angles* α and β) refers to the local EFG. The latter will be discussed in more detail below. Note, according to the signs of eQ and eq, ω_Q can be positive or negative.

Quadrupole interaction is independent of the external magnetic field, and, thus, only for sufficiently strong $\boldsymbol{B}_0$ ($\omega_\mathrm{L} \gg \omega_\mathrm{Q}$) $\mathcal{H}_\mathrm{Q}$ can be treated as a small perturbation. If so, the quadrupole coupling shifts the $2I+1$ Zeeman levels individually. It follows that the energy difference between two neighored states, $m \leftrightarrow m+1$, will be changed

[3] MAS is one of the most important techniques used in NMR, which allows the removal of line broadening effects due to the anisotropic interactions like CSA, Knight shift, direct dipole coupling, and first order quadrupole interaction.

as [83]

$$\begin{aligned} \hbar\Delta\omega &= h\tilde{\nu}_{\mathrm{Q}}(\beta,\alpha,\eta)\,(m+1/2) \\ &\equiv h\nu_{\mathrm{Q}}\left[\frac{3\cos^2\beta-1}{2}+\frac{\eta}{2}\sin^2\beta\cos 2\alpha\right](m+1/2)\ , \end{aligned} \tag{2.40}$$

where $m = (-I, -I+1, ..., I-1)$. Thus, the signal at the resonance frequency ω_{L} splits $2I$ individual lines, separated by $\tilde{\nu}_{\mathrm{Q}}(\beta,\alpha,\eta)$. A quadrupole spectrum consists of $2I$ equally spaced resonance lines, a *central transition* (CT), i.e. $m = -1/2$, and $(2I-1)/2$ pairs of satellites.

Excitation conditions

As quadrupole interactions can be very strong (easily exceed other couplings as NMR shift or dipole interactions by orders of magnitude), it is important to relate ω_{Q} to the strength of the radio frequency field, ω_{rf}. If $\omega_{\mathrm{rf}} \gg \omega_{\mathrm{Q}}$, the coupling of the rf-field to the spin system is called *non-selective* [83]. In this case, the quadrupole interaction is small compared to the rf-field and can be treated like a small perturbation. The system essentially behaves as a spin 1/2 system, i.e. as if not being subject to quadrupole interaction. The opposite case, i.e. when $\omega_{\mathrm{Q}} \gg \omega_{\mathrm{rf}}$, the excitation is *selective*. Ideally, selective excitation induces a single transition. In this case both the quadrupole interaction and the rf-field have a similar strength and the behaviour of the spin system under excitation can be very different to non-selective excitation. The nutation frequency, ω_{rf}, of a selectively excited transition is significantly accelerated compared to a non-selectively excited spin system, i.e.

$$\tilde{\omega}_{\mathrm{rf}} = 2W_m\omega_{\mathrm{rf}}\ , \tag{2.41}$$

with

$$W_m = \frac{1}{2}\sqrt{I(I+1)-m(m+1)}\ . \tag{2.42}$$

Here, m represents as the single quantum transition process $m \to m+1$, while W_m^2 denotes its probability. From experimental point of view, selective excitation in a quadrupole split system appears as if the spin system sees an amplified rf-field, B_1, according to Eq.(2.24). Thus, the nutation is accelerated by selective excitation and depends on the transition m.

Obviously, selective excitation is a fingerprint of quadrupole interaction. In this project *nutation spectroscopy* is employed to study the quadrupole interaction of

^{209}Bi in Bi_2Se_3 single crystals by evaluating transition specific excitation conditions using (2.41). In Tab.2.1, the relative change of $\tilde{\omega}_{\mathrm{rf}}$ for each transition in a quadrupole split spin 9/2 system like ^{209}Bi is listed.

Table 2.1 Enhanced nutation frequencies due to selective excitation of single transitions in a quadrupole split spin 9/2 system.

transition	CT	1st satellite	2nd satellite	3rd satellite	4th satellite
$\tilde{\omega}_{\mathrm{rf}}/\omega_{\mathrm{rf}}$	1/5	$1/\sqrt{24} \approx 0.204$	$1/\sqrt{21} \approx 0.218$	1/4	1/3

The intensity of a quadrupole split spectrum also depends on the excitation condition [83, 88]. For a non-selectively excited (NS) transition m, the relative intensity is given by

$$I^{NS}_{m,m+1} = \frac{W_m^2}{\sum_{m=-I}^{I-1} W_m^2} \ , \tag{2.43}$$

where the sum in the denominator reflects the full intensity of a corresponding spin 1/2 system (i.e. no quadrupole interaction).

Similarly, for a selectively excited (S) transition m, the intensity is

$$I^{S}_{m,m+1} = \frac{W_m}{\sum_{m=-I}^{I-1} W_m^2} \ . \tag{2.44}$$

Electric field gradient

The electric field gradient (EFG) represents the local electronic environment in terms of a charge density $\rho(\boldsymbol{r})$ as it appears at the nucleus site of interest. As a simple example, the EFG, V_{ij}, arising from a single ion with charge q at distance r can be calculated as

$$V_{ij} = \frac{\partial^2 V}{\partial x_i \partial x_j} \ , \tag{2.45}$$

with the potential as

$$V = \frac{q}{4\pi\varepsilon_0}\frac{1}{r} \ , \tag{2.46}$$

where ε_0 denotes the electric permittivity and $r = |\boldsymbol{r}|$. The EFG is thus expressed in terms of a second rank tensor, V_{ij}. It is traceless, i.e. its diagonal components

when diagonalised sum up to zero. Conventionally, the principle components of V_{ij} are ordered as $|V_{ZZ}| \geq |V_{YY}| \geq |V_{XX}|$. The asyymetry parameter η is defined as $\eta = \frac{V_{XX}-V_{YY}}{V_{ZZ}}$. The complete information of the EFG is then given by

$$\begin{cases} V_{ZZ} = eq \\ \eta \ (0 \leq \eta \leq 1) \ . \end{cases} \tag{2.47}$$

From equations (2.45) and (2.46) and the superposition principle it can be seen that the EFG of a given distribution of charges is dominated by the closest ions, as it is proportional to $\sim 1/r^3$. That is, the atoms of the local structure surrounding a nucleus in a given solid can be approximated by effective point charges and the EFG arising from this configuration can easily be calculated.

The situation in real solids is usually more complex. Next to the EFG from the lattice, there can be contributions form deformed closed shells.[4] Most importantly, not fully occupied orbitals will yield a substantial EFG. It is clear that doping which changes the relative occupation of orbitals, will drive such an effect, but so can virtual hopping [89]. In Ch.8, a general expression of the EFG arising from electronic states will be given.

2.3.3 Relaxation

Longitudinal relaxation

To establish equilibrium magnetisation, M_z, in a spin system exposed to an external magnetic field, the spins need to couple to the lattice to exchange energy. The corresponding equilibration is called *longitudinal* or *spin-lattice relaxation*. *Magnetic relaxation* occurs when the nuclear moments couple to the fluctuating magnetic field induced by free carriers. Another source of highly a efficient coupling between nuclear spins and the lattice yields *quadrupole relaxation*. Here, the nuclear moments couple to fluctuation of the EFG arising form lattice vibrations represented by interactions with the present phonon spectrum [90]. In most materials, however, it is complicated to decide weather a system relaxes via quadrupole relaxation or the coupling to free carriers. In systems with both, spin 1/2 and quadrupole nuclei, their individual relaxation can be different, indicating different mechanisms. In quadrupolar split systems, the apparent relaxation depends on the excitation conditions [91].

In an NMR experiment, the spin-lattice relaxation refers to the time evolution

[4] Note, regular closed shells will not create an EFG due to their spherical symmetry.

of the longitudinal magnetisation M_z broad out of equilibrium,

$$M_z(t) = M_0 \left(1 - \mathrm{e}^{-\frac{t}{T_1}}\right) \ , \tag{2.48}$$

with the spin lattice relaxation time T_1.

Transverse relaxation

Transverse refers to the decay of the xy-component of the Magnetisation, M_{xy}, during an NMR experiment. In case of an FID, M_{xy} vanishes with T_2^*, representing the inverse width of the FID's Fourier transform.

In most systems spins retain their individual phase information beyond T_2^*. Echo experiments, as will be discussed in the methods section 4 make use of the phase coherences to *refocus* spins. The typical time scale which describes the loss of phase coherence or *dephasing* of spins in the xy-plane is referred to as *spin-spin relaxation time* T_2. T_2 is measured via tracing the spin-echo decay of a given system (cf. Ch.4).

Transverse relaxation can have various sources. The upper limit is the spin system's spin-lattice relaxation time T_1 (cf. *Redfield theory* [85]). Sometimes it is found that the spin lattice relaxation of another spin system in the compound gives rise to tranverse relaxation. This is supposed to contribute to the fast spin-echo relaxation observed for ^{77}Se in Bi_2Se_3, where T_1^{Bi} is expected to yield T_2^{Se} via the significantly enhanced spin-spin coupling between the 100 % abound Bismuth nuclei and Se [23]. Efficient homonuclear dipole couplings can also give rise to rapid spin-spin relaxation.

T_2 measured by the characteristic decay of a spin echo is commonly approximated with a single exponential function

$$M(\tau) = M_0 \cdot \exp\left(\frac{-2\tau}{T_2}\right), \tag{2.49}$$

or a Gaussian decay,

$$M(\tau) = M_0 \cdot \exp\left(-2\left(\frac{\tau}{T_{2\mathrm{G}}}\right)^2\right) \ , \tag{2.50}$$

where τ denotes the time between two pulses in an echo experiment (cf. Ch.4).

Chapter 3

Methods I: structural, electronic and magnetic properties

After working out the theoretical background of experimental techniques used in this work, the methodological aspects of characterising macroscopic properties shall be discussed. X-ray diffraction (XRD) is an inevitable step, and an essential link between crystal synthesis and their subsequent characterisations. This will be discussed first. Then, the methods use to investigate the electronic and magnetic properties are discussed separately. These are carried out on the physical property measurement system (PPMS) and magnetic property measurement system (MPMS).

3.1 X-ray diffraction

An integral part of the present project was to synthesize samples for subsequent investigations, including a comparison between home-made samples those received form overseas laboratories. It is therefore essential to identify the crystal structure and phase purity of these samples. For this purpose, powder X-ray diffraction (powder XRD) was employed.

Powder XRD was measured on *Bruker*[1] D8 diffractometer equipped with a Cobalt anode ($\lambda = 1.789\,\text{Å}$). In the present work, diffraction patterns of powders were acquired usually between 2θ angles of 5° and 80°. A measuring time that gave a good signal-to-noise ratio is around 60 min in most cases with a 2θ increment of 0.05°.

All the powder samples were prepared in the following way. First, pieces of the material to be investigated were ground in a mortar and pestle for 20 to 30 minutes.

[1]Bruker Corporation, Billerica, MA, USA

A small amount of the powder was then placed in the middle of a quartz sample holder. Note, quartz sample holder was used here as it does not give any XRD reflections.[2] A small droplet of ethanol (C_2H_5OH) was placed on the powder yielding it to spread over the sample holder. This creates a thin layer of material covering an area larger than the spot of the X-ray beam once the ethanol had evaporated. A thin layer of sample is important to allow proper height adjustments which can influence the position of reflections. Furthermore, a thin layer of material is sufficient because of the heavy elements (Se, Te, Bi) being investigated in this project, where the penetration depth of the X-ray is limited to a few micrometres.

The acquired XRD patterns were analysed using the *X'Pert HighScore* software by *PANalytical*[3] and *Topas* software by *Bruker*. The reflection patterns are matched with standard patterns from the so-called *Powder Diffraction Files* (PDF) database provided by the *International Centre for Diffraction Data*[4] which is implemented within the X'Pert HighScore software. In the case of Topas, prior to the measurements a *standard reference material* (SRM) provided by *National Institute of Standards and Technology*[5] (NIST) – NIST SRM1976 – was used to characterize and calibrate the instrument. The results gave the instrumental properties (e.g. intrinsic broadening), which is a starting point for a detailed analysis of the raw XRD data.

3.2 Physical Property Measurement System

3.2.1 Instrumentation

All electrical and thermal transport measurements were carried out on a Physical Property Measurement System (PPMS) from *Quantum Design*[6]. The PPMS consists of two main parts: the console that operates the measurements, and the sample chamber providing the required experimental conditions.

A sweepable superconducting magnet equipped with a cryostat houses the sample chamber. Magnetic fields up to $\pm 8.5\,\mathrm{T}$ can be applied. The full range of temperatures between 1.9 K to 400 K is available. Both, the magnetic field and temperature, can be continuously swept during measurements or be adjusted and held stable at any value in a fully automated way.

[2] Quartz sample holders are single crystals cut in such a way that *no* reflections occur.
[3] Today Malvern Panalytical Ltd a company of Spectris, Egham, UK.
[4] International Centre for Diffraction Data, Newtown Square, PA, USA.
[5] National Institute of Standards and Technology, Gaithersburg, Maryland, USA.
[6] Quantum Design, Inc., San Diego, CA, USA

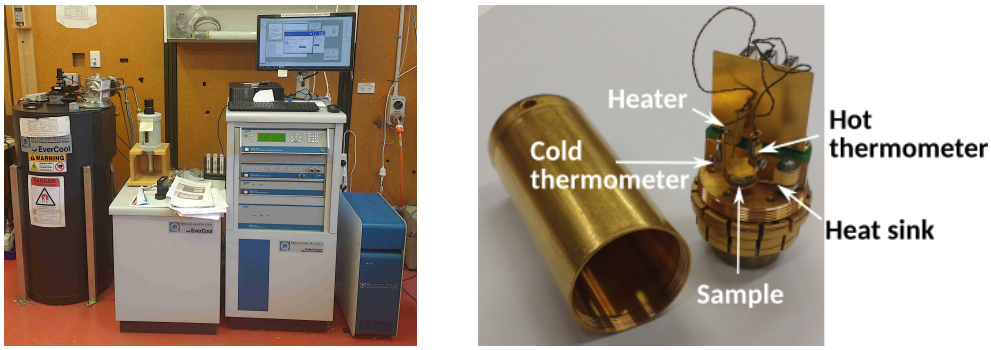

(a) (b)

Figure 3.1 (a) The PPMS instrument including magnet (grey), cooling system and console. (b) TTO puck with heater and thermocouple sensor shoes.

For resistivity measurements such as Hall effect and longitudinal magnetoresistance, the samples were mounted on different sample holders, called *pucks*. The *AC Transport* (ACT) option was primarily used in this project to measure the AC resistivity, DC resistivity for Hall effect, and longitudinal and transverse magnetoresistance (MR). Further details of the preparations are given in Ch.5.

A very important feature of the AC Transport option is the possibility to investigate a given sample property as a function of the sample orientation with respect to the direction of the applied magnetic field, which is implemented through a full circle single axis sample rotator. This function is particularly important since any geometrical misalignment of the sample's orientation can be corrected by measuring the sample at two different angles, e.g. 0° and 180°, and 90° and 270°.

The *Thermal Transport Option* (TTO) also comes with a hardware component, a software package and a special probe which is shown in Fig. 3.1(b). The main function is to measure the thermal properties of a given sample that include thermal conductivity and Seebeck coefficient, bur also electrical resistivity. Together, this allows the determination of the material's figure-of-merit. In addition, it is also possible to measure these properties in the presence of an applied magnetic field.

3.2.2 PPMS sample preparation I: resistivity, Hall effect, and magnetoresistance

The preparation for experiments using the ACT option comprises a number of stages. First, as will be discussed in detail in Ch.5, a sample has to fulfil several conditions. In the current project, predominately pressed and sintered pellets from a well ground powder were used. By that, a proper contacting of the sample is ensured.

From a given pellet, a rectangular piece is cut which dimensions should obey

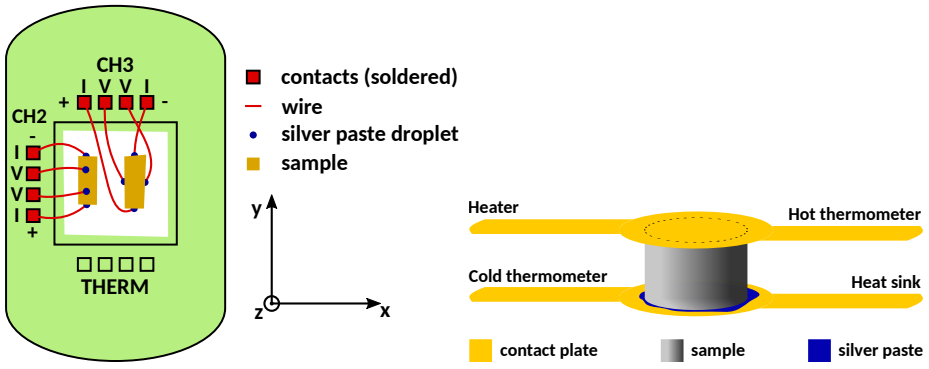

(a) (b)

Figure 3.2 (a) Scheme of a ACT puck showing the arrangement of a sample for resistance/magnetoresistance on the left and for Hall effect on the right. (c) A cylindrical sample arrangement between two gold coated electrodes as used for TTO measurements.

$l > w > h$ (*l*ength, *w*idth, *h*eight or thickness). Usually, such a sample is of several millimetres in length, about a millimetre in width and less than half a millimetre in thickness. The cuboid is placed on an alumina (Al_2O_3) substrate by using some grease to keep it attached.

The next stage is to attach the leads to the sample. To do so, short pieces of uninsulated Cu wire (50 μm in thickness) are attached to the edges of the alumina plate using *GE low temperature varnish* (GE 7031) from CMR-Direct.[7] GE varnish is a non-permanent adhesive widely used in low temperature applications. It can be removed with a 1:1 mixture of toluene and ethanol. To achieve a contacting with the sample, conducting silver paste *EPO-TEK H20E* from *Epoxy Technology, Inc.*[8] was used. The 2-components of the silver epoxy are mixed in the desired quantity and transferred as tiny droplets to connect the wires with the sample. The silver epoxy is cured for 2 hours at 90 °C.

The alumina substrate with wires and sample is placed in the square field in the middle of the puck (cf. Fig.3.2(a)) and fastened with *GE varnish*. The open ends of the wires are then soldered to the contacts on the puck. Thereby, the preparations are complete. The puck carrying the sample are then inserted into the single axis goniometer.

Fig. 3.2(a) shows the configurations of the sample, for resistivity/magneto-resistance (*left*) and Hall effect (*right*). With the sample rotator, it is possible to change the relative orientation of the drive current, I, with respect to the applied magnetic field (B). The puck can be rotated about the x-axis in the figures. In case

[7] CMR-Direct, Somersham, UK
[8] Epoxy Technology, Inc., Billerica, MA, USA

of magnetoresistance, two orientations were used in most of the measurements as discussed in Ch.6 in order to access and subtract resistivity contributions that are originating from Hall effect. On the other hand, when measuring Hall effect of a given sample, the Hall voltages were taken for 0° and 180° which then allows one to remove offsets and misalignments from sample contacts and any magnetoresistance contributions.

3.2.3 PPMS sample preparation II: thermoelectric properties

The thermal transport properties of a given material are measured on a separate TTO puck as shown in Fig.3.2(b). In this work, the 2-terminal sample mounting method was used to accommodate the cylindrical shape pellets, which have been pressed and sintered from powder sample. The pellets had a diameter of 3 mm and heights 1.5 to 3 mm. Gold coated Cu disks from Quantum Design were used as contact-electrodes. They were attached onto the samples by applying a thin layer of EPO-TEK H20E silver epoxy onto the sample's surfaces as schematically depicted in Fig.3.2(b). The heater and thermocouple sensor shoes (Fig.3.1(b)) were then attached on the ends of electrodes, and the whole assembly was encased in a cylindrical heat shield to prevent heat loss during measurements.

The basic principle of TTO measurements are as follows. The heater shoe provides the heat (and drive current for resistivity measurements) to create a temperature gradient across the sample. The temperature difference is measured through the thermocouple shoes. The monitoring of the heat drop across the sample as function of time allows one to measure the material's thermal conductivity. While the concurrent monitoring of the voltage-drop across the sample via the sample thermocouple shoes enables the determination of the Seebeck coefficient. In addition, the a four -contacts configuration can be used to measure the sample's resistivity with or without an applied temperature gradient.

3.3 System accuracy

In order to relate experimental results and their intrinsic errors, some basic system properties are listed in the following table (Tab.3.1).

Table 3.1 System accuracy of the PPMS for the two measurement options used in this work. The drive current, I, is given as the available range.

option	I	V	ρ	angle	κ	S	ZT
ACT	10 μA - 2 A	20 nV	0.03 %	0.05°			
TTO	$\leq$ 200 mA		0.03 %		$\pm$5 %	$\pm$5 %	$\pm$5 %

3.4 Magnetic Property Measurement System

3.4.1 Working principle

The Magnetic Properties Measurement System (MPMS) consists of a variable superconducting magnet ($\pm$6 T), a pick-up coil set connected to a Superconducting QUantum Interference Device (SQUID), and a console to operate experiments. The external magnetic field can be adjusted to any field and then be used in *persistent mode*, which means that no further driving current is needed, or hysteresis mode, which requires a driving current. However, unlike the PPMS, the MPMS is not set-up to perform continuous measurements in a sweep mode, which makes measurements more time consuming.

The sample chamber is thermally separated from the liquid Helium bath of the superconducting magnet. It is equipped with two thermometers providing temperature control with a common PID (proportional-integral-derivative) feedback controller between 2 and 400 K. The temperature is changed by a variable flow of cold He gas provided at the very bottom of the magnet. The He gas flows through an additional tube enclosing the sample chamber that is separated from the Dewar of the superconducting magnet by a vacuum barrier. Inside the sample chamber, the heat is further transferred via a He gas at low pressure. Temperature stabilisation is provided by two built-in heaters, one at the inlet of the He gas and a second one that directly warms up the sample chamber.

The key components of the MPMS are the detection coil operating in a second-order (second derivative) configuration and the SQUID sensor. A schematic of the general arrangement is presented in Fig. 3.3(a). The detection coil is made from a single superconducting wire surrounding the sample tube at the centre of the superconducting magnet. The upper and the bottom single loop coils are wound clockwise while a double turn, counter-clockwise coil is placed exactly in their middle (the direction of the current is indicated by the grey arrows in Fig. 3.3(a)). The pick-up coil is 3 cm in length. The arrangement is chosen in order to minimize background effects mainly coming from the external magnetic field and to make the

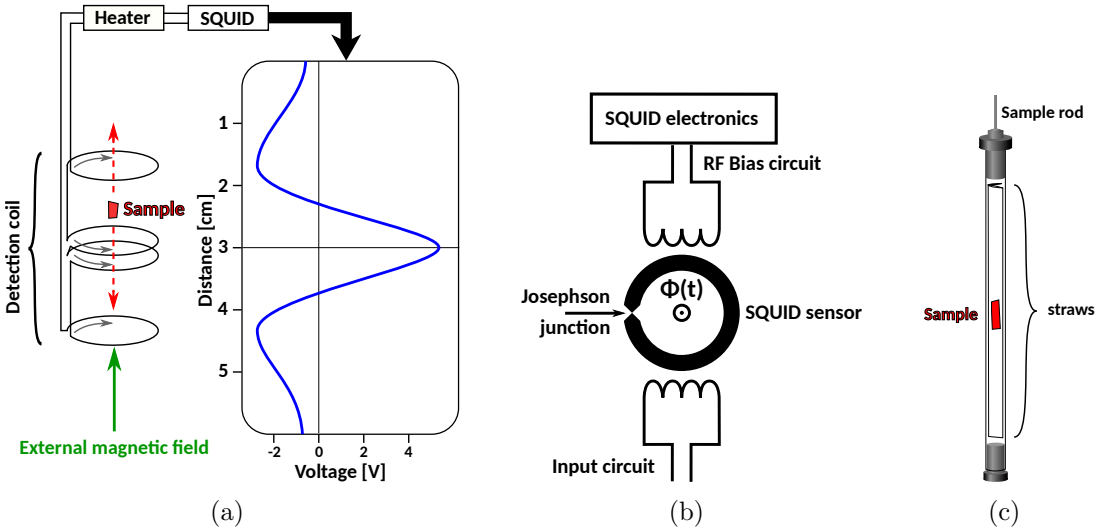

Figure 3.3 (a) Scheme of the MPMS pickup coil and the corresponding signal if a samples moves through. The signal is proportional to the sample's magnetic moments.(b) Schematic of a rf-SQUID including the sensor with a Josephson junction. (c) Sample mounting for a MPMS measurement using the "straw-within-a-straw" method.

system to be more immune to noise.

A sample moving through this gradiometer couples inductively to the detection coil, inducing an electrical current. A heater is implemented in the superconducting detection circuit that is used to quench any persistent current induced in the system during the measurements especially when charging the external magnetic field. The RF SQUID sensor, a superconducting loop with a single *Josephson junction*, is coupled inductively to the detection circuit as well as to a RF driving circuit as depicted in Fig. 3.3(b). Any time dependent signal from the detection coil will induce a current in the SQUID loop which in turn changes V_{rf} of the bias circuit. The SQUID acts as a bridge between input and output circuit that allows the signal to pass through only in multiples of magnetic flux quanta,

$$\Phi_0 = \frac{2\pi\hbar}{2e} \,. \tag{3.1}$$

Thus, the RF SQUID sensor essentially *digitises* the signal from the detection coil. It acts as an extremely sensitive and highly linear current-to-voltage converter. The voltage as function of sample position (Fig. 3.3(a) blue graph) is analysed through a fitting profile. The results are directly converted into the sample's magnetic moment μ in units of $[\mu] =$ emu which is relate to SI units by

$$1\,\mathrm{emu} = 1000\,\mathrm{Am}^2 \,. \tag{3.2}$$

Table 3.2 The magnetic moment, μ, given in different units. Here, the common SI units are used, which are A for amperes, m for meters, ρ gives the mass density, B the external magnetic field in Tesla, and M the magnetisation. Furthermore, μ_B denotes Bohr's magneton, M_mol the molar Mass, FU the chemical formula unit, N_A the Avogadro constant, and N_MI represents the relative number of magnetic impurities per formula unit.

	μ_FU $[\mu_\mathrm{B}/FU]$	μ_MI $[\mu_\mathrm{B}/MI]$	M [A/m]	χ [1]
with μ [Am^2]	$\mu \cdot \frac{M_\mathrm{mol}}{mass \cdot N_\mathrm{A} \cdot \mu_\mathrm{B}}$	$\mu \cdot \frac{1}{N_\mathrm{MI}} \frac{M_\mathrm{mol}}{mass \cdot N_\mathrm{A} \cdot \mu_\mathrm{B}}$	$\mu \cdot \frac{\rho}{mass}$	$\mu \cdot \frac{\mu_0 \rho}{mass B}$

In the course of analysing the magnetic properties of a sample under investigation, it can be helpful to express μ in terms of other units or to convert it into the magnetisation M or the system's susceptibility χ (see Tab.3.2).

3.4.2 Sample mounting

In this work, sample mounting was done by the "straw-within-a straw" method as depicted in Fig. 3.3(c). In this set-up, a sample is placed inside a plastic straw and is held against its inner wall by a shorter straw folded length-wise in half. The sample is kept in a certain position solely by friction without using any adhesive. The advantage of using plastic straws is that they are long and homogeneous compared to the detection coil's full extent. Thus, the background originating from the sample holder will not induce any signal because it does not change when the sample is moved through the gradiometer.

The length of the outer straw is about 15 cm and both ends are capped with two small caps which also act as a connection (top cap) to the sample rod. The sample rod is connected to a transport mechanism outside the sample chamber that can operate at different oscillation frequencies. In the present work, 0.5 Hz was used for all the measurements.

In order to have a reliable measurement of the magnetic moment using the above introduced experimental setup, a sample has to be small compared to the dimension of the pickup coil. The sample can then be approximated as a point dipole. The MPMS used in this work is limited to samples with dimension of about 5 mm in all directions. Typical sample prepared for the experiments were less than 6 mm in length, 1 to 2 mm in widths and less than 1 mm in thickness. Here, the length is the dimension in the direction of the movement and, thus, along the external field. The samples were cut either from pressed and sintered pellets or from larger single crystals.

Before any measurement can be started, an installed sample needs to be *centred*

within the detection coils. To do so, a preliminary stage implemented in the software allows single measurements at any magnetic field in order to adjust the sample transport, i.e. to position the sample exactly within the gradiometer.

Chapter 4

Methods II: nuclear magnetic resonance

In the second part of methods, a closer look at the experimental setup and measuring details used for NMR experiments is provided. Basic hardware components as superconducting magnets and NMR spectrometers will be introduced first. Under signal optimisation, the general performance of such a system as a whole will be discussed, including limitations connected with the circuit and the sample. Finally, the various kinds of experiments used in the present work will be introduced.

4.1 NMR hardware components

4.1.1 Magnets

Throughout the whole project presented within this work, commercial persistent mode superconducting magnets by *Bruker*[1] were used, providing most stable and highly homogeneous magnetic fields. Field strengths of 2.35 T, 7.05 T, 9.39 T, 11.74 T, and 17.64 T were available, that correspond to proton resonance frequencies of 100 MHz, 300 MHz, 400 MHz, 500 MHz, and 750 MHz, respectively.

In these magnets, the superconducting solenoid that provides the magnetic field is submerged in a liquid helium bath which is thermally separated from the interior, a wide bore (diameter 87 mm) that contains the NMR probe carrying the sample, and from a liquid nitrogen bath on the outside. The thermal insulation is achieved with high vacuum gaps.

The bore provides enough space for the shimming system[2] and a whole variety

[1] Bruker Corporation, Billerica, MA, USA

[2] The shimming system, which is an additional set of coils, allows a fine adjustment of the

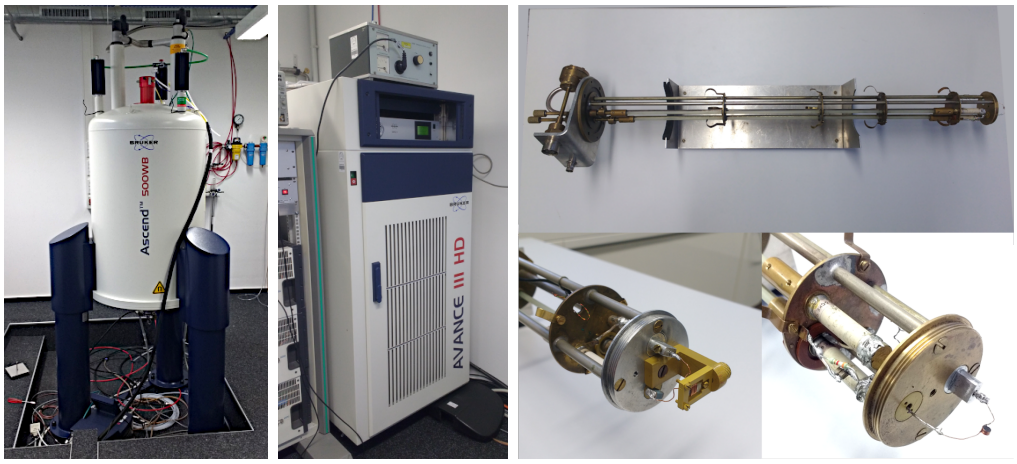

(a) (b) (c)

Figure 4.1 (a) The *Bruker Acsent 500WB* magnet providing 11.74 T. (b) A *Bruker* AVANCE III HD console. (c) A homebuilt probe head (*upper*) carrying the rf-circuit on its far right end to be positioned at the center of the magnetic field. *Below* details of two different rf-circuit set-ups, including a single-axis goniometer to measure single crystals for various relative orientations with respect to B_0 (*lower left*) and a simple solenoidal coil containing a powdered sample fixed in epoxy resin (*lower right*).

of NMR probes, including cryostats for low temperature experiments, probes that allow magic angle spinning (MAS), and sophisticated multi-channel probes (e.g. for cross polarisation and other techniques). In the current work, however, only homebuilt NMR probe heads (cf. section 4.1.3) were used at room temperature.

4.1.2 NMR consoles

Three different NMR spectrometers were used that usually belong to different magnets. At lower fields, 2.35 T and 7.05 T, as well as at the maximum field of 17.64 T, APOLLO consoles from *Tecmag*[3] were used. The maximum power output is 500 W. Time resolution is limited to 100 ns which converts into a spectral filter of 10 MHz in range. These spectrometers have the important advantage that they can be moved and relocated to operate measurements at different magnetic field. The Tecmag console comes with its own NMR software, i.e. TNMR, to operate and analyse NMR experiments.

There are stationary consoles used within this project, which is firstly the AVANCE 750 spectrometer by Bruker operating the experiments at the 17.64 T magnet. The high power amplifier allows 1000 W output signal in maximum. The time resolution

external magnetic field B_0.

[3]Tecmag, Inc., Houston, TX, USA

is 200 ns. Experiments are carried out via the *Topspin 2.0* software by Bruker.

The AVANCE III HD by Bruker is another console type used. These systems operate NMR measurements at the 9.4 T and 11.74 T magnets. The maximum power level is 500 W. With 100 ns, the time resolution is enhanced with respect to the older AVANCE console that combined with appropriate filter settings (> 5 MHz) allows a much improved access to broad NMR resonance lines.

4.1.3 Resonance circuit

Throughput the project, RLC (resistivity-inductance-capacity) resonance circuits mounted on homebuilt probe heads were used. The circuit serves as signal transmitter and receiver. A diagram is presented in Fig.4.2. The basic components are variable tuning and matching capacities C_{T} and C_{M}, and the rf-coil L that contains the sample.

Typically, the geometry and dimension of the rf-coil is set by the sample in order to achieve best possible NMR signals (this refers to the *filling factor* which is discussed in the next section 4.2). With coil dimensions of a few millimetres this results in typical inductances of NMR coils (including a contribution from the leads) in the range of several tens to hundreds of nH. For resonance frequencies around 10^2MHz (depending on isotope and magnetic field B_0) and

$$\omega = \frac{1}{\sqrt{(C_{\mathrm{T}} + C_{\mathrm{M}})L}} \ , \tag{4.1}$$

capacities, $C_{\mathrm{T/M}}$, in the order of pF are needed.

The homebuilt probes used in this work are equipped with commercial variable capacities ranging between 1 and 20 pF. Adjusting them individually allows an accurate *tuning* of the circuit's resonance frequency following Eq.(4.1). In order to further shift the resonance frequency, an additional capacity, C_+ (Fig. 4.2), can be integrated either in series for higher ω, or parallel for lower ω.

The matching capacity C_{M} is needed to couple in the circuit in the course of an experiment, and to receive signals. For an optimal signal transmission, the circuit must be *matched* to $Z_0 = 50\,\Omega$ of the spectrometer (impedance matching).

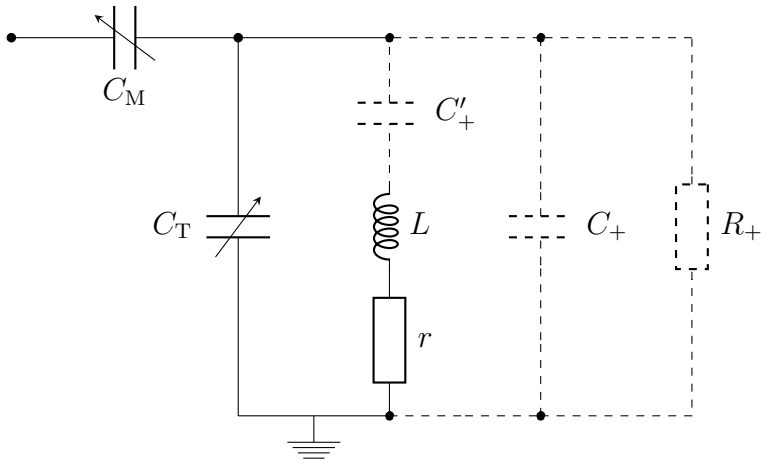

Figure 4.2 Resonance circuit as used in NMR experiments in this work. The *dashed* components can be added optionally in order to change certain circuit properties, since capacities C_{T} and C_{M} are permanently fixed to the probe, while the coil's geometry is defined by the sample limiting its size and number of turns.

4.1.4 Circuit performance

All the losses associated with resistances of the circuit components and the wiring are combined in the serial resistance r (cf. Fig. 4.2). Together with the inductance L, one defines the circuit's quality factor

$$Q = \frac{\omega L}{r} \ . \tag{4.2}$$

More generally, Q is defined by the fraction of energy lost per cycle

$$Q = 2\pi \frac{E_0}{\Delta E} \ , \tag{4.3}$$

In the frequency domain, the system's quality factor corresponds to the *bandwidth*, B, as

$$Q = \frac{\omega_0}{B} \ . \tag{4.4}$$

When driving a circuit with carrier frequency ω, Q is a measure of how efficiently energy can be stored in the system, depending on the resonance offset $|\omega - \omega_0|$. This has serious consequences for NMR measurements, when regarding the issue in the context of the circuit's tuning and matching. Driving a circuit off resonance essentially means impedance matching being violated and, therefore, the power transfer is reduced. Similarly, a signal with frequency ω received through the resonator − i.e.

picking up an oscillating voltage induced by nuclear spins − is attenuated depending on its frequency offset.

On the other hand, the quality factor Q amplifies a signal on resonance,

$$U_{\text{induced}}(\omega_0) = U_0(\omega = \omega_0) \cdot Q \ , \tag{4.5}$$

for both, signal transmission and detection.

In summary, a resonance circuit's quality factor Q has significant impact on the resonator's performance during an NMR experiment. In section 4.2 this problem is addressed in more detail.

4.2 Signal optimisation

An NMR signal is commonly characterised by its *signal-to-noise ratio* (SNR). In NMR, SNR relates the voltage induced in the rf-coil arising from nuclear spins (U_{ind}) to the thermal noise from the circuit's resistance (U_{noise}), i.e. $SNR = U_{\text{ind}}/U_{\text{noise}}$. Both contributions can be expressed in terms of the circuit's properties and the nuclear system, yielding the approximate expression for a solenoid,

$$SNR = \eta \frac{N_{\text{c}} A_{\text{c}} \omega_0 \mu_0 M_0}{\sqrt{4 r k_{\text{B}} T B}} \ . \tag{4.6}$$

Here, the rf-coil is represented through the number of turns N_{c}, the cross-sectional area A_{c}, and its rf-resistance r, including the bandwith B (Eq.4.4). T gives the temperature of the experiment and μ_0 and k_{B} represent the permittivity of the vacuum and the Boltzmann constant. ω_0 is the resonance frequency of the nucleus with gyromagnetic ratio γ, at an applied magnetic field B_0. With Curie's law, the total macroscopic magnetisation arising from a single species of polarised nuclear magnetic moments takes the form

$$M_0 = \frac{N}{V} \frac{\gamma^2 \hbar^2 I(I+1) B_0}{3 k_{\text{B}} T} \ , \tag{4.7}$$

where N/V denotes the number of resonant nuclei per unit volume, I is their nuclear spin and $\hbar$ is the reduced Planck's constant. Finally, η in (4.6) is called the filling factor which relates a given sample to the density of magnetic flux generated by the rf-coil, which is usually approximated as the ratio of the rf-coil's and the sample's volume, ranging between 0 and 1.

With Eqs. 4.6 and 4.7 an NMR experiment can be prepared towards the best

possible outcome depending on gyromagnetic ratios, γ, the magnetic fields, B_0, and the temperatures, T. Achieving $\eta \approx 1$ can be crucial. To further increase the SNR, a high quality factor, $Q = \omega_0/B$, reduces the noise while increasing the induced voltage (4.4) but in turn limits the range of exciting and receiving off-resonance signals.

Signal averaging, i.e. a coherent repetition of an experiment, further increases the SNR of an experiment. Any real physical signal will increase proportionally to the number of individual experiments, so-called *scans*, while the random noise only increases with $\sqrt{scan}$. Thus, the SNR grows with $\sqrt{scan}$.

4.3 Pulse sequences

The fundamental tool in pulsed nuclear magnetic resonance is a rectangular pulse characterised by its carrier frequency ω, the pulse length τ and its amplitude U_0,

$$U(t) = U_0 \mathrm{e}^{i\omega t}\Big|_{-\frac{\tau}{2}}^{+\frac{\tau}{2}} . \tag{4.8}$$

The Fourier transform (FT) of (4.8) is a *Sinc*-function,

$$\mathcal{F}(U(t))(\omega) = \frac{\sin(\omega\tau)}{\omega\tau} \equiv \mathrm{sinc}(\omega\tau) . \tag{4.9}$$

$1/\tau$ gives the linewidth of the sinc function. In order to excite an NMR signal properly, the linewidth associated with the pulse must be sufficiently big, such that $1/\tau > \Delta\omega$. In the present work, $1/\tau$ will be called the *excitation width* of the pulse. Similar to what is found for the circuit's bandwidth (4.4), the excitation width determines how effective the energy is brought into the system as a function of the distance to ω. Or, in other words, an NMR line off resonance will see a lowered rf-amplitude compared to the resonant case.

4.3.1 Free induction decay

Exciting a resonance with a single pulse as represented by (4.8) will give rise to the *Free Induction Decay* (FID) of the given spin system if the carrier frequency matches ω_0 and pulse length and power are adjusted to fulfil the $pi/2$-condition (2.26). The characteristic decay time is denoted as T_2^* which is related to the linewidth, $\Delta\omega$, of the FID's Fourier transform as shown by Hahn [92].

With equations (2.24) and (2.26) as introduced in Sec.2.3, the pulse length re-

quired to rotate M_0 into the xy-plane is

$$\tau_{\pi/2} = \frac{\pi}{2\omega_{\mathrm{rf}}} = \frac{\pi}{2\gamma B_1} \ . \tag{4.10}$$

The strength of the rf-field generated in the coil can be approximated with

$$B_1 = \sqrt{\frac{\mu_0 Q P}{4\pi f V_c}} \ . \tag{4.11}$$

Here, P denotes the pulse power level, f the resonance frequency in Hz and V_c the rf-coil's volume.

4.3.2 Nutation

The oscillating voltage induced across the rf-coil is proportional to the projection of M_0 on the xy-plane,

$$U_{\mathrm{ind}} \propto M(\varphi) = M_0 \sin(\omega_{\mathrm{rf}}\tau) \tag{4.12}$$

which assumes its first maximum for the condition (4.10), as depicted in Fig.4.3. Thus, a most simple NMR experiment is given by a set of measurements in which the nutation angle, $\varphi = \omega_{\mathrm{rf}} \cdot \tau$, is stepwise increased either by changing τ or the pulse power level P. Such an experiment is called a *nutation*.

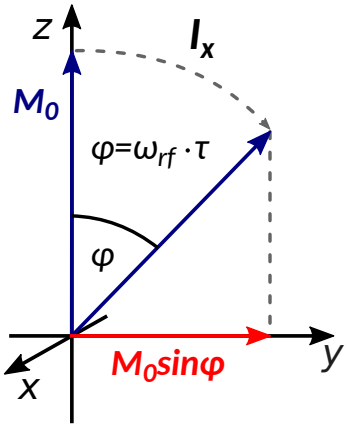

Figure 4.3 Nutating M_0.

In Sec.2.3.2 it is shown that the effective $\tilde{\omega}_{\mathrm{rf}}$ can depend on the interactions affecting the spin-system and the excitation details. In case of a selective excitation of a quadrupolar split spin system, $\tilde{\omega}_{\mathrm{rf}}$ can significantly enhanced (see equation (2.41) and [83]). Thus, the nutation experiment can be used to investigate a spin system affected by quadrupole interaction, a method which is known as *nutation spectroscopy*. This method is a key tool in the investigation of ^{209}Bi nuclei in Bi_2Se_3 as reported in Sec.8.

4.3.3 Echo experiments

To circumvent the dead time of an NMR spectrometer and to access broad resonance lines, echo experiments are widely used. First observed and described by Hahn [93] and evaluated in the presence of a moderate quadrupole interaction by Haase and Oldfield [94], an *echo* follows *two* pulses separated by a time period τ_Δ. The *Hahn*

or *Spin-echo* pulse sequence has become one of the basic tools in NMR of solids. The pulse sequence reads

$$\frac{\pi}{2} - \tau_\Delta - \pi - \tau_\Delta - echo \ . \tag{4.13}$$

A π-pulse following an initial $\pi/2$-pulse after a time τ_Δ, refocusses $M_0(xy)$ (the transverse magnetisation) by reverting the effect of dephasing induced by reversible processes. This set of pulses gives rise to an *echo* after another time period τ_Δ. A spin-echo can only be received if

$$T_2^* < T_2 \tag{4.14}$$

holds. Obviously, the pulse separation time τ_Δ needs to be smaller than the spin system's T_2.

A similar experiment is the *Solid* or *Quadrupole-echo* sequence [95–97], featuring two $\pi/2$-pulses separated by a time duration τ_Δ, i.e.

$$\frac{\pi}{2} - \tau_\Delta - \frac{\pi}{2} - \tau_\Delta - echo \ . \tag{4.15}$$

It is used to collect coherences of a spin system subject to quadrupole interaction.

4.3.4 Measuring relaxation

The echo amplitude in a Hahn or solid echo experiment depends on the system's transverse relaxation as discussed in Sec.2.3. Hence, the sequence (4.13) can be used to determine the system's T_2. A typical T_2 experiment is a set of i measurements with

$$\frac{\pi}{2} - \tau_{\Delta_i} - \pi - \tau_{\Delta_i} - echo \ , \tag{4.16}$$

where τ_{Δ_i} is gradually increased. T_2 is then given by the characteristic decay time of the echo amplitude as function of τ_{Δ_i}.

In order to measure spin-lattic relaxation of a given spin system *recovery* experiments are employed. *Saturation recovery* reads the z-magnetisation after an initial saturation $\pi/2$-pulse as function of the recovery time, $\tau_{\Delta_{T1}}$, i.e.

$$\frac{\pi}{2} - \tau_{\Delta_{T1}} - read. \tag{4.17}$$

Relatedly, inversion recovery uses a π-pulse to invert M_z initially,

$$\pi - \tau_{\Delta_{T1}} - read. \tag{4.18}$$

In both cases, (4.17) and (4.18), the *reading* can be done by an FID or an echo experiment. In the most simple case, the intensity of the *reading* signal depends on $\tau_{\Delta_{T1}}$ as

$$M(\tau_{\Delta_{T1}}) = M_0 \left(1 - f \exp\left(-\frac{\tau_{\Delta_{T1}}}{T_1}\right)\right) \ , \tag{4.19}$$

where $f = 1$ and $f = 2$ for saturation and inversion recovery, respectively, and M_0 corresponds to the fully relaxed spin system.

4.4 Shift determination

In this work orderthe secondary reference method introduced by Harris et al. [98] is used to determine the NMR shift of a spin species in the sample under investigation, The method uses tetramethylsilane (TMS), the common reference for ^{1}H NMR, as an universal reference. For this purpose, Harris et al. [98] provide a comprehensive table containing conversion factors, i.e. frequency ratios Ξ, that allow to relate a measured shift to a common reference sample to that of TMS.

The procedure used in later chapters is as follows: the relative shift of, e.g., ^{209}Bi (^{125}Te) in Bi_2Se_3 (Bi_2Te_3) is measured with respect to ^{63}Cu in the rf-coil. This allows a measurement of the shift without changing the setup. With the shift of ^{63}Cu in Cu metal, -3820 ppm given in Lutz et al. [99], that the shit of its reference $[Cu(CH_3CN)_4][ClO_4]$ from Lutz et al. [100], -1820 ppm, and the frequency ratio of the latter Cu as given in Harris's table, $^{63}\Xi = 26.515473$, the ^{63}Cu shift with respect to TMS can be calculated.

At last, with the frequency ratio of the common Bi (Te) reference $Bi(NO_3)_3$ (Me_2Te), $^{209}\Xi = 16.069288$ ($^{125}\Xi = 31.549769$), the actual shift of ^{209}Bi (^{125}Te) measured in a given sample can be related to $Bi(NO_3)_3$ (Me_2Te).

Chapter 5

Sample preparation and basic characterisation

This Chapter documents the single crystal growing and and processing, as well as basic sample characterisations using powder XRD and electrical transport measurements. A detailed description of the synthesis procedure is given first. Following that, a complete set of XRD data and the results obtained by Hall effect measurements will be presented. The last part provides an overview of the samples their properties that will be investigated in subsequent chapters.

5.1 Crystal synthesis

In order to make samples of pure Bi_2Te_3 and Bi_2Se_3 with different carrier concentrations, the materials' inherent self-doping mechanism was driven by changing the relative amount of the precursors going into the synthesis process. In the case of Bi_2Te_3 a stoichiometric and a Te excess sample were prepared. Mn doped Bi_2Te_3 was made by adding the appropriate molar ratio of Mn to the Bi and Te precursors. Bi_2Se_3 crystals were prepared from a Se excess, a stoichiometric, and a Se deficient precursor ratio. A detailed record of all the samples prepared in this thesis are listed in Tab.5.1.

All the precursors ($\geq$99.99 % purity) from *Sigma Aldrich* were mixed inside an ultra-pure Argon gas-filled glovebox and loaded into quartz tubes. The quartz tubes were then evacuated, sealed, and placed into a vertical furnace for the heat treatment process. The heating schemes for the synthesis of the different compounds shown in Fig. 5.1.

Table 5.1 Precursor quantities used during the synthesis. The list documents the individual composition of the melt single crystals were grown from.

sample/melt	mass(Bi)	mass(Te/Se)	mass(Mn)	atomic ratio [%]
$Bi_{1.88}Te_3$	5,9878 g	5,84016 g		38.5/61.5
$Bi_{2.00}Te_3$	1.5814 g	1.4496 g		40/60
$Mn_{0.03}Bi_{1.97}Te_3$	1.0354 g	0.9616 g	0.0054 g	0.78/39.36/59.86
$Mn_{0.06}Bi_{1.94}Te_3$	1.0244 g	0.9673 g	0.0083 g	1.2/38.8/60
$Bi_{1.95}Se_3$	1.9349 g	1.1246 g		39.4/60.6
$Bi_{2.00}Se_3$	1.9788 g	1.1215 g		40/60
$Bi_{2.05}Se_3$	1.9999 g	1.1058 g		40.6/59.4

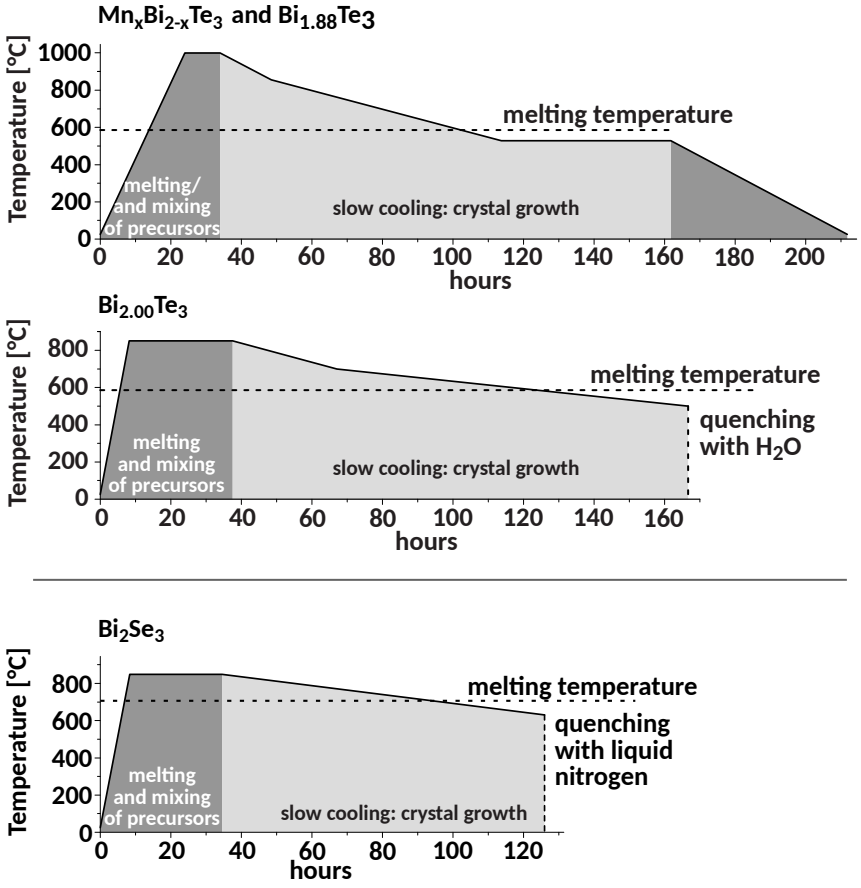

Figure 5.1 Heat schemes applied for the various materials during the synthesis.

Cylindrical ingots between 1 and 2 cm in length with typical reflective (metallic) surface were obtained from the synthesis (Fig. 5.2(a)). The ingot could easily be broken into smaller pieces, which reveals a rich abundance of smaller shiny single crystals (Fig. 5.2(b)). Some of the multifaceted pieces were picked and ground to fine powder using a mortar and pestle. Single faceted large single crystal pieces were kept aside and could be further cleaved with care into smaller pieces. The

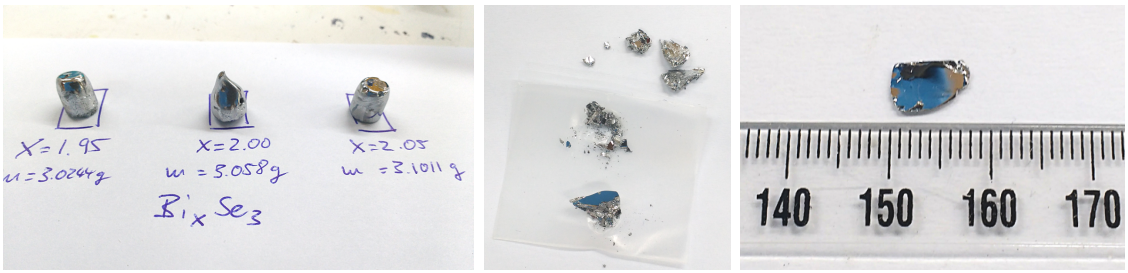

(a) (b) (c)

Figure 5.2 (a) Ingots as obtained from the synthesis of Bi_2Se_3 with different melt compositions. (b) Breaking the ingot reveals the facet of a large single crystal. (c) A cleaved single crystal with perspective onto the (001)-plane. Scale in mm.

extracted crystals are up to 7mm in length and width, and about 1 mm in thickness (Fig. 5.2(c)). Note that due to the layered nature of the materials with weak van-der-Waals interactions connecting the quintuple layers,[1] the cleaved single crystals naturally have a flat, plate-like shape. Such crystals typically have their shortest dimension, i.e. the plate's height, along the crystal's *c*-axis, which can thus be used to identify the crystals' lattice orientation. This could be verified by XRD.

5.1.1 Pelletizing and sintering

For electrical transport measurements using the PPMS it is desirable to use pressed pellet samples obtained from ground and sintered powders. The chief reason comes down to the layered structure of Bi_2Te_3 and Bi_2Se_3. Crystals tend to be micaceous and the layers sometimes delaminate by reason of which the interlayer coupling is lost at low temperature. This causes false resistance readings and compromises the interpretation of the results obtained. In that regard, it has previously been found that pressed pellet samples have much lower resistance, plus the advantage of being able to be cut into various shapes, which can improve the accuracy of the measurements and thus their results. Experiments that use pressed pellet samples include resistivity, Hall effect, thermal conductivity, Seebeck Coefficient, and magnetisation measurements.

The preparation of a pellet sample follows several steps. First, pieces from the ingot were ground into fine powder for 20 to 30 min using a mortar and pestle. There is no reason to perform the grinding under an inert atmosphere because bulk Bi_2Te_3 and Bi_2Se_3 are not known to be sensitive to oxidation at ambient conditions. To achieve a fine powder, the pieces were ground in anhydrous hexane (C_6H_{14}). After

[1] In contrast to strong covalent bonds within a QL.

the hexane had complete evaporated the ground powder is pressed into pellets of 3 to 6 mm diameter using a die-press. Single or multiple pellets of the same sample were then sealed in evacuated quartz tubes and sintered at temperatures just below the melting temperature (for $Bi_2Te_3 \sim 535\,°C$, for $Bi_2Se_3 \sim 685\,°C$). The sintered pellets are then cut into the required shape and dimensions for particular measurements.

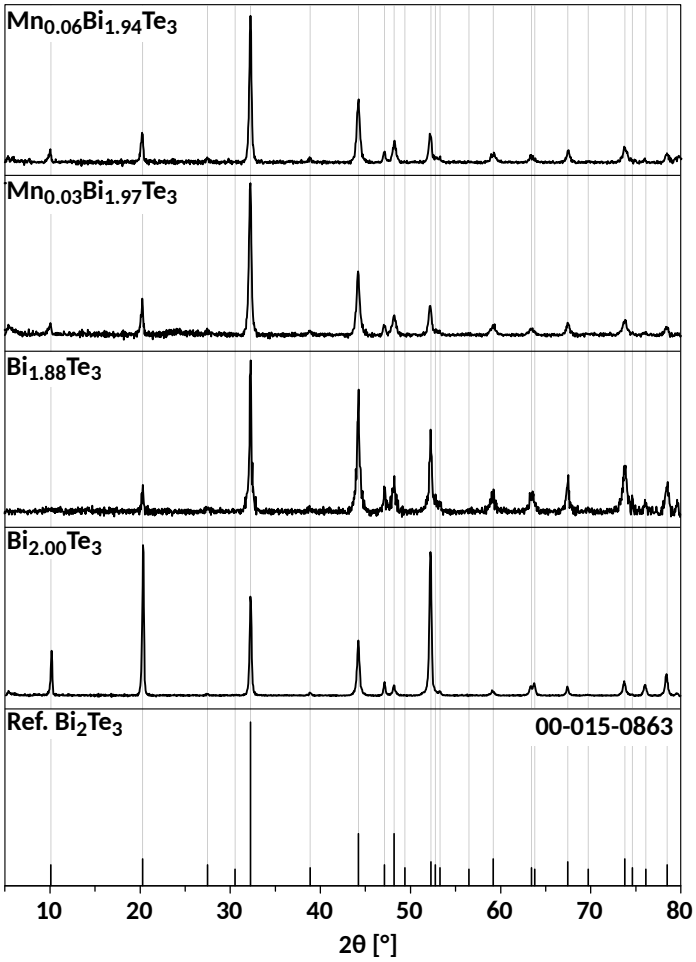

Figure 5.3 Complete set of XRD data for the four Bi_2Te_3 samples synthesised during this project. The bottom panel shows the corresponding reference patterns and its *pdf* number.

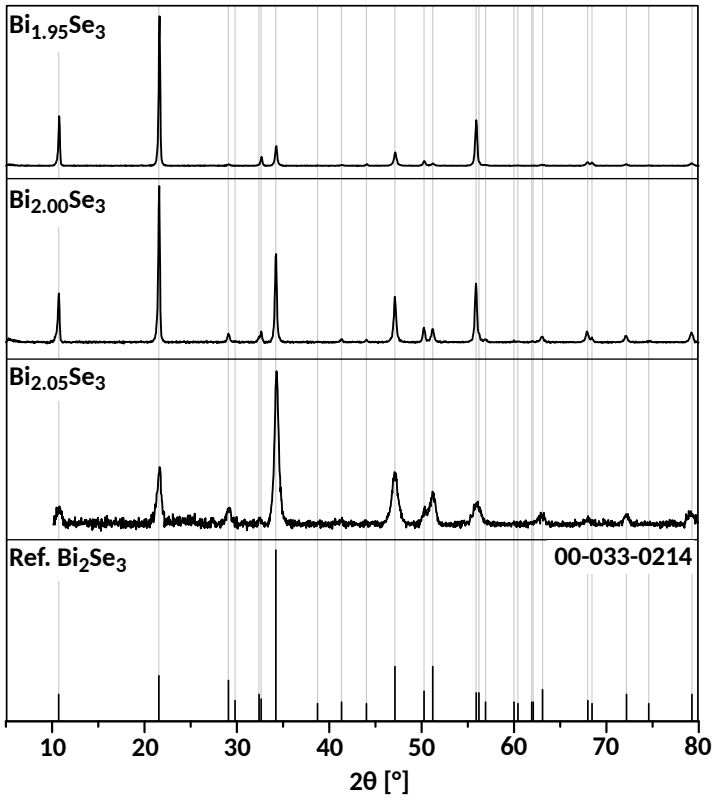

Figure 5.4 Complete set of XRD data for the three Bi_2Se_3 synthesised during this project. The bottom panel shows the corresponding reference pattern with its *pdf* number.

5.2 X-ray diffraction

Powder XRD was used to characterize all the materials prepared in the course of this project. XRD patterns were collected using the following scan parameters:

- between 5° and 80°
- 0.05° steps
- 60 min total experimental time

The complete set of data including reference patterns are organized in Figs. 5.3 and 5.4.

The investigated powders obtained from grinding using a mortar and pestle, were analysed with *X'Pert HighScore* software and matched with a corresponding reference pattern (bottom patterns in Figs. 5.3 and 5.4). Prior to matching, the background has been subtracted, and the the K-α contribution was removed. The matching score (no match = 0, perfect match = 100) for all samples was found to be between 65 and 75. The reference patterns are of *star* quality (highest quality).

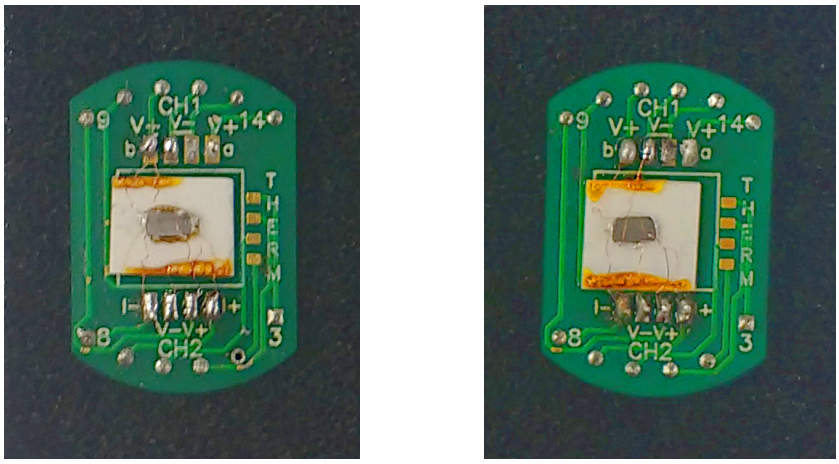

(a) (b)

Figure 5.5 Pucks prepared for Hall effect measurements with (a) $Bi_{2.00}Te_3$ and (b) $Bi_{2.00}Se_3$. The samples are pieces cut from pressed and sintered powder pellets. Note that for both samples the Hall effect has been measured twice through two channels (two sets of Hall contacts).

For all samples, each reflection can be identified with the corresponding reference pattern confirming the prepared materials to be phase pure. A number of reflections in the experimental patterns do not match the intensities of the reference pattern. The mismatch is attributed to the different experimental conditions and sample preparations, especially since the powder samples were obtained by grinding pre-synthesised single crystals. During the preparation of the XRD measurements, the individual grains in the powder may come to rest in a preferred orientation, likely with c perpendicular to the sample holder since both, Bi_2Se_3 and Bi_2Te_3, are layered materials as mentioned earlier. Hence, the as-prepared powder samples do not necessarily reflect perfectly randomised crystallite orientation. The relative intensities of individual reflections will then be different to the reference pattern, as the reference pattern is based on randomly distributed powder samples.

Using the *Topas* software by *Bruker*, the measurements were fitted in order to access lattice parameters. For all microscopic samples the fitting convincingly reproduces the measurements (data not shown). The resulting lattice parameters are all in agreement with values reported in the literature (see Tab. 5.2 for details).

5.3 Hall effect

The Hall effect is a widely used method to determine the carrier concentration, n, of a material under investigation. It is important to determine the density of free

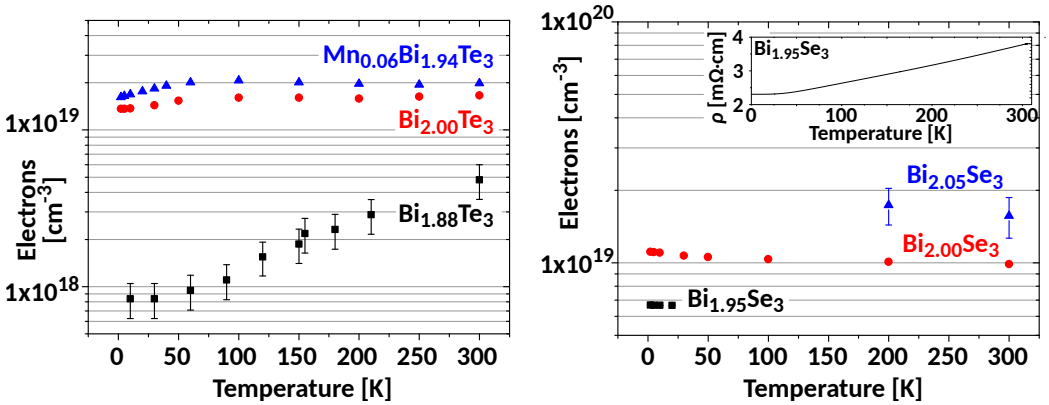

Figure 5.6 The carrier concentration as a function of temperature obtained from Hall effect measurements using eq. (2.12). There is no Hall measurement for sample $Mn_{0.03}Bi_{1.97}Te_3$. For $Bi_{1.95}Se_3$, a resistivity measurement is presented in the inset, showing a typical metallic behaviour.

carriers in the present materials as they play a crucial role for the understanding of most of the properties studied in this work.

It must be noted that the Hall effect was carried out on representative samples from the *same* syntheses batches as the single crystals which were later investigated with various methods. Thus, the results of Hall effect measurements can only provide an estimation of the carrier concentration of the crystals investigated in subsequent chapters.

Hall effect was measured for temperatures between 2 and 300 K. External magnetic fields of up to 8 T were used while the voltage was taken for each field twice, at 0° and 180°, in order to allow the removal of additional contributions from misalignment and magnetoresistance.

The hall voltage V_H as function of the external field B was analysed assuming a single carrier type density, n, as argued in previous chapters (2.12),

$$ne = \frac{BI}{V_H h} \ , \tag{5.1}$$

with the the elementary charge e, sample thickness, h, and the driving current, I. The obtained carrier concentrations as function of temperature are plotted in Fig. 5.6.

Most of the samples show no significant temperature dependence of the carrier concentration. A slight downturn of n for temperatures below 50 K is seen for $Bi_{2.00}Te_3$ and $Mn_{0.06}Bi_{1.94}Te_3$. A similar effect is found for $Bi_{1.88}Te_3$. In both cases, n decreases by about the same amount with decreasing temperature (3 –

$5 \times 10^{18}\,\mathrm{cm}^{-3}$). The changes are related to a freezing out of carriers at low temperatures. Apart from these minor variations, all samples show the expected very high carrier densities.

The intrinsic doping can be understood on a simple level when assuming a stoichiometric, i.e. 2:3 ratio, sample of Bi_2Se_3 or Bi_2Te_3 to have a considerable amount of free electrons due to Se (Te) vacancies. Reducing the Bi (Bi^{3+}) content will then result in hole doping of the system compensating a certain amount of the electrons. Excess Bi, on the other hand, drives the doping with electrons. The change in carrier concentration, however, does not reflect the variation in the composition of the melt during crystal growth. This points to a more complex chemistry connected with the self-doping effects in the present systems.

In summary, through Hall effect measurements the carrier concentration was determined to be between $10^{18}\,\mathrm{cm}^{-3}$ and $10^{19}\,\mathrm{cm}^{-3}$ for all the samples prepared in in the course of this study. The temperature dependence of the carrier densities is expected for heavily doped degenerate semiconductors.

5.4 Overview of the samples studied in this work

Table 5.2 Sample properties obtained from XRD and Hall effect measurements, comprising lattice parameters from the fitting of XRD data and the carrier concentrations. For NMR, two more single crystalline samples where investigated by Prof. Dr. C. Felser (Dresden, Germany) and Prof. Dr. K. Kadowaki (Tsukuba, Japan).

material	label/note	a/b-axis [Å]	c-axis [Å]	n [cm^{-3}]
XRD Ref. Bi_2Te_3	00-015-0863	4.3852	30.4830	
Bi_2Te_3	$Bi_{1.88}Te_3$	4.3876(12)	30.508(5)	$4.8(5) \times 10^{18}$
Bi_2Te_3	$Bi_{2.00}Te_3$	4.3848(2)	30.4950(12)	$1.7(1) \times 10^{19}$
Bi_2Te_3	$Bi_2Te_3^*$	Dresden, Germany		
$Mn_{0.03}Bi_{1.97}Te_3$		4.3842(5)	30.536(3)	
$Mn_{0.06}Bi_{1.94}Te_3$		4.3802(5)	30.521(3)	$2.2(3) \times 10^{19}$
XRD Ref. Bi_2Se_3	00-033-0214	4.1396	28.6360	
Bi_2Se_3	$Bi_{1.95}Se_3$	4.1410(3)	28.644(2)	$6.8(5) \times 10^{18}$
Bi_2Se_3	$Bi_{2.00}Se_3$	4.1409(4)	28.639(3)	$1.05(10) \times 10^{19}$
Bi_2Se_3	$Bi_{2.05}Se_3$	4.1435(4)	28.637(3)	$1.7(3) \times 10^{19}$
Bi_2Se_3	$Bi_2Se_3^{**}$	Tsukuba, Japan		

Chapter 6

Magnetic and electronic properties of Mn doped Bi_2Te_3

This chapter reports on the magnetic and electronic properties of Bi_2Te_3 and the effects caused by manganese doping. As presented in the previous chapter, powder XRD of pure and Mn doped samples show essentially no change of the lattice parameters within the resolution of the instrument (Tab.5.2). Thus, there is no evidence that a great portion of the Mn ions are intercalated in between quintuple layers and it is concluded that Mn predominantly substitutes for Bi as intended.

In the course of this study, it turns out that the effects on both magnetic and electronic properties connected to Mn doping, are unexpectedly rich. As mentioned earlier, pressed and sintered powder samples were used to ensure a reliable contacting of the samples for electrical transport measurements. It was found, however, that grinding and sintering affects the magnetic properties substantially, especially the ferromagnetic phase present in Mn doped Bi_2Te_3 single crystals which has vanished for the sintered powders. Furthermore, the sintered samples show an unexpectedly large magnetoresistance and change in sign of the thermopower while the carriers in these systems do change neither in type nor in number. These observations illustrate the complexity of the magnetic and electronic properties evidently governed by the their defect chemistry.

The chapter is divided into two parts. First, the magnetic properties of pure and Mn doped Bi_2Te_3 single crystals and sintered pellets are presented (cf. Ch.5) were used for the first part. In the second part only sintered samples were investigated with respect to their electronic and thermoelectric properties.

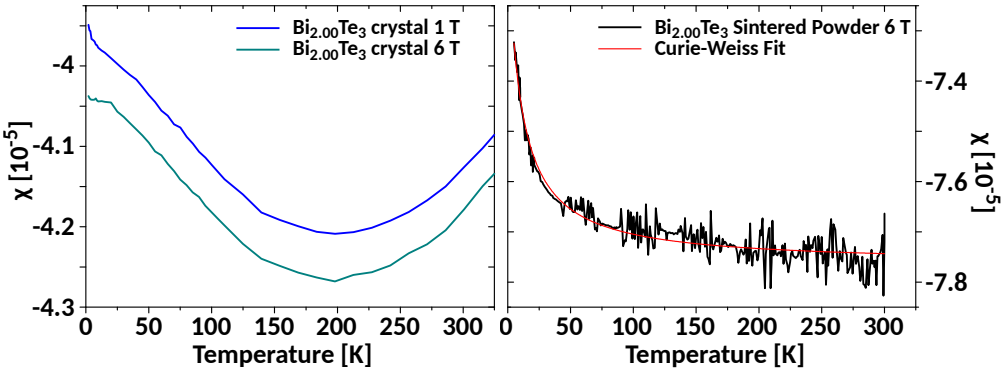

(a) (b)

Figure 6.1 Temperature dependent susceptibility obtained from $Bi_{2.00}Te_3$, as (a) measured in a single crystal with the crystal *c*axis perpendicular to the applied field, $c \perp B$ (1 T and 6 T) and (b) as obtained from a ground and sintered sample (6 T). The red solid line in (b) shows a Curie-Weiss fit. Grinding and sintering clearly introduces paramagnetic impurities most likely to be associated with Te vacancies.

6.1 Magnetic properties

6.1.1 Results

Temperature dependent susceptibility

The susceptibility of pure Bi_2Te_3 as obtained from a single crystal and a sintered powder is shown in Fig.6.1. The single crystal was oriented with the crystal *c*axis perpendicular to the applied field ($c \perp B$). The curves in Fig.6.1(a), at two different applied magnetic fields, represent the typical diamagnetic response of a doped semiconductor with a rather weak temperature dependence. There is no evidence for the presence of paramagnetic point defects. In contrast, the susceptibility of the sintered sample (Fig.6.1(b) black) presents a very different temperature dependence. It can be interpreted as a diamagnetic response with small paramagnetic contribution. A similar behaviour was also observed in Mn doped Bi_2Se_3 by Chong et al. [51]. A Curie-Weiss fit (2.20) was performed, which is represented by the red solid line in Fig.6.1(b). The Curie constant, C, is determined to be 6.59×10^{-7} K.

The Curie constant together with equation (2.20) can be used to evaluate a simple scenario where the paramagnetic ions are identified as V_{Te}^{+} vacancies occupied by a single electron with $S = 1/2$ (similar to the approach used by Chong et al. [51]). These defects will then have an effective moment of $P_{\text{eff}} = \mu_B g\sqrt{S(S+1)} \approx 1.72\mu_B$

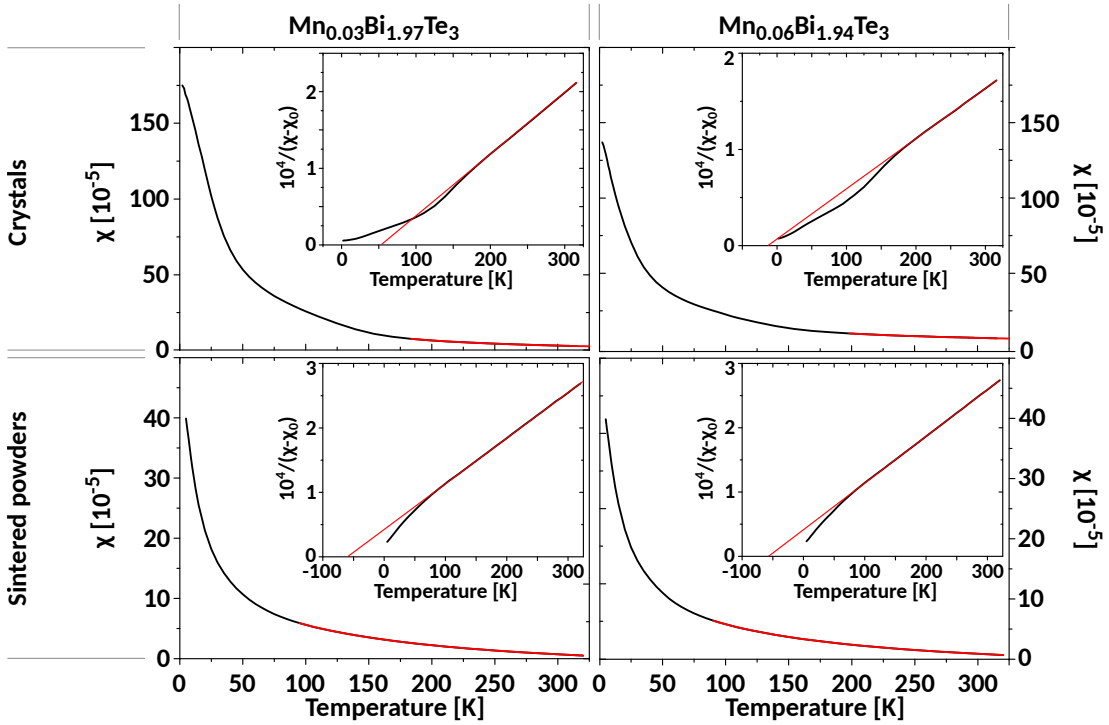

Figure 6.2 Temperature dependent susceptibility of $Mn_{0.03}Bi_{1.97}Te_3$ (left) and $Mn_{0.06}Bi_{1.94}Te_3$ (right). The upper two panels represent single crystals with $c \perp B$, the lower two panels show the results for sintered powder pellets. The red solid lines correspond to Curie-Weiss fittings (results in Tab.6.1). The insets show the inverse susceptibility plots $(1/(\chi - \chi_0))$.

with an electron g-factor of $g \approx 2$. With

$$C = \frac{n_\mathrm{p}\mu_0 P_\mathrm{eff}^2}{3k_\mathrm{B}} = 6.59 \times 10^{-5}\,\mathrm{K}\ , \tag{6.1}$$

the corresponding density of paramagnetic centres, n_p, can be derived and translated into a Te deficiency of about 0.05 %, using mass density and the molar mass of Bi_2Te_3.[1]

The effect of Mn doping is considered next. In Fig.6.2, the temperature dependence of the susceptibility of $Mn_{0.03}Bi_{1.97}Te_3$ and $Mn_{0.06}Bi_{1.94}Te_3$ is shown. Again, single crystalline samples with $c \parallel B$ (Fig.6.2, upper two panels) and sintered powder samples (Fig.6.2, lower two panels) were studied.

All samples show a clearly paramagnetic response as expected from Mn doping. The paramagnetic region of the single crystals can be traced down to ∼150 K and ∼170 K for $Mn_{0.03}Bi_{1.97}Te_3$ and $Mn_{0.06}Bi_{1.94}Te_3$, respectively. The low temperature non-paramagnetic regions (non-linear regions in the $1/(\chi - \chi_0)$ plots - cf. Fig.6.2, insets) of the crystals are rather peculiar. It is remarkable that evidently θ has

[1] $\rho = 7.7\,\mathrm{g/cm^3}$ and $M_\mathrm{mol} = 800.761\,\mathrm{g/mol}$

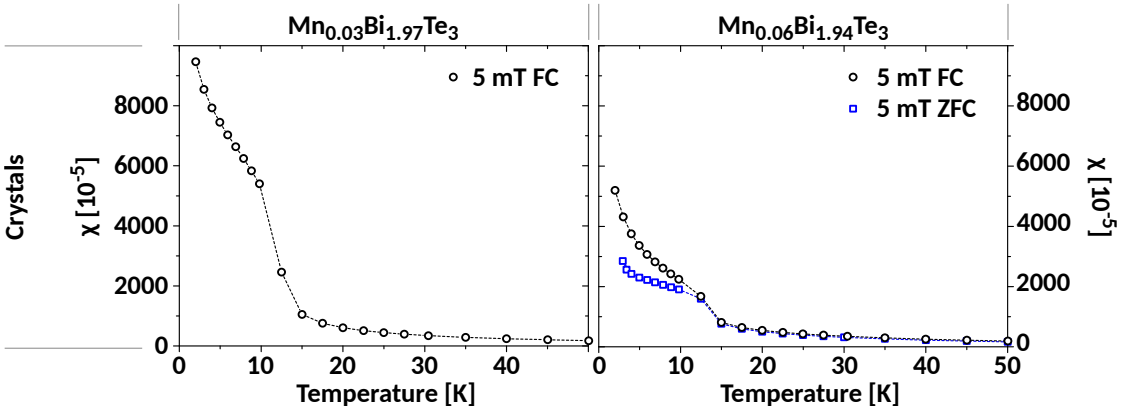

Figure 6.3 Low field susceptibility (5 mT) of $Mn_{0.03}Bi_{1.97}Te_3$ (left) and $Mn_{0.06}Bi_{1.94}Te_3$ (right) for temperatures below 50 K. The sudden step around 15 K (17 K) marks the ferromagnetic transition.

opposite sign when comparing $Mn_{0.03}Bi_{1.97}Te_3$ ($\theta = 53$ K) and $Mn_{0.06}Bi_{1.94}Te_3$ ($\theta = -14$ K).

After sintering, both samples show a very similar behaviour with a paramagnetic region down to ∼90 K and negative θ as shown in Fig.6.2, lower two panels. The results of the Curie-Weiss fittings, as represented by the red solid lines, are collected in Tab.6.1.

In Fig.6.3, the low field susceptibilities of $Mn_{0.03}Bi_{1.97}Te_3$ and $Mn_{0.06}Bi_{1.94}Te_3$ crystals are presented. In both samples a clear step in the susceptibility is seen around 15 K, that is a sign for a magnetic transition. The sudden jump in susceptibility points to a spontaneous alignment of magnetic moments, i.e. indicates a ferromagnetic (FM) transition. The presence of a ferromagnetic phase in crystals of Mn doped Bi_2Te_3 is proven by the typical S-shape ferromagnetic field-loop curves and the hysteresis at low temperatures as shown in upper panels of Figs.6.4 and 6.5. The FM transition temperature, T_{Curie}, is estimated from the susceptibility measurements to be about ∼15 K for $Mn_{0.03}Bi_{1.97}Te_3$ and ∼17 K for $Mn_{0.06}Bi_{1.94}Te_3$.

Magnetic field dependence

For the single crystals, the magnetic moment saturates for sufficiently large magnetic fields and low enough temperatures (Fig.6.4). Remarkably, for both samples the saturation moment per Mn ion, μ_{Mn}, deviates from the effective moment, P_{eff}, as obtained from the Curie-Weiss fitting by about a factor of two (cf. Tab.6.1).

The field dependent measurements have been repeated for the ground and sintered samples at 5 K and 20 K. The results are shown in the bottom panels of Figs.6.4 and Fig.6.5. Down to 5 K, no hysteresis in the field loops is observed, in

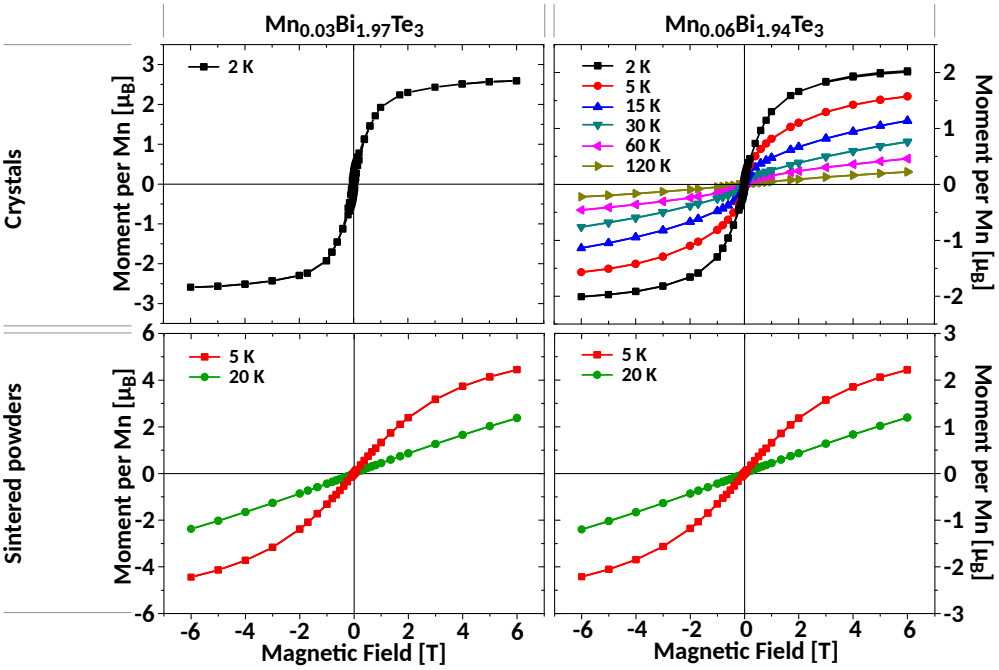

Figure 6.4 Magnetic field dependence of the moment per Mn ion for $Mn_{0.03}Bi_{1.97}Te_3$ (left) and $Mn_{0.06}Bi_{1.94}Te_3$ (right). The upper panels present the results obtained from single crystalline samples, the bottom panels the measurements of sintered powder samples.

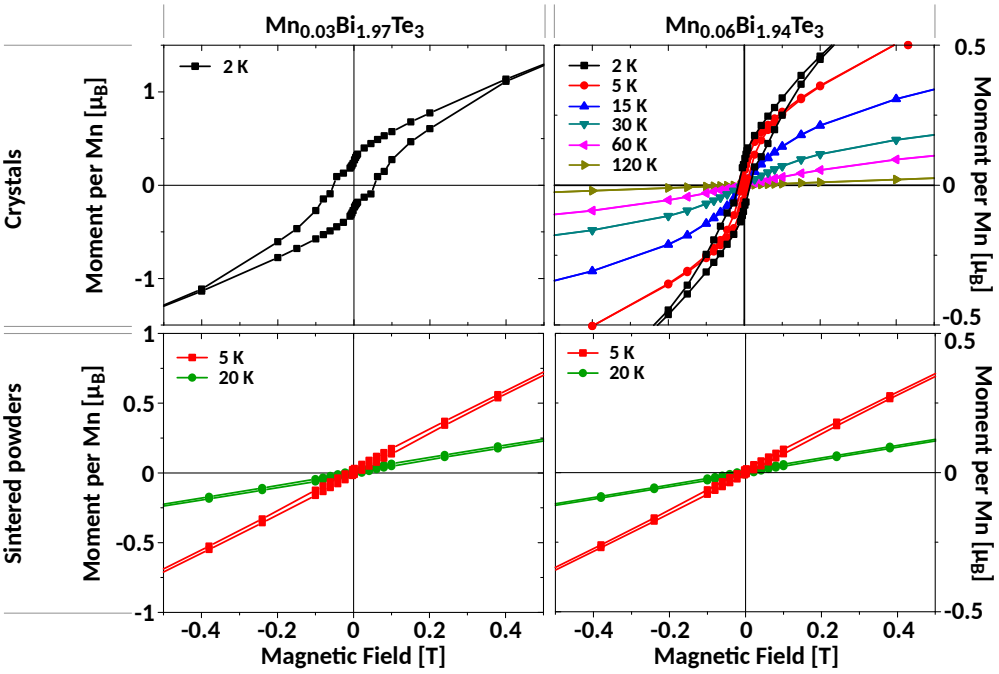

Figure 6.5 Enlargement of the low field region of the measurements shown in Fig.6.4. Both single crystalline samples (upper panels) show magnetic hysteresis for temperatures of 5 K and below. The ferromagnetic ordering seems to disappear with grinding and sintering.

agreement with the temperature dependent susceptibilities and the negative θ from the Curie-Weiss fittings (Fig.6.4, bottom panels, and Tab.6.1), which suggest an antiferromagnetic ordering of the magnetic moments. Furthermore, the magnetic moment per Mn at 6 T has slightly increased during the sintering, while the S-shape of the field loop suggests that a saturation could be achieved for temperatures below 5 K. Apart from the slightly higher moment per Mn and the absence of a hysteresis, this behaviour seems to be similar to the unprocessed crystals.

Together with the the temperature dependent susceptibility measurements as shown above, the results on the magnetic field dependence obtained from ground and sintered samples of previously ferromagntic materials constitute a highly unusual and unexpected finding. Evidently, the magnetic ordering mechanism is severely affected by processing the samples.

The following table provides an overview of the individual properties as obtained from the measurements mentioned above.

Table 6.1 Magnetic properties of single crystals and sintered powders of Mn doped Bi_2Te_3, $Mn_xBi_{2-x}Te_3$. θ and P_{eff} were obtained from Curie-Weiss fittings, T_c were estimated from the temperature dependent susceptibility, and μ^*_{Mn} were obtained from low temperature field loops.

x	θ [K]		T_{curie} [K]		P_{eff} [μ_B/Mn]		μ^*_{Mn} [μ_B/Mn]
	crystal	sintered	crystal	sintered	crystal	sintered	crystal
0.03	~ 53	-61	~ 15		5.24	5.59	2.6
0.06	~ -14	-58	~ 17		4.6	3.9	2.0

*at 2 K and ∼6 T

6.1.2 Discussion

Ferromagnetism

Mn doped Bi_2Te_3 single crystals show ferromagnetic ordering even at doping levels as low as 3 % Mn. The ferromagnetic transition was found to occur at about 15 K and 17 K for $Mn_{0.03}Bi_{1.97}Te_3$ and $Mn_{0.06}Bi_{1.94}Te_3$, respectively, in agreement with the presence of magnetic hysteresis at temperatures below the Curie temperature, T_{Curie}. Literature provides studies of doping levels from 2 % to 15 %[2] and corresponding transition temperatures, T_{Curie}, from 9 to 17 K of macroscopic samples [52, 60, 62,

[2]Note, sometimes x% Mn doping refers to $Mn_xBi_{2-x}Te_3$ and in other cases to $Mn_{x/2}Bi_{2-x/2}Te_3$. In the present study the first convention is adopted.

63, 65] and thin films [70–72]. The variations of T_{Curie} may be related to the way the transition temperature is determined. A clear relation between Mn content and T_{Curie} was not found.

In qualitative agreement with ferromagnetic ordering is the positive $\theta = 53\,\mathrm{K}$ found for $Mn_{0.03}Bi_{1.97}Te_3$. The negative $\theta = -14\,\mathrm{K}$ obtained for $Mn_{0.06}Bi_{1.94}Te_3$ means that a ferromagnetic phase as well as an additional unordered paramagnetic phase with antiferromagnetic correlation are present. Such a scenario will account for the discrepancy found for the effective moment per Mn as obtained from the Curie-Weiss fits and the saturation at 2 K (P_{eff} and μ^*_{Mn} in Tab.6.1). The antiferromagnetic coupling in the spin-disordered paramagnetic phase will yield a cancelling of the corresponding magnetic moments and, thus, a reduced total moment. The difference of about a factor of 2 for both samples argues in favour of a rather large portion of such an additional paramagnetic phase, i.e. representing about half of the sample under investigation. Thus, the materials appear composite-like.

Indications of an inhomogeneous magnetism with a ferromagnetic as well as a paramagnetis phase in Mn doped Bi_2Te_3 single crystals has not been reported so far. Publications show temperature dependent susceptibilities with Curie-Weiss behaviour down to 30 K and less [52, 60, 62–65]. Moreover, values of θ obtained from Curie-Weiss fittings coincide with the ferromagnetic transition temperatures, T_{Curie}. Also different in comparison to the present work, is the observation of rather small saturation fields. Saturation of the magnetic moment is achieved at fields between 0.1 T [62] and 2 T [52, 60]. For the samples studied in the present work, a considerably higher field is of 6 T and more is required (Fig.6.4). The striking difference between earlier publications and this work might indicate very different samples in terms of the defect chemistry. In this context, it is remarkable that the ferromagnetic transition was found at similar temperatures as reported.

It should be noted that the finding of two phases, a ferromagnetic next to a paramagnetic one, could easily be explained by an accumulation of Mn ions forming Mn clusters. In this scenario, a long range ordering that characterises dilute ferromagnets would not be required. This, however, was not observed in the literature. Furthermore, since the ferromagnetic phase disappears with sintering, such a scenario would require an efficient dispersion of the Mn ions across the samples which is not expected from sintering below a system's melting temperature.

From the small amount of magnetic ions it is inferred that Mn doped Bi_2Te_3 indeed represents a dilute ferromagnet. The coupling between these distant moments is by some authors argued to arise from indirect exchange interaction of RKKY type (cf.

Ch.2.3) via conduction electrons [63–66]. This interpretation, however, is in contradiction with experimental observations of a carrier density independent T_{Curie}, reported by Watson et al. [62]. Furthermore, several studies investigating thin films that, as mentioned above, show very similar transition temperatures, T_{Curie}, explicitly state that there is no evidence of a correlation between the presence of carriers and ferromagnetism.

The current study cannot contribute evidence on whether or not the type of interaction among Mn moments is RKKY. A more systematic study of samples with a large variation of carrier concentrations at the same Mn doping level is required, because an RKKY type of interaction should depend on the density of states, and must therefore change with the carrier concentration.

Effective moment per Mn

The magnetic moment per Mn as obtained from the Curie-Weiss fittings for the single crystalline samples were found to be $5.24\,\mu_{\mathrm{B}}$ and $4.6\,\mu_{\mathrm{B}}$ for $Mn_{0.03}Bi_{1.97}Te_3$ and $Mn_{0.06}Bi_{1.94}Te_3$, respectively. The sintered samples show similar values (Tab.6.1). These results are in agreement with the literature, where the effective moment is reported to vary between $\sim 4\,\mu_{\mathrm{B}}$ and $5.8\,\mu_{\mathrm{B}}$ [60, 62, 63, 65]. There seems not to be a strict dependence of the moment with respect to the Mn content.

For $Mn_{0.03}Bi_{1.97}Te_3$ the effective moment obtained from the paramagnetic region is with $P_{\mathrm{eff}} = 5.24\,\mu_{\mathrm{B}}$ close to what is expected for Mn^{2+} (high spin configuration, $S = 5/2$), i.e. $P_{\mathrm{eff}} = 2\mu_{\mathrm{B}}\sqrt{(S(S+1))} \approx 5.92\,\mu_{\mathrm{B}}$. In the case of $Mn_{0.06}Bi_{1.94}Te_3$, however, the effective moment per Mn is reduced to $P_{\mathrm{eff}} = 4.6\,\mu_{\mathrm{B}}$. A plausible explanation for this observation of a reduced effective moment per Mn ion is a mixture of Mn^{2+} with $P_{\mathrm{eff}} = 5.92\,\mu_{\mathrm{B}}$ and Mn^{3+} with a lower spin configuration, perhaps $S = 0$, as argued by Watson et al. [62] and discussed by Antonov et al. [101]. In this scenario, the oxidation state of the Mn ion depends on the coordination of the Mn atoms and thus on their position in the lattice. Mn^{2+} is expected for Mn substituting Bi, while Mn^{3+} ions are associated with Mn atoms being intercalated in the van der Waals gap between two quintuple layers (cf Fig.1.1 and [101]).

The difference in the effective moments obtained from 3 % and 6 % can thus be interpreted in the context of the defect chemistry of the Bi_2Te_3 system. For low Mn concentrations, Mn atoms substitute preferably for Bi atoms as intended from the melt composition, $Mn_xBi_{2-x}Te_3$. For an increased Mn concentration, the used synthesis procedure may yield a material with a larger amount of intercalated Mn atoms. To achieve an effective moment of $P_{\mathrm{eff}} = 4.6\,\mu_{\mathrm{B}}$ by assuming a mixture

of Mn^{2+} and Mn^{3+} ions, the fraction of Mn^{3+} with $S = 0$ is about 20 % of the total number of Mn ions. That is, about 0.01 Mn atoms per Bi_2Te_3 unit would be intercalated. The associated change of the lattice parameters (a stretch of the unit cell along the crystal *c*-axis) is too small to be measurable with XRD, which shows no variation of the lattice parameters across the three – pure and doped – Bi_2Te_3 samples.

To sum up, the variation of the effective moment per Mn in $Mn_xBi_{2-x}Te_3$ could indicate different lattice positions of the Mn ions in the Bi_2Te_3 structure with a certain dependence on the initial Mn concentration and, perhaps, the synthesis procedure. The incorporation Mn in Bi_2Te_3 may thus depend on details of the defect chemistry of the system under investigation. A systematic study with a larger variety of samples and Mn concentrations may allow further insight and help to reveal the underlaying mechanisms that govern the creation of defects – native and foreign – in the present material.

The effect of sintering

Sintering of well ground crystals seem to change the magnetic properties rather severely. Crystals of pure Bi_2Te_3 show a typical diamagnetic response of a semiconductor with no evidence of paramagnetic point defects (Fig.6.1). After sintering, however, the situation has clearly changed and the material does now exhibit traces of paramagnetic impurities. A similar result is obtained from samples of sintered Bi_2Se_3 by Chong et al. [51]. Thus, it might be argued that this response alludes to half-filled defects due to Te vacancies which is in agreement with an estimated Te deficiency of 0.05 % as derived from the Curie-Weiss fit. The assumption is also in agreement with the general understanding of the defect chemistry in the present system. 0.05 % of half-filled Te vacancies, V_{Te}^{+}, corresponds to about $9 \times 10^{18}\,cm^{-3}$ vacancies which will then add the same number of electrons to the system. This is about half the carrier density as measured by Hall effect and, thus, a consistent result since other defects such as V_{Te}^{2+} or Bi/Te antisites may add more electrons while being magnetically neutral.

It is obvious that grinding and sintering affects the defect chemistry of a sample. The sintering process is intended to fuse the grains. Although this process was carried out below (560 °C) the melting temperature of Bi_2Te_3 (585 °C) [46], one cannot rule out introducing Te vacancies or a change in the number of Bi/Te antisite defects. It would be interesting to study the material's transport properties and see how they change with grinding and sintering, i.e. whether or not there is a

change in the carrier concentration or a deviation from a linear field dependence of the Hall coefficient. However, as mentioned above, attaching wire contacts on single crystalline samples is difficult. Other methods that do not require physical contacts, such as optical measurements and NMR, might, thus, prove to be very useful for future investigations.

For the Mn doped samples, sintering yields yet another unexpected result. Most interestingly is loss of ferromagnetic ordering among Mn moments at low temperatures. Instead, the magnetic response of both Mn doped samples, $Mn_{0.03}Bi_{1.97}Te_3$ and $Mn_{0.06}Bi_{1.94}Te_3$, is very similar. In other words, the composite-like susceptibility has changed into a paramagnetic susceptibility with an antiferromagentic ground state. The paramagnetic region is now extended to as low as $\sim$90 K for both samples and the corresponding θ are almost identical with about -60 K, a value that is much different from those before sintering (cf. Fig.6.2 and Tab.6.1).

Again, grinding and sintering will change the density of defects and perhaps the relative number of Bi/Te antisite defects and Te vacancies. The negative θ observed in the samples indicates an antiferromagnetic ordering of the magnetic moments. It might be suggested that during the sintering process, defects accumulate in the close vicinity of the Mn ions, and by that, suppress their long range interaction mediated by itinerant carriers.

In the light of the complexity of the present results obtained with a limited number of different samples, a more definite conclusion cannot be drawn at this stage. However, strong evidence is provided that the defect chemistry in the present system is perhaps more complicated than expected. Native defects may hold the key to the manipulation of magnetic properties in the present class of materials.

6.2 Transport properties

6.2.1 Results

The transport properties of Bi_2Te_3 and changes induced by Mn doping are presented in this section. All the results were obtained from ground and sintered samples, similar to those investigated in the former section. The resistivity, the Hall effect, and thermopower have been measured for each sample. From the resistivity and the carrier concentration obtained from Hall effect measurements, mobility was calculated. The results are shown in Fig.6.6.

The resistivity (Fig.6.6 top left) is found to be similar for all three compounds, i.e. the materials under investigation show decreasing resistivity with decreasing temperature. This is the typical behaviour of highly doped degenerate semiconductor with a considerable carrier concentration.

The bottom left of Fig.6.6 shows the temperature dependence of the free carrier concentrations in $Bi_{2.00}Te_3$ and $Mn_{0.06}Bi_{1.94}Te_3$ obtained from Hall effect measurements. Charge carrier densities on the order of $\sim 10^{19}\,\mathrm{cm}^{-3}$ are found. Apart from a slight decrease at low temperature, the carrier concentrations are almost independent of the temperature between 300 K and ∼100 K. Hence, the effect of Mn substitution for Bi atoms, as it appears, does not result in a large change in carrier density, at least for these ground and sintered samples.

In the simple model of a single carrier type, the electron mobility can be derived from resistivity and carrier concentration using equation (2.6). The results are presented in the top right plot of Fig.6.6. Thus, as the resistivity is reduced and the carrier density remains fairly temperature independent, the carrier mobility is seen to increase with decreasing temperature.

In another experiment, the Seebeck coefficient or thermopower, S, of all three samples was measured (Fig.6.6 bottom right). Most notably, a change in sign of the thermopower, S, from Bi_2Te_3 to $Mn_{0.06}Bi_{1.94}Te_3$ is observed. This is somewhat surprising given carrier type as derived from Hall effect does not change in sign. This must reflect a more complex origin of the thermoelectric properties in the present material.

Magnetoresistance

A comprehensive study of the resistivity as function of an externally applied magnetic field was undertaken as well. The magnetoresistance, MR, of the pressed and sintered samples was measured between 2.2 K and 300 K. For each temperature,

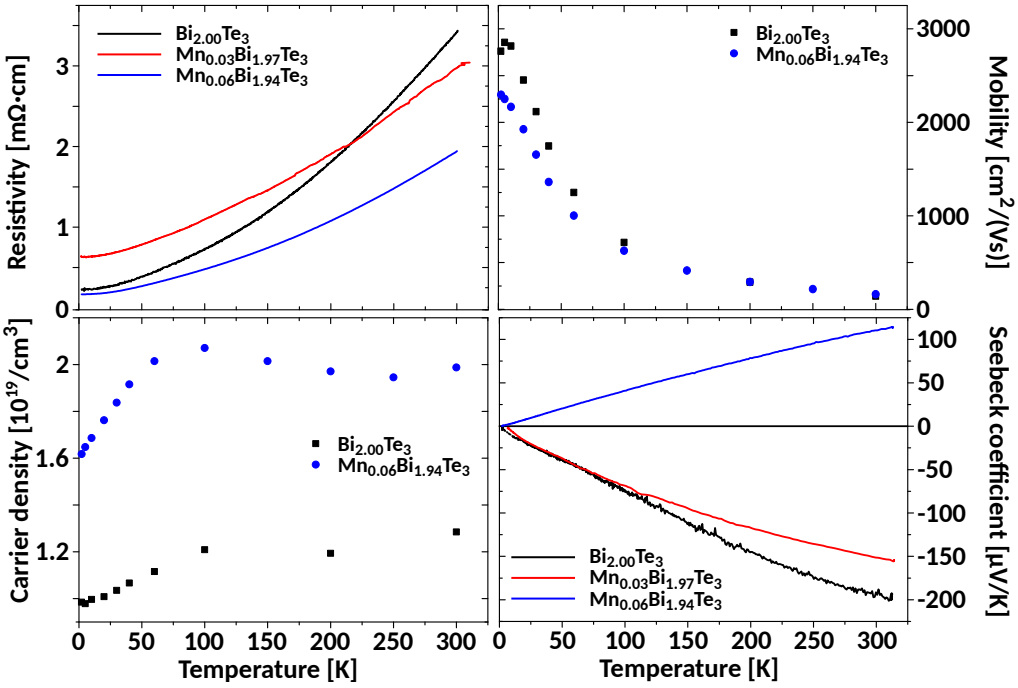

Figure 6.6 Transport properties of $Bi_{2.00}Te_3$ (black), $Mn_{0.03}Bi_{1.97}Te_3$ (red), and $Mn_{0.06}Bi_{1.94}Te_3$ (blue). Measurements were carried out on ground and sintered samples. The temperature dependent resistivity is shown on the top left. The temperature dependent carrier density from Hall is shown on the bottom left. The upper right plot shows the mobility obtained from resistivity measurements and the carrier concentration. The thermopower as a function of temperature is shown in the bottom right.

the longitudinal as well as the transverse MR was measured, i.e. with the driving current I parallel ($I \parallel B$) and perpendicular ($I \perp B$) to the external field B, respectively. The results are shown in Fig.6.7. A large MR is found at temperatures between 2.2 K and 10 K, with the highest value for the pure sample reaching almost 200 % (Fig.6.7(a), $I \perp B$). A similarly large effect is also observed in the Mn doped samples.

When rotating the sample from $I \perp B$ to $I \parallel B$, the MR is clearly reduced – a typical signature of an ordinary MR. Such a behaviour is expected because for $I \parallel B$ there is no contribution from the Hall effect. The curvature of the MR changes at approximately 100 K from concave (tangent above) at lower temperatures to convex (tangent below) at higher temperatures. The least curved MR(B) is exhibited by $Mn_{0.03}Bi_{1.97}Te_3$, which also shows the smallest MR among the set of samples measured. By rescaling the results obtained for $I \parallel B$ to $I \perp B$ (cf. Fig.6.8(a)), there is good agreement of the field dependencies for all samples.

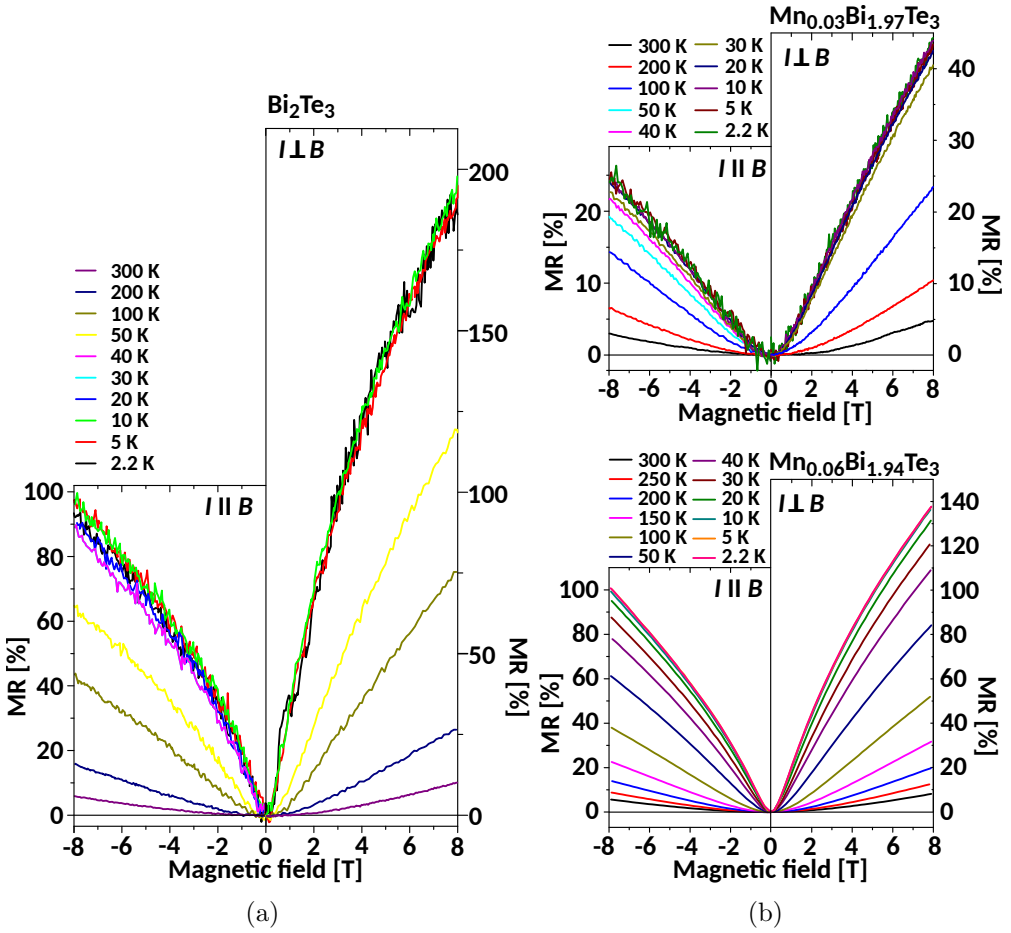

Figure 6.7 Magnetoresistance of $Bi_{2.00}Te_3$ (left), $Mn_{0.03}Bi_{1.97}Te_3$ (upper right), and $Mn_{0.06}Bi_{1.94}Te_3$ (lower right) at various temperatures and two sample orientations, i.e. $I \parallel B$ and $I \perp B$, as indicated in the plots. Measurements were carried out on ground and sintered samples.

6.2.2 Discussion

Thermopower

In the previous section, a number of interesting observations in the transport and thermoelectric properties of pure and Mn doped Bi_2Te_3 were reported. The electronic transport is essentially unaffected by Mn doping, i.e. the measured resistivities are very similar, showing a normal temperature dependent Fermi-liquid transport behaviour, while carrier concentration and type do not change considerably. It seems as if any additional carriers are compensated, perhaps by Te vacancies in the vicinity of the Mn ions.

Interestingly, the thermopower, S, changes its sign between 3 % and 6 % Mn doping (cf. Fig.6.6). The rather high room temperature values of the thermopower, S, of

$\approx -195\,\mathrm{K}$, $\approx -150\,\mathrm{K}$, and $\approx 110\,\mathrm{K}$ for Bi_2Te_3, $Mn_{0.03}Bi_{1.97}Te_3$, and $Mn_{0.06}Bi_{1.94}Te_3$, respectively, are expected for highly conductive semiconductors. The underlying trend of a reduced thermopower with incresing Mn content agrees with earlier reports [25, 48]. The temperature dependence seems to be in agreement with the corresponding resistivity, i.e. a resistivity decreasing with temperature lowers the thermopower indicating carrier diffusion to be the origin.

A direct relation between carrier type and the sign of the thermopower was used to argue in favour of a transition of Bi_2Se_3 from *n*-type semiconductor to a *p*-type semiconductor due to Ca doping [49]. Hor et al. [60] show that the carrier concentration can be considerably reduced by annealing Single crystals of Bi_2Te_3 in a Te rich atmosphere. Remarkably, they also observe that the carrier type as function of temperature measured with Hall effect changes sign, i.e. changes from electrons to holes, between 50 K and 100 K. In the same temperature range, the thermopower changes from negative to positive, in perfect agreement with the single carrier type scenario. In the present study, a change in sign of the thermopower occurs while the carrier type as obtained from Hall effect does *not* change. This seems to be a clear contradiction with a single carrier type driven thermopower.

The origin of the thermopower in Mn doped Bi_2Te_3, therefore, seems to be more complex. With the assumption of comparatively strong spatial variations of the doping that creates an inhomogeneous material with regions of higher and lower conductivity (as will be discussed in the context of the unusual strong magnetoresistance) one may find an explanation. In such a scenario, the presence of two carrier types could account for the different results obtained by Hall effect and thermopower measurements.

Magnetoresistance

Magnetic field dependent measurements of the resistivity show a large magnetoresistance for each sample at low temperatures (Fig.6.7). A maximum value of about 200 % was obtained for undoped Bi_2Te_3 at 2.2 K. Note there is no publication of the magnetoresistance of Mn doped bulk Bi_2Te_3. This result is in agreement with reports on the bulk magnetoresistance of Bi_2Te_3 in the literature [48, 59]. The results of the present study seem not to support a direct dependence of the magnetoresistance on the Mn content. In other words, the magnitude of the MR does not change systematically with Mn doping ($Mn_{0.03}Bi_{1.97}Te_3$ show the smallest MR, cf. Fig.6.8(a)). General similarities, such as the sign of the MR, the orientation

dependence ($I \parallel B$ vs. $I \perp B$) and the curvatures, remain the same for all three samples. This indicates mechanism behind the magnetoresistance is independent of Mn doping.

The MR of thinfilms of Bi_2Te_3 has been studied as well [55–57, 102]. Most authors conclude that MR arises from weak anti-localisation (WAL), others refer to quantum linear MR. The evidence for WAL is based on the assumption of a two-dimensional electronic transport and strong spin orbit coupling. Thus, one might be tempted to explain the findings in the present study in the light of a WAL mechanism, because the system under investigation is a layered compound with essentially two-dimensional transport and exhibits very strong spin-orbit coupling. However, it must be doubted that the MR in macroscopic samples originates from WAL. The magnitude of the measured MR, its field and temperature dependence observed in the present samples are not expected for WAL.

There are a number of characteristics found in the measurements that support a simple scenario based on a geometric MR. First, the measurements were carried out on ground, pressed and sintered powders with layered structure (cf. Fig.1.1). Second, MR changes systematically to smaller values when changing the sample orientation from $I \perp B$ to $I \parallel B$ for all samples, but the field dependence remains essentially the same (Fig.6.8). Furthermore, the mobility shows a similar temperature dependence.

These observations imply a rather inhomogeneous material. In a simplified model, one might consider the sample to be a network of connected high conductivity regions enclosing islands of lower conductivity. The mean distance between these regions of lower conductivity must be longer than the mean free path of the carriers. Without an external magnetic field, charge carriers choose the least hampered paths, yielding the zero field resistivity. With an increasing external field enabled, the Lorentz force increasingly forces the carriers away from their ideal path into regions of lower conductivity, resulting in higher resistivity values. In such a scenario, a higher mobility at lower temperatures, i.e. longer mean free path of the carriers, would result in a greater deviation from the optimal pathway. The low conductance islands do not change in size with temperature, which is conceivable if these region are characterised through the local defect density. Hence, the temperature dependencies of the mobility and MR are similar. Since the system is essentially two dimensional and the measurements were carried out on sintered powders, one measures a resistivity (with and without field) that reflects the mean inclination of the randomly oriented conducting 2d plates and an overall contribution from their interfaces.

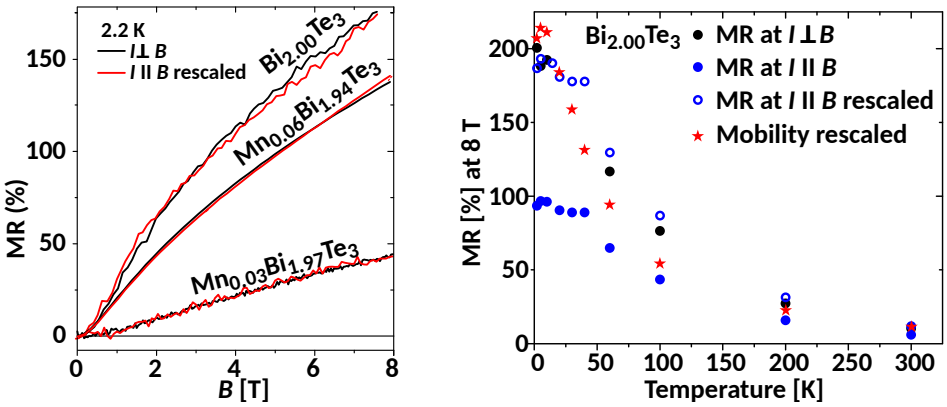

Figure 6.8 Magnetotransport at 2.2 K for $Bi_{2.00}Te_3$, $Mn_{0.03}Bi_{1.97}Te_3$, and $Mn_{0.06}Bi_{1.94}Te_3$ as indicated by the labelling. Rescaled MR for $c \parallel B$ (red) matches with MR for $c \perp B$ (black). (b) High field (8 T) MR as a function of temperature. Rescaled (open blue) MR(T) for $c \parallel B$ (solid blue) matches MR(T) for $c \perp B$ (solid black). The overall agreement of the rescaled MR at $c \parallel B$ with that for $c \perp B$ in (a) and (b) indicates geometric MR as a source. The similar temperature dependence of the mobility (red stars) in (b) supports the proposed geometric MR due to low conductivity islands as explained in the text.

The model from above was introduced by Parish and Littlewood [103]. It is related to ordinary and geometric magnetic resistance in a two dimensional network of resistors resembling inhomogeneous conductors. It is shown that such a scenario can produce MR field dependencies with different curvatures, just as found in the present samples.

Though lacking quantitative theory, the scenario above takes advantage of a simple concept without using complicated explanations of a whole variety of experimental results. However, a deeper and more systematic study, perhaps supported by theoretical calculations, is required to confirm or disprove the present hypothesis. Clarification may be sought by NMR measurements of sintered samples as used in the present study. This is because islands with low conductivity might give a very different NMR signal (shifted in frequency units) due to the eventually higher impurity densities and accompanied changes of the local electronic density of states.

6.3 Summary

Bi_2Te_3 samples doped with 3 % ($Mn_{0.03}Bi_{1.97}Te_3$) and 6 % ($Mn_{0.06}Bi_{1.94}Te_3$) were investigated with respect to their magnetic and electronic properties. Pure Bi_2Te_3 served as a reference material. Though the study investigates only a few samples, the results illustrate an unexpectedly rich collection of chemical and physical effects.

It was found that grinding and sintering of the samples changes their magnetic properties severely. Clearly, additional paramagnetic point centres are introduced in the pure sample. The long range magnetic order that gives rise to a ferromagnetic phase in Mn doped samples at temperatures below $\sim$15 K, is eliminated during the processing. The source of these significant changes must be sought in additional defects introduced by the grinding and sintering. These are most likely Te vacancies and Te/Bi antisites. It is possible that the additional defects are near the Mn and result in the loss of the long range magnetic order. The loss of the ferromagnetic order is closely tied to the its origin, i.e. the mechanism behind the long range interaction. This could be studied in an extended research programme focussing on single crystals and polycrystalline samples with a range of carrier concentrations.

Magnetotransport and thermoelectric measurements were made only on the sintered samples due to the difficulty of making good electric contacts to crystals and measuring the thermopower of small crystals using the PPMS. It was found that Bi_2Te_3 exhibits a surprisingly large, positive magnetoresistance of up to 200 %. The Mn doping, despite minor variations, appears not to change the magnetoresistance in a substantial way. The magnetoresistance is likely to be due to a geometric magentoresistance arising from spatial inhomogeneities, similar to observations of large magentoresistances in other spatially inhomogeneous materials.

Surprisingly, there is a change in sign of the thermopower from $Mn_{0.03}Bi_{1.97}Te_3$ (negative) to $Mn_{0.06}Bi_{1.94}Te_3$ (positive) while there is no evidence that the carrier concentration changes at all. This is not expected. Other studies of the same or related materials, report a change in sign of the thermopower according to the carrier type. It is possible that the finding is due to inhomogeneities, but this requires further study involving a range of Mn concentrations as well as other dopants that are known to affect the carrier concentration, as well as studies of non-stoichiometry samples.

The results from the magnetic, magnetotransport, and thermopower measurements show how important defects are for the physical properties of these systems. Furthermore, Bi_2Te_3 must be assumed to be spatially inhomogeneous. Consequently, these measurements do not necessarily provide information about the bulk of the

material. For example, the resistivity selects that fraction of the sample with the highest conductivity, while the thermopower represents low conductivity regions. These results can be compared with NMR which is a local probe averaging the whole sample.

Chapter 7

NMR of spin $1/2$ nuclei: ^{125}Te in Bi_2Te_3

In this chapter, a ^{125}Te NMR investigation of undoped Bi_2Te_3 is presented. Single crystals and powders from the two Bi_2Te_3 syntheses as reported in Ch.5 are studied. Additionally, a single crystalline sample from the Max Planck Institute in Dresden was investigated.[1]

The single crystals were placed in a single axis goniometer for orientation dependent measurements. The rf-coil was directly wound around the samples in order to achieve high signal-to-noise ratios. External magnetic fields of 7 T, 9.4 T, 11.7 T, and 17.6 T were used during the study.

To excite the spin systems, exclusively Hahn-echo pulse sequences were used (cf. Ch.4). This includes measurements of the spin-echo decay (T_2) where the pulse separation, τ_Δ was progressively increased. Using inversion recovery pulse sequences, the spin-lattice relaxation times, T_1, of individual Te signals were found to be between 50 ms and 100 ms in agreement with earlier publications [17, 25]. To ensure maximum signal intensity, the experimental repetition times were thus set to 0.5 s or longer throughout the measurements.

The chapter is organised as follows. In the beginning, measurements at the $c \parallel B_0$ orientation will be presented, and the two signals corresponding to the two crystal sites will be assigned using T_2 corrected relative signal intensities. Next, the orientation dependent NMR shift anisotropy will be measured and the result will be compared to resonances obtained from powders. The magnetic field dependent NMR linewidth will be studied next, followed by a comprehensive discussion of the results and their relation to the literature.

[1] Prof. C. Felser, Max Planck Institute for Chemical Physics of Solids, Dresden, Germany.

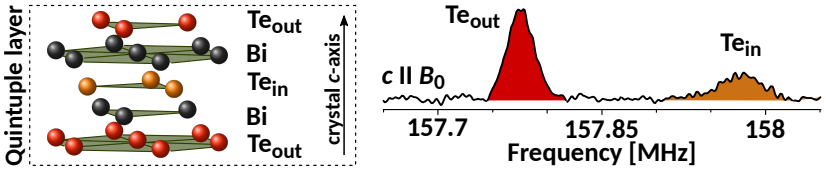

Figure 7.1 A quintuple layer of the Bi_2Te_3 crystal structure is given on the left. Signals from the outer sheets (Te_{out}) are distinguished from those of the inner sheet (Te_{in}) in an NMR experiment as can be seen on the right, where ^{125}Te Hahn-echo spectra after Fourier transform are shown. The measurements were taken from the $Bi_2Te_3^*$ single crystal at $c \parallel B_0$ in a magnetic field of 11.7 T. The label "Te_{in}" and "Te_{out}" give the crystal site assignment which is confirmed by NMR signal intensity after T_2 correction (cf. Fig.7.2).

7.1 Experimental results - single crystals and powders

Throughout the presentation of the results and in the subsequent discussion, the three different samples and corresponding powders are identified as "$Bi_{1.88}Te_3$" and "$Bi_{2.00}Te_3$", which relates them to the composition of the melt they were grown from (Ch.5). The sample from the laboratory in Dresden, Germany, is labelled as "$Bi_2Te_3^*$".

7.1.1 The $c \parallel B_0$ orientation

As shown in Fig.7.1, two separated ^{125}Te NMR signals are received from a single crystal with the crystal c-axis parallel to the external field, i.e. $c \parallel B_0$. This is expected because there are two chemically different environments for Te atoms in the crystal structure. A quintuple layer, the basic building block of the Bi_2Te_3 structure, is reproduced in Fig.7.1 on the left.

The two signals represent the two crystal sites and are conveniently labelled as Te_{in} and Te_{out} depending on their position in the quintuple layer. The local differences in their environments are the following: Te_{in} nuclei placed at the inversion centre of the system are surrounded by six Bi atoms forming an octahedron, whereas Te_{out} is neighboured by three Bi atoms and the van-der-Waals gap separating two quintuple layers, i.e. three Te_{out} atoms from the adjacent quintuple layer (Fig.1.1). A similar identification has been used for ^{77}Se NMR in Bi_2Se_3 [23] and was in the following also applied to ^{125}Te in Bi_2Te_3 [26].

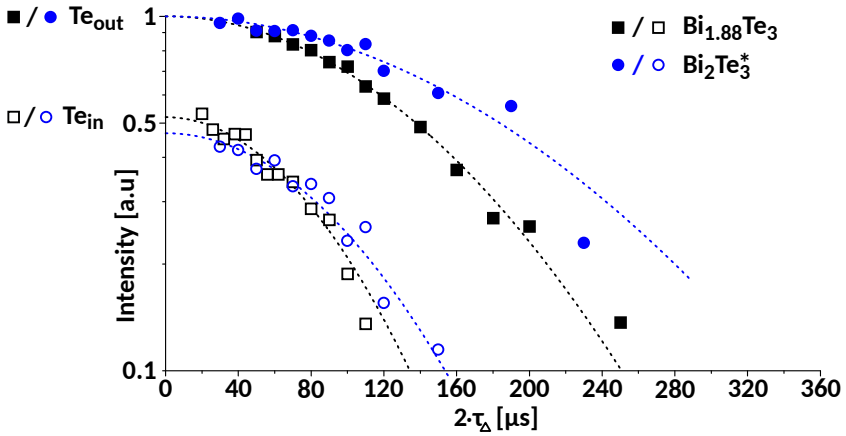

Figure 7.2 The spin echo decay presented as signal intensity vs. twice the pulse separation, $2\tau_\Delta$, for Te_{in} (open symbols) and Te_{out} (solid symbols) observed in $Bi_{1.88}Te_3$ (black) and $Bi_2Te_3^*$ (blue). The echo decays are in good approximation Gaussian as such (dashed lines). The measurements were normalised such that the Te_{out} initial intensity ($2\tau_\Delta = 0$) equals 1, in order to emphasise the inner signals, Te_{in}, to be half the intensity initially.

7.1.2 Transverse relaxation and intensity ratio

Using the relative intensity of the two Te signals, a crystal site assignment can be made, because the NMR signal intensity is quantitatively related to the number of nuclei in a given system, i.e. in case of Bi_2Te_3, there are twice as many Te_{out} in the system as Te_{in}. The results, however, need to be corrected for potential differences on the individual spin-echo decay (T_2), since echo sequences were used. This was done for the crystals $Bi_{2.00}Te_3$ and $Bi_2Te_3^*$ as shown in Fig.7.2. The signal intensities are normalised by the corresponding initial Te_{out} signal to be equal to 1. Thus, the initial intensity of the Te_{in} signals, being close to 0.5, confirms the expectation of a intensity ratio of 2:1.

The spin echo decays are very fast and slightly sample dependent, with characteristic relaxation times obtained from the Gaussian fittings of only $T_{2G} \approx 120\,\mu s$ and less. Furthermore, the spin echo decay for Te_{in} is measurably faster compared to Te_{out}. Details are tabled at the end of the results section in Tab.7.1.

7.1.3 Orientation dependence and NMR Shift

Orientation dependent measurements were carried out to trace the individual shift anisotropies of Te_{in} and Te_{out}. That is, the single crystals were stepwise rotated inside the magnetic field B_0 about an axis perpendicular to the crystal c-axis. For each orientation, the resonance frequencies of the spectra were recorded. With

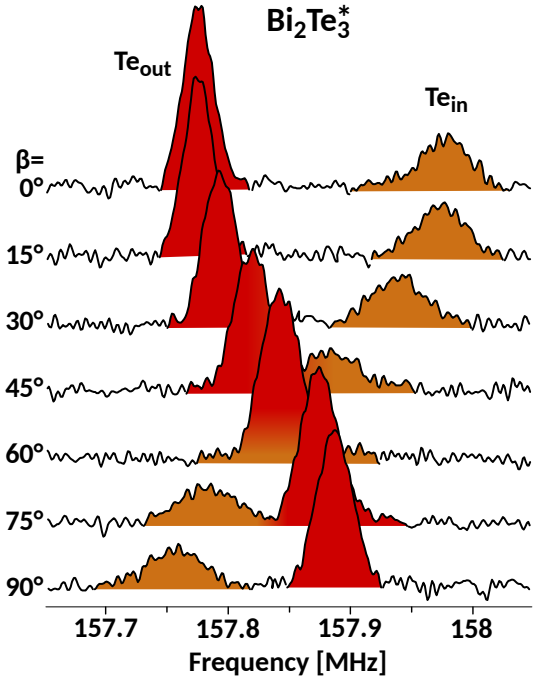

Figure 7.3 ^{125}Te Hahn echo spectra as function of the crystal orientation ($\beta = \angle(c, B_0)$). Measurements obtained from $Bi_2Te_3^*$ at 11.74 T. The individual shift anisotropies let Te_{in} and Te_{out} overlap at about 60°.

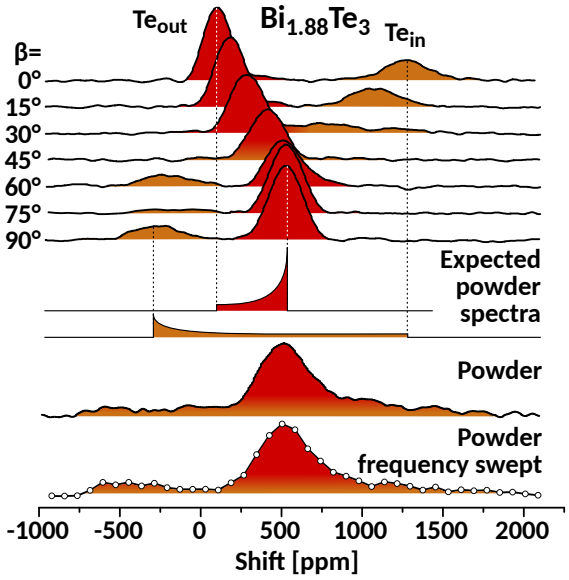

Figure 7.4 Orientation dependent Hahn echo spectra of ^{125}Te in $Bi_{1.88}Te_3$ are presented in the upper panel. In the middle, schemes of the corresponding powder spectra for axial symmetric NMR shifts are given. In the lower panel, $Bi_{1.88}Te_3$ powder spectra are presented. The upper powder spectrum was obtained by a single high power Hahn echo with $\pi/2$-pulse length of 2 μs. For the lower most spectrum, frequency stepped Hahn echo measurements (open circles) with long ($\pi/2 = 10\,\mu$s), low power pulses were employed.

the secondary reference method (Ch.4), the orientation dependent resonances were converted into the corresponding shift, K (in ppm), with respect to the common reference material Me_2Te. The orientation dependence was then fitted with

$$K(\beta) = K_{\text{iso}} + K_{\text{axial}}(3\cos^2(\beta) - 1)/2 \tag{7.1}$$

for an axial symmetric NMR shift (2.29).

Orientation dependent single crystal spectra of $Bi_2Te_3^*$ are given in Fig.7.3 (in frequency units). The colours indicate the crystal site assignment as already used in Fig.7.1. The angle β denotes the relative orientation of the crystal c-axis with respect to B_0. As the crystal is rotated away from $c \parallel B_0$ ($\beta = 0°$), both lines, Te_{in} and Te_{out}, move in opposite directions in frequency units. Close to the magic angle ($\beta \approx 54.74°$) the signals cross each others way and overlap. For larger angles β, the two signal separate again. The shift anisotropies are in good approximation axially symmetric, reflecting the cylinder symmetry of the crystal structure.

The same orientation dependent measurements were done for $Bi_{1.88}Te_3$ and $Bi_{2.00}Te_3$. The results are similar to those found for $Bi_2Te_3^*$, i.e. Te_{out} moves to higher frequencies with increasing β, while Te_{in} is shifted in the opposite direction. Again, near the magic angle, both resonance lines overlap. The shift anisotropies have axial symmetry.

For $Bi_{1.88}Te_3$, the orientation dependent spectra are depicted in Fig.7.4 in ppm. Next to the single crystal data, the expected powder spectra from the shift anisotropies are shown, in agreement with actual measurements of powder samples below. That is, since an ideal powder sample consists of a multitude of small single crystals with random orientation, a powder spectrum represents an average of the orientation dependent single crystal spectra. The average of the single crystal spectra, however, depends on the probability to find a crystallite of the powder in a given orientation. In case of axial symmetric shift anisotropy, orientation dependent single crystal spectra are weighted with $\sin\beta$ for the powder average, yielding the typical *expected* lineshape as given in Fig.7.4. Thus, in a powder of an axial symmetry shift anisotropy, the $c \perp B_0$ orientation dominates due to more possible crystallite orientations with the same shift (high probability). Finally, in order to achieve agreement with the measured spectra, an isotropic (orientation independent) NMR linebroadening has to be taken into account. The latter is related to the special linewidth of ^{125}Te spectra as discussed in the following section.

As mentioned above, orientation dependent single crystal spectra allow the direct determination of the isotropic and the axial contributions to the NMR shift (cf.

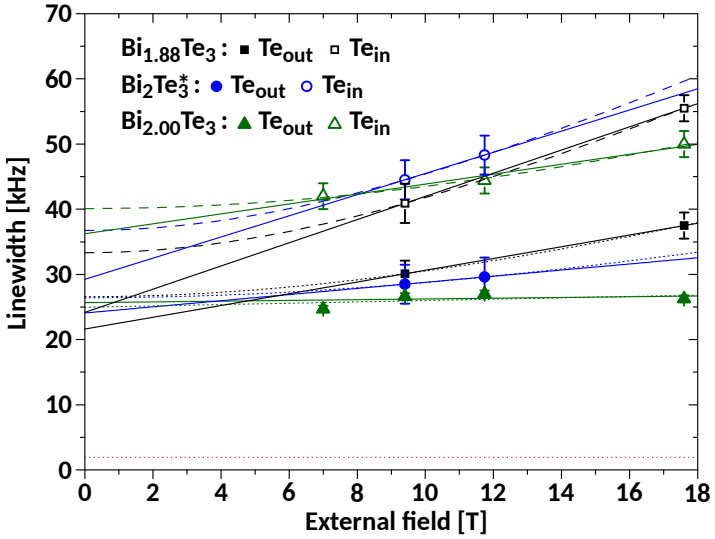

Figure 7.5 The ^{125}Te linewidths as function of the external field B_0 for all three samples and crystal sites. The linewidth is measured as full width at half maximum (FWHM). The individual field dependencies are fitted with a linear (solid lines) and a quadratic dependence (dashed lines) to determine field dependent and independent components (see text for details). The red dotted line represents expected contributions to the linewidth from direct dipole interactions. Each resonance shows a significant field independent (extrapolation to $B_0 = 0$) NMR linewidth which proves a very unusual dipole interaction similar to what is found in Bi_2Se_3 [23].

equations (7.1), (2.30), and (2.31)). The complete set of results for the three samples under investigation is provided in Tab.7.1. The findings are: the anisotropic NMR shift contributions, K_{axial}, of Te_{in} and Te_{out}, have a different sign and magnitude, their isotropic parts, K_{iso}, are nearly the same yielding an overlap of the resonance lines close to the magic angle. The NMR shift changes with the sample and must therefore be related to actual carrier concentration as argued by Boutin et al. [76].

7.1.4 Linewidths

Using ^{77}Se NMR in Bi_2Se_3 single crystals, Georgieva et al. [23] reported extensive NMR line broadening that was attributed to an exotic indirect internuclear dipole coupling of Bloembergen-Rowland type. The same calculations imply a similar effect for ^{125}Te nuclei in Bi_2Te_3 [74]. The NMR linewidths of Te_{in} and Te_{out} have therefore been measured at different magnetic fields in order to separate the field independent NMR linewidth that accounts for dipole interactions.

In Fig.7.5, the linewidths, i.e. the full width at half maximum (FWHM) of the resonances, of Te_{in} and Te_{out} for the three crystals under investigation are presented. In general, Te_{in} resonance lines were found to be measurably wider than outer ones,

qualitatively similar to Se in Bi_2Se_3. The field dependence of the linewidths as shown in Fig.7.5 reveals that in both cases, i.e. Te_{in} and Te_{out}, there is a considerable field independent NMR linewidth (extrapolation to $B_0 = 0$). The applied fitting formulas are the following. The straight solid lines in Fig.7.5 represent a convolution of two Lorentzian distributions and thus their linewidths add up as

$$\Lambda_{\mathrm{L}} = \Lambda_{0,\mathrm{L}} + b_{\mathrm{L}} B_0 \ ; \tag{7.2}$$

In a second model, the total linewidth results from the convolution of two Gaussian distributions and the total linewidth thus assumes

$$\Lambda_{\mathrm{G}} = \sqrt{\Lambda_{0,\mathrm{G}}^2 + (b_{\mathrm{G}} B_0)^2} \ . \tag{7.3}$$

It has to be noted that both representations are simplified approximations to the magnetic field dependence of the NMR linewidth as investigated in the present study. The results of the fittings were averaged and can be found in Tab.7.1.

The NMR line broadening originating from direct dipole interactions, (2.32) and (2.33), can be estimated with van Vleck's method of moments, (2.35) and (2.34) [84]. For Te_{in}, there are six Bi neighbours forming a octahedron. The line broadening from the heteronuclear dipole coupling with these 6 neighbours is about $\sim$1 kHz. In case of Te_{out}, there are only three Bi neighbours. The three Te neighbours from the adjacent quintuple layer contribute a vanishing broadening due to the low abundance (7 %) of ^{125}Te nuclei. Coupling partners further away will contribute much less to the line broadening due to the $\sim r^{-6}$ dependence in equation (2.35), which yields a $\sim r^{-3}$ dependence for the resulting linewidth. It can be concluded that the NMR line broadening of ^{125}Te nuclei in Bi_2Te_3 for $c \parallel B_0$ resulting from direct dipole coupling will hardly exceed 2 kHz.

7.1.5 Overview of ^{125}Te NMR properties in Bi_2Te_3

Table 7.1 NMR properties for the three samples studied: $K_{\mathrm{iso/axial}}$ denotes the isotropic and axial shift contribution, respectively. Λ_0 is the field independent linewidth, while b the field dependent component. $T_{2\mathrm{G}}$ is the characteristic time scale of the spin echo relaxation approximated by a Gaussian decay. n denotes the carrier concentration obtained from Hall effect measurements.

	$Bi_2Te_3^*$		$Bi_{2.00}Te_3$		$Bi_{1.88}Te_3$	
	Te_{out}	Te_{in}	Te_{out}	Te_{in}	Te_{out}	Te_{in}
K_{iso} [ppm]	437(8)	314(10)	398(10)	259(15)	375(10)	234(15)
K_{axial} [ppm]	-483(8)	938(9)	-390(20)	1075(70)	-311(20)	1147(45)
Λ_0 [kHz]	25(1)	33(4)	25(1)	38(2)	24(2)	29(4)
b [kHz/T]	0.8(3)	2.1(5)	0.30(15)	1.2(4)	1.2(3)	2.2(3)
b [ppm]	60(22)	156(37)	22(12)	89(30)	89(22)	164(19)
$T_{2\mathrm{G}}$ [μs]	120(20)	85(10)	110(10)	65(5)	110(10)	66(8)
n [cm^{-3}]			$1.7(1) \times 10^{19}$		$4.8(5) \times 10^{18}$	

7.2 Discussion

Single crystal NMR spectra of ^{125}Te in Bi_2Te_3 consist of two individual resonances corresponding to the two crystal sites, Te_{in} and Te_{out} (cf. Figs.1.1 and Fig.7.1). This assignment has already been reported [26]. It is based on the relative intensity of the two NMR signals after T_2 correction. The initial intensities must reflect the relative number of nuclei occupying different positions in the lattice. Thus, as there are twice as many Te_{out} sheets than Te_{in} sheets per quintuple layer, the relative intensity of the corresponding resonances must be 2 : 1. That this is indeed the case was shown in Fig.7.2 for $Bi_2Te_3^*$ and $Bi_{1.88}Te_3$. Furthermore, these results emphasise the similarities of Bi_2Te_3 and Bi_2Se_3 as for the latter, two ^{77}Se signals were also identified [23].

NMR shift

The assignment allows a site selective evaluation of ^{125}Te NMR in Bi_2Te_3. Orientation dependent measurements as shown in Fig.7.3 and Fig.7.4 reveal an axially symmetric NMR shift for both lines, Te_{in} and Te_{out}. The shift components, i.e. K_{iso} and K_{axial}, as determined by the measurements are provided in Tab.7.1, seem

to change systematically with the samples. Although the carrier concentration is only known for $Bi_{1.88}Te_3$ and $Bi_{2.00}Te_3$ from Hall effect measurements, the NMR shift suggests an ordering of the samples as provided in the table, with the carrier concentration, n, decreasing from left to right. In this scenario, $Bi_2Te_3^*$ would have the highest carrier concentration, n.

An NMR shift that changes with the carrier concentration is consistent with the general expectation of a Knight shift contribution in systems with a substantial number of free carriers. The isotropic shift, K_{iso}, of $\mathrm{Te_{out}}$ and $\mathrm{Te_{in}}$ increases with the carrier density, n. The axial parts, K_{axial}, of $\mathrm{Te_{in}}$ and $\mathrm{Te_{out}}$ have opposite sign. Their change, however, occurs in the same direction with changing n i.e., for both resonances, K_{axial} decreases with increasing n. In summary, the carrier dependent isotropic NMR shift of ^{125}Te in Bi_2Te_3 is consistently positive, whereas the carrier dependent axial component is negative.

Only the positive dependence of the isotropic NMR shift of $\mathrm{Te_{out}}$ with increasing concentration of electrons is in agreement with the calculations carried out by Boutin et al. [76]. However, the present study provides only a very limited set of data. Especially a reliable determination of the actual carrier concentration of the sample under investigation is not easily achieved. Furthermore, Boutin et al. [76] do not include the carrier independent shifts, which are inevitably included in the present measurements. It must be concluded that the NMR shift of ^{125}Te in Bi_2Te_3 is quite complex and the various carrier dependent shift contributions,[2] as proposed by Boutin et al. [76] are in a different balance in the real systems. A systematic experimental study of samples with a variety of well defined carrier concentrations will help to deepen the understanding of NMR shifts in this class of materials.

The individual shift anisotropies are in agreement with averaged powder spectra. As seen in Figs.7.3 and 7.4, the two signals overlap near the magic angle. In the corresponding powder, the two resonance lines overlap entirely, as illustrated by the bottom spectra in Fig.7.4. This is a very important observation, because there are publications that deal with the NMR of Bi_2Te_3 powders without mentioning a second NMR signal at all. Antonenko et al. [27] worked out the individual shift anisotropies using powdered samples only. Apparently, a detailed angular dependence of the single crystal was not available. They correctly concluded on an overlap of the two signals and presented two different scenarios for the two shift anisotropies. However, were not able to decide for one scenario or the other. In this regard, the present

[2]There is the contact interaction, dipolar and orbital shift, as well as core polarisation contributing to the total NMR shift.

study provides a clarification for the case of n-type Bi_2Te_3.

On the basis of the full set of information, as presented in Tab.7.1, one may draw the following conclusion concerning the NMR of Bi_2Te_3 powders: given the smaller intensity of Te_{in}, its faster spin-echo decay (T_2) and much larger shift anisotropy, the powder spectrum of Bi_2Te_3 should be dominated by Te_{out}, such that the conclusions reported in some publications are only marginally affected.

Linewidths

The NMR linewidths of the two resonances in each sample have been evaluated at different external fields in order to extract field independent linewidth components that evidence dipole couplings among nuclei. Field independent linewidths are indeed found to be very large, exceeding the linewidths originating from direct dipole coupling by an order of magnitude. Note that the measurements were carried out for $c \parallel B_0$. Thus, due to the coordination of the three (Te_{out}) or six (Te_{in}) Bi neighbours (cf. Fig.7.1) at angles between 50° and 60°, direct dipole interaction is highly suppressed because of the $(3\cos^2(\theta) - 1)$ term in (2.34) which nears zero for these angles. NMR line broadening from direct dipole interactions were estimated to be less than 2 kHz.

When considering the orientation dependent measurements in Figs.7.3 and 7.4, one notices that the linewidth does not change with β. The linewidth, therefore, represents an isotropic or scalar interaction which is typical for indirect dipole interactions. Together, these findings of a field (dipole) and orientation (isotropic) independent broadening that is much larger than direct dipole couplings, provide clear evidence of an unusual strong indirect internuclear dipole interaction affecting ^{125}Te resonances. Furthermore, when comparing different samples, the linewidth of the outer signal, $\Lambda_{0,out}$, does not change significantly, in contrast to the linewidth of the inner signal, $\Lambda_{0,in}$. Thus, it is not clear whether the field independent linewidth depends on the carrier concentration.

With a similar observation of extensive, field and carrier independent NMR line broadening of the ^{77}Se NMR in Bi_2Se_3, Georgieva et al. [23] argued that a surprisingly slowly decaying Bloembergen-Rowland (BR) interaction governs the indirect dipole coupling among nuclear moments. In the present study, it is not possible to confirm a Bloembergen-Rowland mechanism as the source for internuclear coupling as proposed by the same theoretical model used for the ^{77}Se NMR in Bi_2Se_3 [74]. The experimental results are not sufficient, neither in respect to the variation of carrier concentration across the samples nor in the accuracy of the field dependencies

of the NMR linewidths. A BR coupling would be almost independent of the carrier concentration and the corresponding NMR linewidth should therefore be independent as well.

Besides the large field independent linewidths that are due to an indirect dipole coupling, field *dependent* line broadening can be observed in all three samples. It is smallest in $Bi_{2.00}Te_3$, and obviously more pronounced for Te_{in} resonances with values up to about 2.2 kHz/T (165 ppm). The magnetic field dependent broadening in a single crystal must stem from a variation of the NMR shift. The systematically stronger broadening of Te_{in} resonances provides some evidence, as it reflects a distribution of the very large axial shift component. Such a conclusion could imply a variation of the carrier concentration within the sample. Similarly, the line broadening may reflect defects as argued by Levin et al. [25].[3] In any case, such an NMR line broadening could directly be related to the inhomogeneities reported in chapter 6. This is a very interesting observation as it illustrates a tool that could be used to investigate the homogeneity of a given sample. A more systematic study may reveal variations as a consequence of the defect density and accompanied changes in the band structure due to localised charges.

Transverse relaxation

The spin-echo decay of ^{125}Te nuclei in Bi_2Te_3 has not been reported so far. In the present work, the spin-echo decay was determined in all three samples for both Te signals. The relaxation was found to be very fast with maximum values ranging between 65 μs and 120 μs. The decay is different for the two crystal sites, the inner signal decays faster (cf. Tab.7.1). There are also slight variations across the samples.

Again, the results are very similar to what was found for ^{77}Se NMR in Bi_2Se_3. There, the spin-echo decay is very fast as well, while the inner signal, Se_{in}, decays faster (between 95 and 134 μs) than the than Se_{out} (between 215 and 260 μs). The transverse relaxation was attributed to a very fast spin-lattice relaxation of the quadrupolar split ^{209}Bi nuclei (less the 1 ms, cf. Ch.8). The coupling of the ^{77}Se nuclei to the ^{209}Bi nuclei (100 % abundance) is established through the indirect dipole interaction mentioned above. In the present study, no relaxation measurements of ^{209}Bi in Bi_2Te_3 are available. In a future study which includes the ^{209}Bi NMR of Bi_2Te_3, the surprisingly short ^{125}Te spin-echo decay, and whether it is connected to the Bi T_1, should be investigated in greater detail.

[3] Note, Levin et al. [25] found a "shoulder", i.e. an additional signal, they do not mention NMR line broadening.

7.3 Summary

In summary, the ^{125}Te NMR of Bi_2Te_3 single crystals and powders was investigated. There are two Te resonance lines that can be assigned to nuclei occupying either the inner (Te_{in}) or the outer (Te_{out}) Te sheets of a quintuple layer. Most remarkably, Te resonances show a field independent and isotropic, i.e. orientation independent, NMR line broadening that evidences a strong indirect internuclear coupling. The result is very similar to what was found for ^{77}Se NMR in Bi_2Se_3 [23]. Furthermore, the model calculations that associate the indirect coupling in Bi_2Se_3 with a slowly decaying Bloembergen-Rowland (BR) susceptibility, also hold for Bi_2Te_3 [74]. The current study, however, cannot exclude an RKKY interaction due to a lack of samples with sufficiently different carrier concentrations. This question is certainly worth being addressed in future projects.

The NMR shift of Te_{in} and Te_{out} was evaluated by tracing the single crystal spectra under stepwise crystal rotation. In both cases, the shift is axially symmetric in agreement with the symmetry of the crystal structure. The isotropic shift of Te_{in} and Te_{out} are very similar, while the axial shifts differ in size and sign. As a consequence, the single crystal spectra overlap near the magic angle. Furthermore, these shift anisotropies cause the two signals to overlap completely in a powder. However, the contribution of Te_{in} to a powder spectrum is very limited due to its reduced intensity, its larger axial shift, and shorter T_2. Hence, though the lines do overlap in powders of Bi_2Te_3, the Te_{in} signal is too weak to affect the conclusions drawn by some authors in the literature.

Systematic changes of the NMR shift observed across the samples must stem from sample dependent carrier concentrations. Variations of the carrier concentration within a single sample could then explain the observed NMR line broadening which is proportional to the external magnetic field, i.e. a broadening that arises from a distribution of the carrier dependent shift. In the future, NMR shift and linewidth together can potentially be developed into a powerful tool to probe the doping level and homogeneity of Bi_2Te_3 single crystals.

Chapter 8

NMR of quadrupole nuclei: ^{209}Bi in Bi_2Se_3

This chapter reports a comprehensive study of ^{209}Bi NMR in Bi_2Se_3. The focus is laid on macroscopic single crystalline samples with different carrier concentrations, n, as introduced in Ch.5. The chip-like single crystals of a few millimetres in length and width, and up to ∼1 mm in thickness were placed in single axis goniometers. The rf-coils were wound directly around the samples to achieve filling factors close to 1. The coil's symmetry axis, and thus the direction of the alternating field, B_1, was kept perpendicular to the external field, B_0, *and* to the crystal c-axis. For comparison, Bi_2Se_3 powders obtained from grinding commercial Bi_2Se_3 flakes (*Sigma Aldrich*) using a mortar and pestle were investigated. These powders were filled in cylindrical glass containers with the rf-coil wound around the container.

Solid-echo (SE) pulse sequences with short and strong rf-pulses were employed to excite the whole ^{209}Bi quadrupole spectrum. Typical quality factors of $Q \sim 20$ provided sufficient bandwidth for excitation and detection. Hahn-echo (HE) measurements were used to selectively access single transitions of quadrupole split spectra. The latter were also used to determine transition selective nutation frequencies, $\tilde{\omega}_{\mathrm{rf}}$, spin-echo decay times, T_2, and the spin-lattice relaxation time, T_1. Where applicable, free induction decay (FID) experiments were used.

All measurements were carried out at room temperature. Magnetic fields from 7.05 T to 17.6 T were used, while most of the experiments were conducted at 9.39 T and 11.74 T with typical ^{209}Bi resonance frequencies of ∼64.7 MHz and ∼80.8 MHz, respectively. The secondary reference method (Ch.5) was used for referencing NMR shifts.

The chapter is divided into two parts. The first part presents a comprehensive account of experimental results, beginning with experiments with $c \parallel B_0$, i.e. the

crystal c-axis parallel to the external field B_0, followed by measurements at the magic angle ($\angle(c, B_0) \approx 55°$), and by a full orientation dependence of the ^{209}Bi spectrum from $c \parallel B_0$ to $c \perp B_0$, including the comparison of samples with different carrier concentrations, n. The NMR of Bi_2Se_3 powders is presented next. The second part provides a discussion of the general NMR properties, presents evidence that ^{209}Bi quadrupole splitting measures the energy band inversion, and describes how the unusual orientation independent electric quadrupole interactions can be explained with a strong spin-orbit coupling of conduction electrons in Bi_2Se_3.

8.1 Experimental results

In sections Sec.8.1.1 to 8.1.3, the experimental outcome obtained from a single crystal that was provided by an overseas laboratory as mentioned in Ch.5 is reported.[1] ^{77}Se NMR (including some ^{209}Bi NMR) of the same single crystal were reported in Georgieva et al. [23]. Details of the synthesis can be found there as well. Most of the results in this chapter are published in Guehne et al. [104].

With Sec.8.1.4, single crystals made in the course of this project are included. The sample labelling is as follows: the single crystal from Japan is identified as "$Bi_2Se_3^{**}$", while the samples, for which the syntheses are described in Ch.5, are labelled with the respective composition of the melt they were grown from, i.e. "$Bi_{1.95}Se_3$", "$Bi_{2.00}Se_3$", and "$Bi_{2.05}Se_3$". The increased Bi content of the melt is accompanied by an increase of the corresponding carrier concentration, n, of the resulting crystals as measured by Hall effect.

8.1.1 The $c \parallel B_0$ orientation

First order quadrupole interaction

^{209}Bi is a spin 9/2 system. As reported in the literature, ^{209}Bi nuclei in Bi_2Se_3 are subject to a moderate quadrupole interaction (cf. Sec.2.3.2). The c-axis defines the stacking direction of this layered material (Fig.1.1). It is found that this direction also defines the principle axes system (PAS) of the electric field gradient (EFG), that is, the principle component of the EFG, V_{ZZ}, at the bismuth site is aligned along the crystal c-axis [16, 18, 20, 21]. Thus, the splitting for $c \parallel B_0$ defines the quadrupole splitting frequency, $\omega_Q/2\pi \equiv \nu_Q$ (2.39). The literature reports values $\nu_Q \sim 150\,\text{kHz}$, which is very small, such that a first order treatment as given by (2.38) is a very good approximation.

[1] Prof. K. Kadowaki, Division of Materials Science, Tsukuba, Japan.

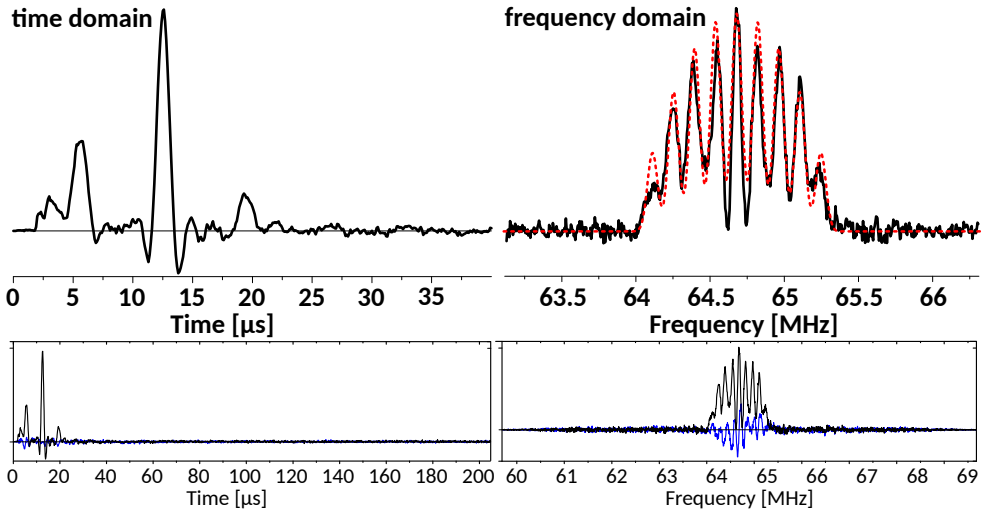

Figure 8.1 High power solid echo measurement of $Bi_2Se_3^{**}$ with $\pi/2$ width of 0.75 μs and $\tau_\Delta = 15.5\,\mu$s obtained at $B_0 = 9.4\,$T. The echo, as it appears in the time domain is given on the left and its Fourier transform on the right including a first order quadrupole fit (red dashed line). The quadrupole splitting is found to be $\nu_Q = 141(3)\,$kHz, while quadrupole broadening is $< 5\,\%$. The two bottom panels provide the complete domains that are determined by the dwell time = 100 ns (time resolution of the signal digitisation) which determines the frequency domain of 10 MHz. The number of data points used was 2048, setting the acquisition window to $2048 \cdot 100\,\text{ns} = 204.8\,\mu$s.

Solid echoes ($\pi/2 - \tau_\Delta - \pi/2$) of short, high-power pulses ($< 1\,\mu$s) were employed to excite the whole first order quadrupole pattern. In Fig.8.1, the signal in the time domain and it's Fourier transform is presented. Note, that the whole signal in the left panel of Fig.8.1 represents the echo. Its centre is given by the highest amplitude located at $\approx$12.5 μs. Its rather small total width of about 10 to 15μs translates into the broad individual resonances (65 to 75 kHz) that form the quadrupole pattern in frequency space. The structuring of the echo, especially the two features at $\sim$5 μs, and $\sim$19 μs, give rise to the typical equidistant quadrupole splitting as seen in the frequency domain.

The first order quadrupole spectrum was fit with a set of nine equidistant Gaussian lines with relative intensities following equation (2.43) (red dashed line in Fig.8.1). The quadrupole splitting was determined to be $\nu_Q = 141(3)\,$kHz, which is slightly smaller than the values reported in the literature, a first indication of its sample dependence. Despite the high carrier concentration from native defects, there is almost no quadrupole broadening, i.e. from a distribution of splitting frequencies, $\Delta\nu_Q$. Such a broadening would affect the individually resonances differently. While there would be no broadening of the central transition, the satellites would

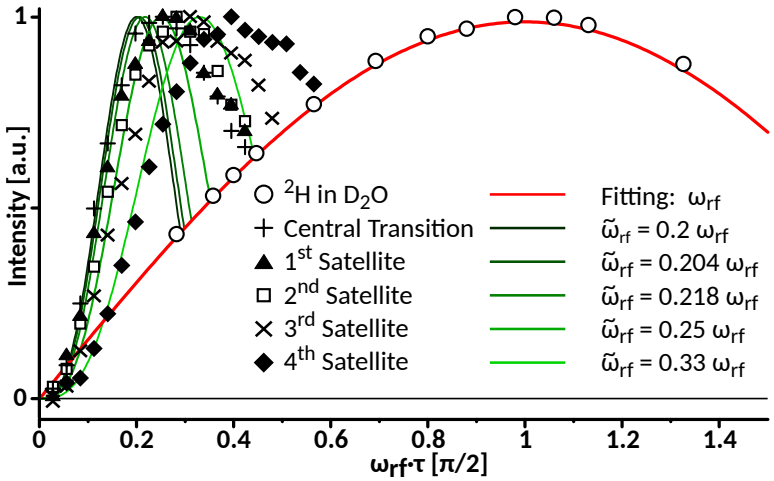

Figure 8.2 Nutation spectroscopy using selective Hahn-echoes with $\pi/2$-pulse length of 10 μs, obtained in $Bi_2Se_3^{**}$ for individual peaks (central transition and lower satellites – all symbols except for open circles) of the spectrum shown in Fig.8.1. Simulations of transition selective nutations following equation (2.41) (green solid lines) are included. As a non-selective or spin 1/2 reference, ^{2}H in D_2O was measured (open circles). The red solid line represents the fitting using a sine function. Intensities were normalised for the sake of clarity.

be affected gradually by their order with the largest width for the fourth satellites. Uncertainties of ν_Q were thus estimated to be smaller than 5 %. This is indeed a surprising result as due to the inevitable chemical irregularities from native defects, one would not have expected such a well defined Bismuth environment (100 % abundant isotope) when averaging over a macroscopic single crystal.

Nutation spectroscopy

For each transition of the first order quadrupole spectrum shown in Fig.8.1, Hahn-echo (HE) nutation experiments were carried out. Selective pulses of 10 ($\pi/2$-pulse) and 20 μs (π-pulse) duration were used to limit the excitation to individual transitions, while the nutation was conducted by progressively increasing the pulse power levels, P. ^{2}H in D_2O was used as a non-selective reference, measured in the same rf-coil and being rescaled using (4.10) and (4.11).[2] The signal intensities as functions of the non-selective nutation angle, $\omega_{\rm rf}\tau$, are given in Fig.8.2. The nutation angle is a convenient expression to identify a quadrupole split system. In case of $I = 9/2$, as for ^{209}Bi, the enhancement of the nutation frequency, $\tilde{\omega}_{\rm rf}$, for each transition is given by (2.41) and in Tab.2.1.

[2]Note, a quadrupole coupling of ^{2}H ($I = 1$) in D_2O is cancelled out due to the rapid reorientation of the water molecules.

Bismuth transitions were measured with a HE sequence that follow a $\sin^3(\sqrt{P})$ relation (cf. appendix 8.3) due to phase cycling. Deuterium in D_2O, in contrast, was measured using single pulse FIDs and the corresponding nutation assumes the typical $\sin(\sqrt{P})$ dependence of signal intensity. This explains the different functions displayed in Fig.8.2. The power level where the D_2O signal assumes its first maximum corresponds to $\tau_{\pi/2}$ via (4.10) and (4.11). This was used to convert the whole set of selective ^{209}Bi nutations into the nutation angle by

$$\frac{\pi\tau}{2\tau_{\pi/2}} \equiv \omega_{\mathrm{rf}}\tau \ . \tag{8.1}$$

The results as given in Fig.8.2 prove a quadrupole interaction affecting the ^{209}Bi nuclei. Owing to the large spin of $I = 9/2$ of ^{209}Bi, the differences between selective and non-selective excitation are as large as a factor of 5 for the central transition. Even the subtle differences between the individual transitions (green simulations in Fig.8.2) perfectly follow the theory for moderate power levels (cf. Tab.2.1). This is an important result because it shows that individual transitions can be accessed separately, despite their rather large widths of 70 kHz.

Deviation from the simulation for higher power levels is not surprising, when magnetic field inhomogeneities of the rf-coil and the excitation of forbidden transitions (located between the satellites, cf. [105]) are taken into account. Intensities were normalised for clarity. The typical intensity pattern of a selectively excited quadrupole spectrum, given by equation (2.44), is not exactly recovered due to large variations of the spin echo decay of individual transitions.

Spin echo decay

With the optimised excitation conditions from the nutation experiments, the spin echo decay ($10\,\mu\mathrm{s} - \tau_\Delta - 20\,\mu\mathrm{s}$) for each transition was measured. The results are presented in Fig.8.3. The echoes decay in good approximation exponentially, cf. Fig.8.3(a). In the lower panel of Fig.8.3(b) the results form exponential fits of the individual spin echo intensities are presented. The change in relaxation time from the inner parts of the spectrum to the outer satellites is intriguing. The central transition vanishes on average about six times faster than the 4th satellites.

The total spectral intensity of the signal obtained from the solid echo sequence from Fig.8.1 was also investigated as a function of the pulse separation τ_Δ, as shown in Fig.8.3(a) by the blue data points. This solid echo decay occurs on the same timescale (on average about $\sim 35\,\mu\mathrm{s}$) as the transition selective echo decay, with a slight change in slope for larger τ_Δ. Thus, the solid echo decay represents in good

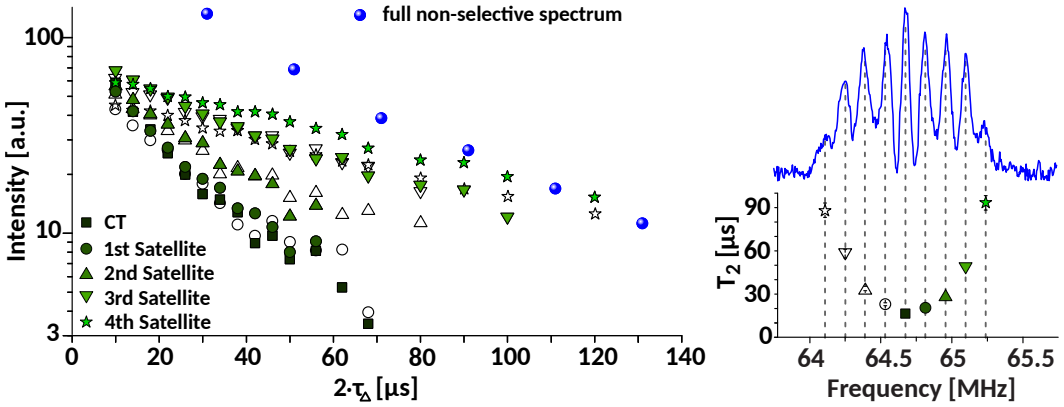

Figure 8.3 (a) Selective spin echo decay observed in $Bi_2Se_3^{**}$ (open and green symbols, for assignment see panel b). The blue data points represent the full spectral intensity of the non-selective solid echoes shown in Fig.8.4. (b) Non-selective solid echo spectrum (blue) and the T_2 values obtained from single exponential fits of the spin echo decays are shown in (a) for each transition.

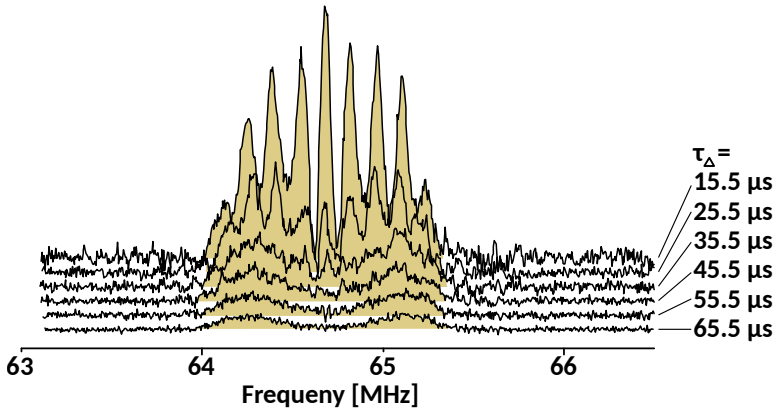

Figure 8.4 Fourier transform of non-selective solid echo experiments ($\pi/2 = 0.75\,\mu s$) with increasing pulse separation, τ_Δ (solid echo decay), of $Bi_2Se_3^{**}$. The spectra are normalised by the number of scans. Thus, the intensities are representative and the reduced noise for the lower spectra stems from a greatly enhanced signal averaging.

approximation the average of the individual relaxation processes with contributions from each transition following the non-selective intensity pattern (2.43).

In Fig.8.4 the solid echo decay and its effect on the overall lineshape of the quadrupole pattern is presented. Most remarkable is the signal loss in the central region, but in general, individual spectral features disappear rather rapidly leaving the typical double-hump spectrum that is known from literature [16, 20]. As pointed out by [16], these observations must reflect an unusual spin echo relaxation in the present material.

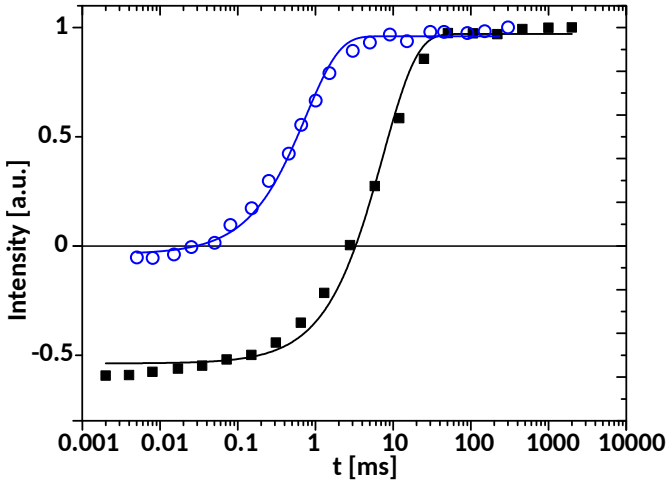

Figure 8.5 Signal recovery of ^{209}Bi as obtained from selective saturation of the central transition for $c \parallel B_0$ (blue data points) and from non-selective inversion at the magic angle (black data points) in $Bi_2Se_3^{**}$. Single exponential recovery, $M(t) = M_0(1 - f \cdot \exp(t/T_1))$, was used to evaluate the corresponding effective spin-lattice relaxation, resulting in an apparent $T_1 \sim 750\,\mu$s for the selectively excited CT for $c \parallel B_0$ and $T_1 \sim 7.5$ ms for the non-selectively excited spectrum at the magic angle.

Spin-lattice relaxation

Spin-lattice relaxation was measured selectively of the central transition, using a saturation recovery pulse sequence (data points in Fig.8.5). The recovery of the spin system is very fast, about 0.75(5) ms, when the central transition is excited individually.

Key results: ^{209}Bi NMR for $c \parallel B_0$

- A well defined first order quadrupole interaction ($\nu_Q = 141(3)$ kHz, Fig.8.1) is confirmed by nutation spectroscopy (Fig.8.2).
- A very short and transition dependent spin echo decay (Fig.8.3) is found that leads to severe changes of the lineshape as function of the relaxation (Fig.8.4)
- A very short selective spin-lattice relaxation with an apparent $T_1 = 0.75(5)$ ms was found for the central transition.

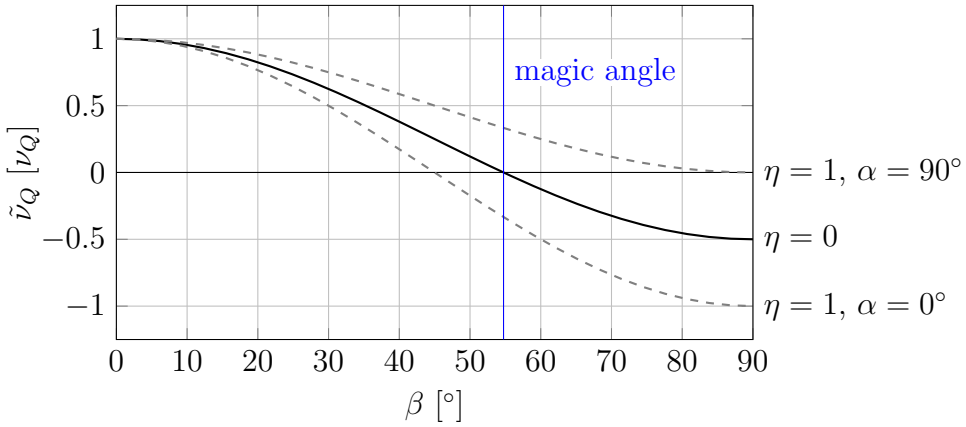

Figure 8.6 The quadrupole splitting (8.2) of an axially symmetric EFG ($\eta = 0$) as a function of β (black solid line). Also given are the two limits of a highly asymmetric EFG ($\eta = 1$) for the angles $\alpha = 0°$ and $90°$ (dashed lines). Note, any possible orientation dependent splitting with $0 \leq \eta \leq 1$ for any orientation α will be found between the two dashed lines.

8.1.2 The magic angle

From equation (2.40) in Sec.2.3, one can see that the effective splitting that is measured in a single crystal depends on the orientation of the EFG with respect to B_0. This angular dependent splitting reads

$$\tilde{\nu}_{\mathrm{Q}}(\beta, \eta, \alpha) = \nu_{\mathrm{Q}} \left\{ \frac{3\cos^2\beta - 1}{2} + \frac{\eta}{2}\sin^2\beta\cos 2\alpha \right\} . \tag{8.2}$$

From the crystal structure's cylindrical symmetry one concludes that $\eta = 0$, i.e. that the EFG is axially symmetric ($V_{YY} = V_{XX}$). Thus, the angular part in (8.2) reduces to $(3\cos^2\beta - 1)/2$. The function is drawn in Fig.8.6. At $\beta = \arccos\sqrt{1/3} \approx 54.74°$, the function has an x-intercept, which means that by definition the quadrupole interaction disappears. This angle is called the *magic angle*, well-known in the context of magic angle spinning.

The absence of a quadrupole interaction means that the excitation conditions change from selective to non-selective, because it is not possible any more to induce a single transition without inducing transitions in the other spin states. In the frequency domain, the broad quadrupole pattern collapses to a single line. The single resonance line can be accessed with single pulse FID measurements. Thus, FID nutation experiments were carried out (Fig.8.7(a)) very similar to those done on ^{2}H in D_2O as shown in Fig.8.2.

The nutation perfectly recovers the non-selective excitation condition represented

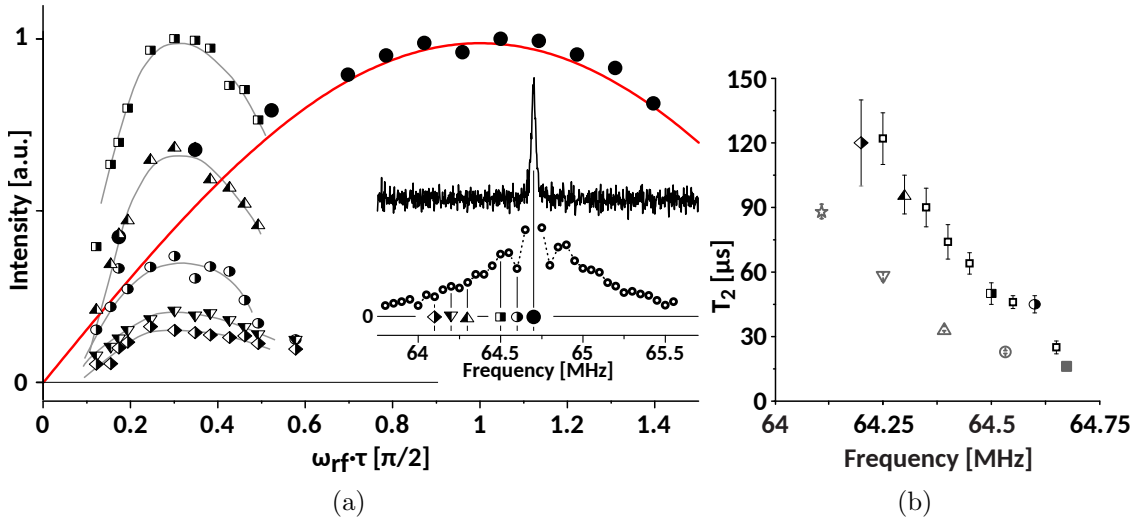

(a) (b)

Figure 8.7 (a) Nutation spectroscopy of single crystal $Bi_2Se_3^{**}$ at the magic angle. The solid circles denote a normalised FID (upper spectrum of the inset) nutation, perfectly reproducing the non-selective nutation of rescaled ^{2}H in D_2O (red solid line is the fitting from Fig.8.2) The half-filled symbols represent selective Hahn echo nutations ($\tau_{\pi/2} = 10\,\mu$s) at the magic angle between 100 and 600 kHz off centre. Relative intensities of the selective Hahn echoes are as measured (normalised to the maximum value of the nutation at -100 kHz). The grey solid lines are guide for the eye. The inset provides the combined and T_2-corrected frequency swept Hahn echo spectrum including symbol assignment.(b) T_2 values for selective Hahn echo decays obtained from simple exponentials of the broad spectrum at the magic angle. Symbols are the same as used in the nutations on the left. For comparison, the T_2 values obtained for $c \parallel B_0$ shown in Fig.8.3(b) are given in grey.

by the rescaled ^{2}H nutation in Fig.8.2 (red solid line). Consequently, T_1 measurements will give the system's actual spin-lattice relaxation. The result of the inversion recovery measurement carried out on $Bi_2Se_3^{**}$ at the magic angle is given in Fig.8.5 with $T_1 = 7.5$ ms from a single exponential fit. This is expected and in agreement with the much smaller effective $T_1 = 0.75$ ms as measured for the selectively excited CT with $c \parallel B_0$ [91]. [3]

A second signal

So far, the ^{209}Bi NMR gives a consistent picture in terms of its quadrupole splitting and T_1. However, as shown in the inset of Fig.8.7(a), there is considerable signal found far away from the centre of the spectrum, up to ± 600 kHz, that cannot be explained with equation (8.2). Frequency stepped Hahn echo nutation (Fig.8.7(a))

[3] The relation between selective and non-selective excitation and the corresponding apparent spin lattice relaxation times can be found in Suter et al. [91].

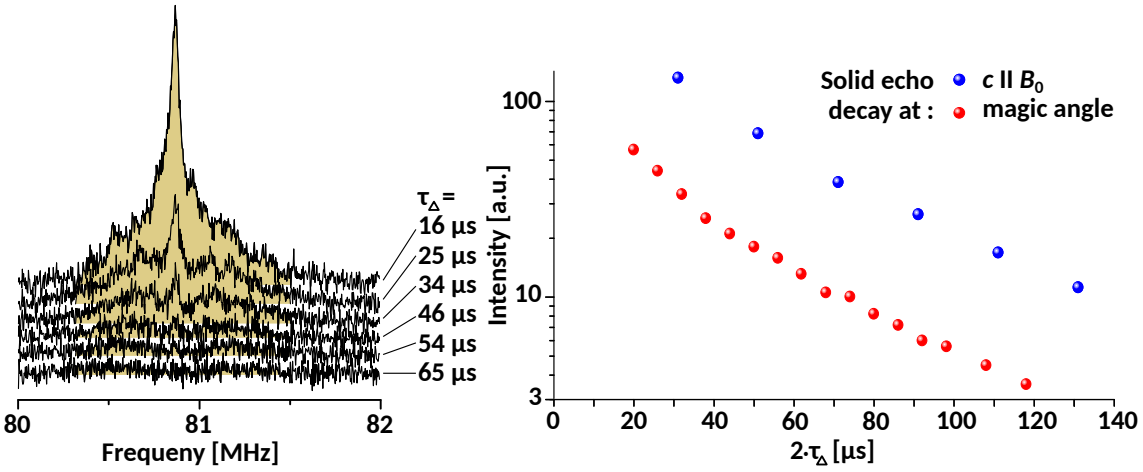

(a) (b)

Figure 8.8 (a) Non-selective solid echo spectra ($\tau_{\pi/2} = 1\,\mu$s) of the single crystal $Bi_2Se_3^{**}$ at the magic angle for increasing τ_Δ (solid echo decay). (b) Comparison of the solid echo decays in terms of the full spectral intensity as obtained for $c \parallel B_0$ (blue) and at the magic angle (red).

and T_2 measurements (Fig.8.7(b)) were used to investigate this off-centre region at the magic angle. Evidently, these resonances show selective excitation and must therefore be subject to quadrupole interaction. Additionally, an increase of the transverse relaxation time, T_2, from the centre to the outer parts is observed, similar to what is found with $c \parallel B_0$ (Fig.8.7(b)).

Non-selective solid echo experiments were applied to study the whole spectrum at the magic angle (Fig.8.8(a)). A very broad resonance line is observed which covers the same range of frequencies as the quadrupole split spectrum for $c \parallel B_0$. Furthermore, for increasing τ_Δ, a similar decay with a rather rapid vanishing inner region and a more slowly relaxing outer region is observed. The change of the total signal intensity occurs on the same timescale as the solid echo decay for $c \parallel B_0$, cf. Fig.8.8(b). These results constitute an astonishing irregularity of the first order quadrupole interaction found for ^{209}Bi in Bi_2Se_3.

Key results: ^{209}Bi NMR at the magic angle

- A single, non-selective resonance (Fig.8.7(a)) with $T_1 = 7.5(5)$ ms (Fig.8.5) is found in agreement with the well defined quadrupole splitting at $c \parallel B_0$ (8.2).
- A far extending distribution of resonances with selective excitation (Fig.8.7(a)) and distributed spin-echo decay (Fig.8.7(b)) is also found. This is in clear contradiction with the first order quadrupole interaction expressed by (8.2).

8.1.3 Orientation dependence

The single crystal was rotated about an axis perpendicular to B_0 *and* the crystal c-axis in 10° steps, i.e. β was changed from 0° to 90°. For each orientation, a solid echo measurement with $\pi/2$-pulse (0.75 μs was carried out. The complete set of orientation dependent spectra is given in Fig.8.9 together with a simulation following equation (8.2) with $\eta = 0$.

The orientation dependent measurements confirm what was already suggested by the measurements at the magic angle. The spectra change only slightly when leaving the $c \parallel B_0$ orientation. The total extension of spectral density, i.e. the range of about ±600 kHz that the total spectrum spans for $c \parallel B_0$, does not change during the rotation of the single crystal. Furthermore, it seems that the individual transitions seen for $c \parallel B_0$ (individual peaks) can be found for each orientation at the same frequencies (blue dashed lines in Fig.8.9). The result is very different compared to what one expects from a first order quadrupole interaction in a single crystal. The latter is represented by the simulated spectra on the left in Fig.8.9. An interesting detail is the narrow resonance visible in the centre of each spectrum for angles between 20° and 90°, which is accounted for in the simulation except for angles very close to the magic angle ($\sim 55°$).

Symmetric EFG tensor

In regard to the results, one may question whether the assumption of $\eta = 0$ is justified, even though there is no structural evidence for such a scenario. To verify this assumption, an additional orientation dependent measurement was carried out. Inside the rf-coil, the single crystal was rotated about the crystal c-axis by 45° and 90°. For each angle, the spectrum was measured again at $\beta = 0°$, 45°, and 90°. In total, this is related to orientation dependent measurements for three different angles α in equation (8.2). The results are shown in Fig.8.10(a) in the upper panel.

For $\eta \neq 0$, there would be very different effective splittings when leaving $c \parallel B_0$ (cf. Fig.8.6), which is clearly not the case. The spectra for different α at the same orientation β are very similar, apart from minor variations as the crystal had to be replaced inside the rf-coil. This means, the unusual orientation dependence as shown in Fig.8.9 is not related to the asymmetry parameter.

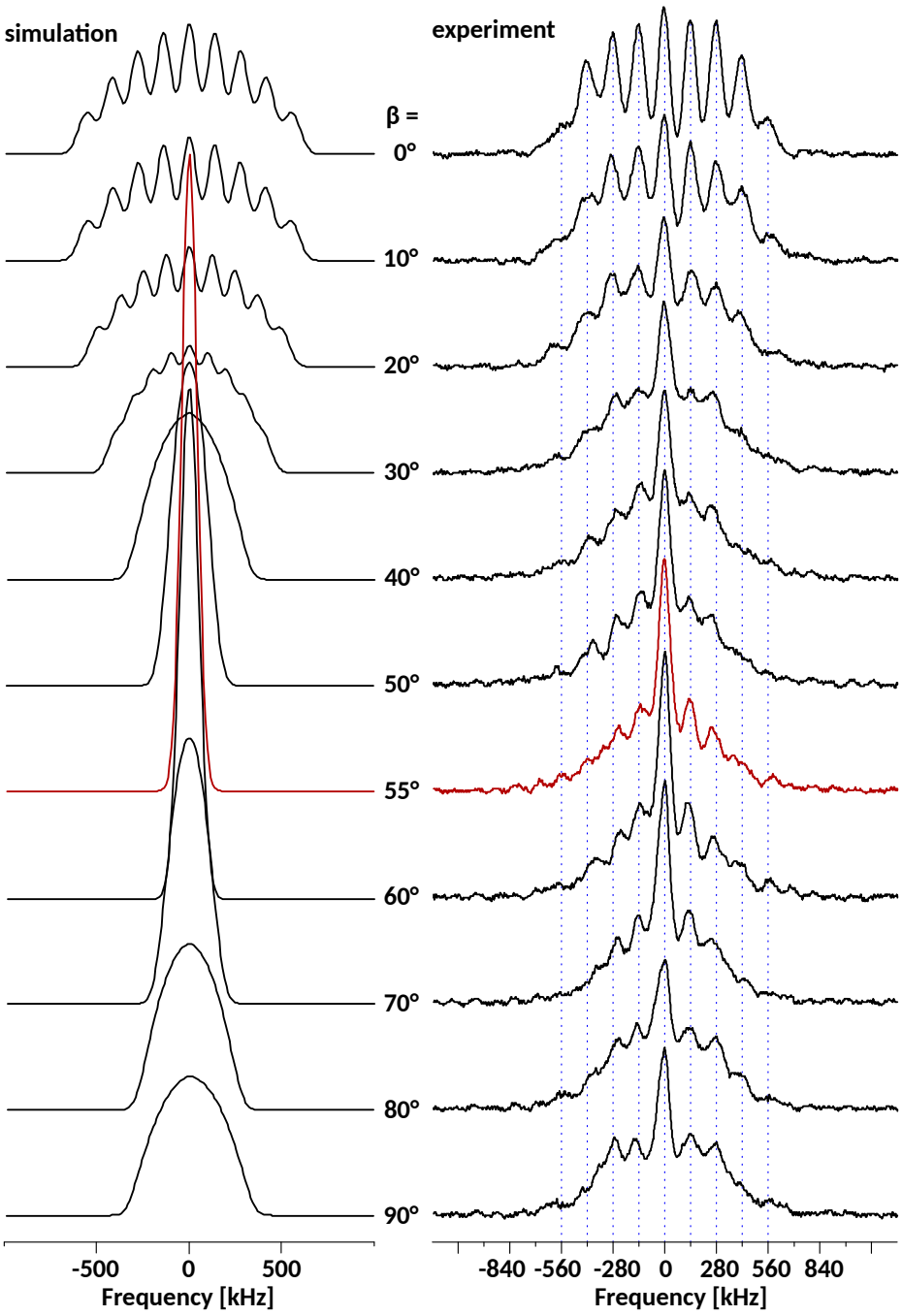

Figure 8.9 Orientation dependent non-selective ^{209}Bi spectra as (*left*) simulated from the quadrupole fitting for $c \parallel B_0$ (Fig.8.1) and (right) as obtained from non-selective solid echoes on $Bi_2Se_3^{**}$ under crystal rotation about an axis perpendicular to the crystal c-axis. The *red* spectra denote the magic angle spectra close to $\beta \sim 55°$.

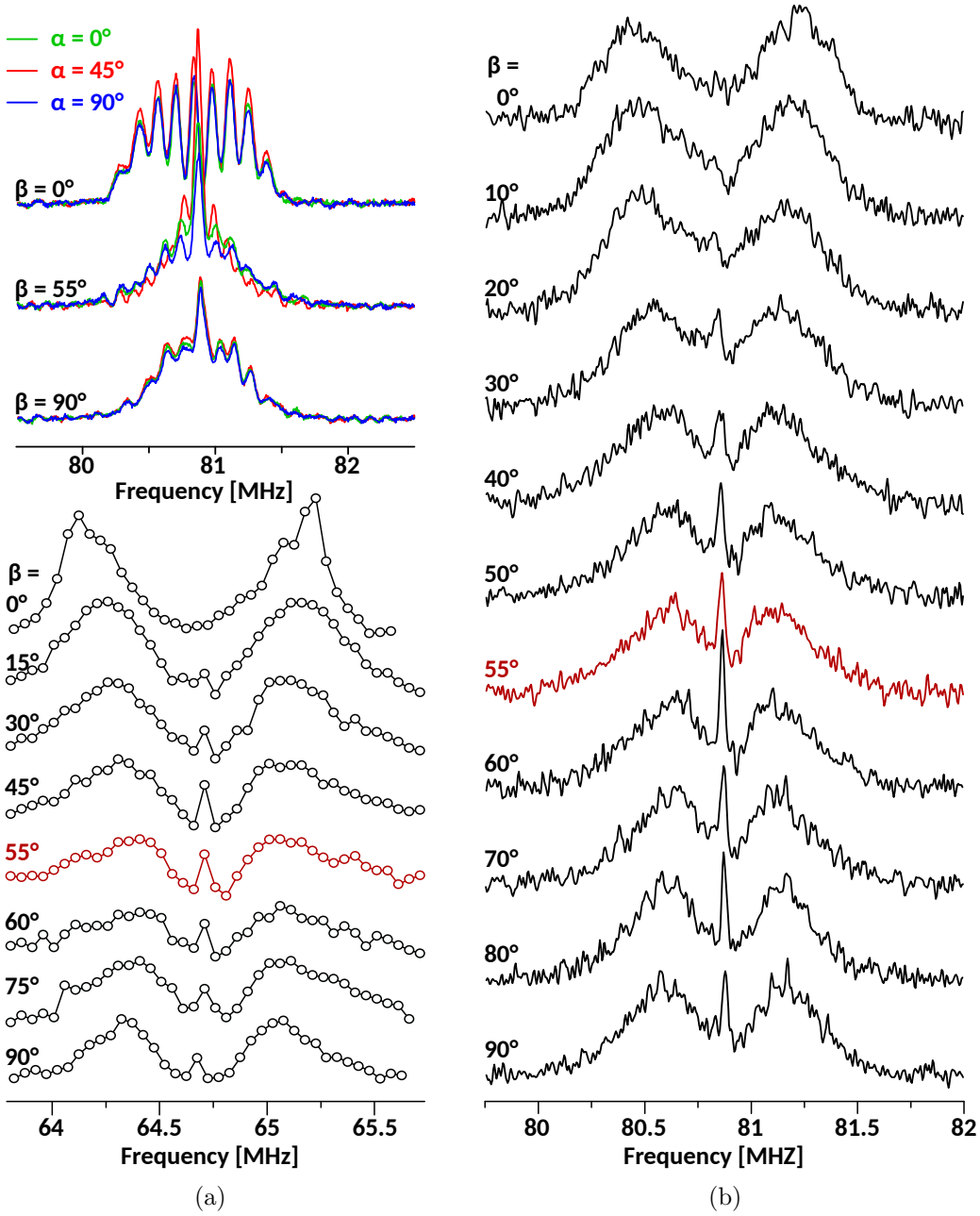

Figure 8.10 (a) In the upper panel, orientation dependent solid echo spectra ($\beta = 0°,\ 55°,\ 90°$) for three different orientations $\alpha = 0°,\ 45°,\ 90°$ (rotations about the crystal c-axis) obtained for $Bi_2Se_3^{**}$ at 11.74 T are given. In the lower panel, frequency stepped selective Hahn echo measurements with $\tau_{\pi/2} = 10\,\mu s$ and $\tau_\Delta = 45\,\mu s$ for a set of orientations between $\beta = 0°$ and 90° are presented (each data point represents a single measurement). Measurements taken at 9.39 T. (b) Orientation dependence of non-selective solid echo measurements with $\tau_\Delta = 45\,\mu s$ obtained from $Bi_2Se_3^{**}$ at 11.74 T.

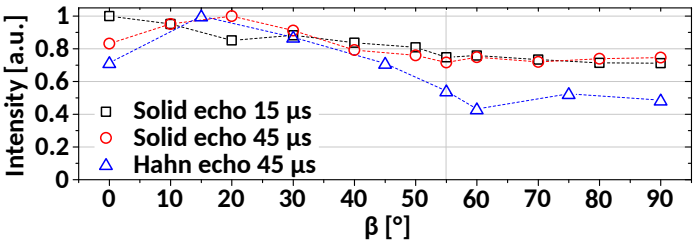

Figure 8.11 Total spectral intensities (area under curve) of the angular dependent measurements shown in Fig.8.9 and Fig.8.10.

Spin echo decay

Since the pulse separation time τ_Δ had such a strong effect on the total lineshape for $c \parallel B_0$ and at the magic angle, the orientation dependent measurements were repeated with $\tau_\Delta = 45\,\mu$s using the solid echo pulse sequence as well as a frequency stepped selective Hahn echoes. The results are shown in the lower panel of Fig.8.10(a) and in Fig.8.10(b). It has to be noted that due to selective excitation of the spin system by using Hahn echoes with long $\pi/2$-pulses ($10\,\mu$s), the excitation condition changes for different parts of the spectrum. The spectra shown in the lower panel of Fig.8.10(a) were obtained by using an excitation condition that corresponds to a second satellite (cf. nutation maxima in Fig.8.2). Furthermore, the spectra were not corrected for T_2.

The characteristic change of the total spectral shape is recovered for all the orientations. Interestingly, at orientations where a pronounced narrow line appears in the centre of the spectra in Fig.8.9, i.e. from 20° on, a narrow resonance survives the transverse decay for longer τ_Δ. This peculiar resonance line appears to be more pronounced in the non-selectively excited measurements (Fig.8.10(b)) than for the selective Hahn echo measurements as depicted in Fig.8.10(a) lower panel.

Intensities

The total signal intensities for the three different orientation dependent measurements have been evaluated by the area under each curve. The relative intensities as a function of β for each set of experiments are plotted in Fig.8.11. Under crystal rotation, about 25 % of the total spectral intensity gets lost for the spectra obtained from non-selective excitation (Fig.8.11 black and red). This is very different to the results published by Nisson et al. [20], where an intensity loss of up to 60 % was reported. For the selectively excited spectra (Fig.8.11 blue), i.e. the Hahn echo spectra with $\tau_\Delta = 45\,\mu$s, the total intensity varies strongly compared to the non-selective counterparts, going down to almost 40 % at $\beta = 60°$.

Interestingly, the maximum intensity for $45\,\mu$s is found to be around $\beta = 20°$ for both, solid as well as Hahn echo measurements, while for the solid echoes with $\tau_\Delta = 15\,\mu$s, the maximum intensity is found at $\beta = 0°$ ($c \parallel B_0$). The total variations in intensity when changing the relative crystal orientation of the single crystal must be assumed to be predominantly representing larger variations in T_2 accompanied by changing excitation conditions related to the used experimental parameters (pulse length and power level).

Key results: Orientation dependent ^{209}Bi NMR

- A broad ^{209}Bi signal is found independent of the crystal orientation (Fig.8.9).
- For sufficiently long pulse separation times, $\tau_\Delta = 45\,\mu$s, all the spectra assume a peculiar double-hump shape (Fig.8.10).
- A narrow line appears in the centre for $\beta \geq 20°$ for both short and long pulse separation times, τ_Δ (Figs.8.9 and Fig.8.10).
- A vanishing asymmetry parameter, $\eta = 0$, has been confirmed by additional orientation dependent measurements at $\alpha = 0°$, 45°, and 90°.

8.1.4 Carrier concentration dependence

Systematic measurements were also carried out on the three Bi_2Se_3 samples, the syntheses of which were described in Ch.5. As mentioned, the crystal synthesis followed the intention to make samples with different carrier concentrations, n, by growing crystals from melts with slightly different elemental composition, i.e. from a Bi-deficiency melt ($Bi_{1.95}Se_3$), from a stoichiometric ($Bi_{2.00}Se_3$), and from a Bi-excess melt ($Bi_{2.05}Se_3$). The investigation of additional samples of the same material allows to investigate how far the peculiarities reported in the previous sections are a general property of Bi_2Se_3 single crystals, and if they depend on the carrier concentration, n.

NMR shift, quadrupole interaction, and linewidth

The spectra obtained for $c \parallel B_0$ of four single crystals, $Bi_2Te_3^{**}$, $Bi_{1.95}Se_3$, $Bi_{2.00}Se_3$, and $Bi_{2.05}Se_3$ are given in Fig.8.12. The resonances in Bi_2Se_3 are subject to a carrier dependent NMR shift. That is, the ^{209}Bi quadrupole pattern is shifted to higher frequencies with increasing carrier concentration, n. The samples are order with

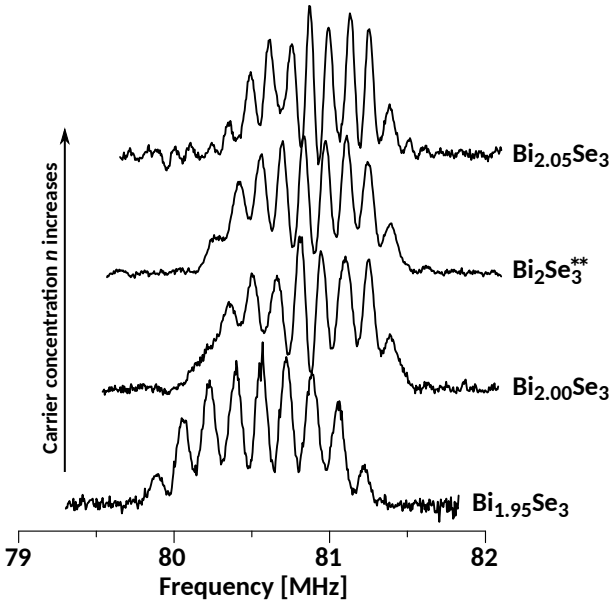

Figure 8.12 Non-selective solid echo spectra with $\tau_{\pi/2} = 0.75\,\mu$s and $\tau_{\Delta} = 15.5\,\mu$s obtained from samples with different carrier concentrations at $B_0 = 11.74\,$T.

respect to the intended (synthesis) and measured (Hall effect) change in carrier concentration. Moreover, it can be concluded that the single crystal $Bi_2Se_3^{**}$, which has not been studied by Hall effect measurements, has a carrier concentration between that of the samples $Bi_{2.00}Se_3$ and $Bi_{2.05}Se_3$.

For each sample, the NMR shift in terms of $K_{\rm iso}$ and $K_{\rm axial}$ was determined. The procedure includes the conversion of the centre frequencies of a given sample for angles from $\beta = 0°$ and $90°$ into the relative shift, K in ppm, with respect to $Bi(NO_3)_3$, using the secondary reference method introduced in Ch.4. $K(\beta)$ was then fit using

$$K(\beta) = K_{\rm iso} + K_{\rm axial}(3\cos^2(\beta) - 1)/2\ . \tag{8.3}$$

Results are listed Tab.8.1.

The quadrupole splitting decreases systematically with increasing carrier concentration, n, which, again, reproduces the ordering of the single crystals as suggested by the NMR shift, i.e. $Bi_2Se_3^{**}$ can be placed between $Bi_{2.00}Se_3$ and $Bi_{2.05}Se_3$. A clearly carrier dependent quadrupole interaction is a surprising result, because Nisson et al. [18] explicitly stated that they found no carrier dependence in their measurements. The quadrupole splitting for all samples are collected in Tab.8.1.

The individual linewidth represented by the central transition in each sample also seems to depend on the carrier concentration. The resonances are progressively

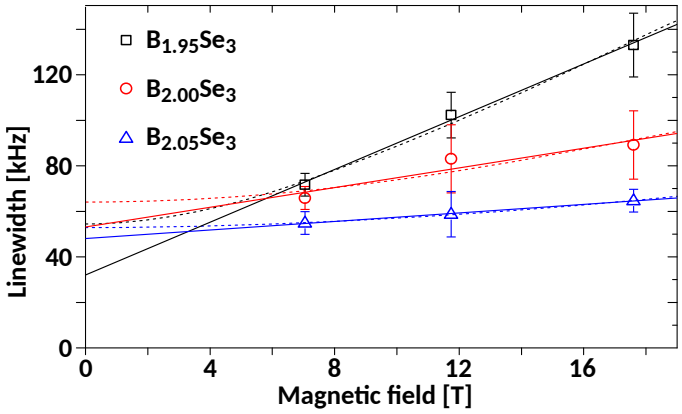

Figure 8.13 Linewidth of the central transition of the ^{209}Bi quadrupole pattern for $c \parallel B_0$ for three different magnetic field.

narrowing with increasing n. Again, the gradual narrowing is in agreement with the sample ordering as provided by the NMR shift and the quadrupole interaction.

The spectra of the three single crystals $Bi_{1.95}Se_3$, $Bi_{2.00}Se_3$, and $Bi_{2.05}Se_3$ have been measured for magnetic fields $B_0 = 7,\ 11.74$, and 17.6 T in order to evaluate field dependent and field independent linewidth components. The linewidths are assumed to be composed of two contributions, a field dependent linewidth, b, that reflects shift variations proportional to B_0, and a field independent contribution, Λ_0, that reflects broadening from dipole interactions. In order to separate both contributions, two different approaches were employed. Assuming both variations to be of Lorentzian shape, the total width is

$$\Lambda = \Lambda_0 + bB_0 \ . \tag{8.4}$$

This approach is represented by the solid lines in Fig.8.13. For both broadening effects originating from normal distributions, the total width is

$$\Lambda^2 = \Lambda_0^2 + (bB_0)^2 \ . \tag{8.5}$$

This approach is given by the dashed lines in Fig.8.13 upper panel.

The contributions to the NMR linewidth due to direct dipole interactions, 2.32 and 2.33, in $c \parallel B_0$ were estimated using the method of moments, (2.34) [84]. These dipole couplings are chiefly homonuclear due to the low abundance of ^{77}Se nuclei (7.6 %). It follows, that at $c \parallel B_0$ the next neighbours are the Bi atoms in the plane (ab-direction, cf. Fig.1.1). Their distance, ∼4.14 Å, is given by the length of the crystal a and b-axis (Tab.5.2). The NMR line broadening from these six next neighbours is calculated to ∼0.5 kHz. Including contributions from nuclei further

Table 8.1 Collected ^{209}Bi NMR parameters of the four single crystals. Documented are isotropic, K_{iso}, and axial, K_{axial}, shift components, the quadrupole splitting, ν_{Q}, as well as averaged field independent, Λ_0, and field dependent, b, linewidths.

sample	K_{iso} [ppm]	K_{axial} [ppm]	ν_{Q} [kHz]	Λ_0 [kHz]	b [kHz/T]	b [ppm]
$Bi_{2.05}Se_3$	7310(40)	-240(25)	128(3)	51(5)	2(0.5)	290(70)
$Bi_2Se_3^{**}$	7040(10)	-435(15)	141(3)	–	–	
$Bi_{2.00}Se_3$	6750(30)	-560(60)	147(3)	58(8)	3(0.5)	430(70)
$Bi_{1.95}Se_3$	5233(30)	-1954(75)	164(3)	43(11)	6.4(1)	905(140)

away and the few ^{77}Se nuclei, the total NMR line broadening of ^{209}Bi nuclei in Bi_2Se_3 for $c \parallel B_0$ from direct dipole interactions is estimated to be in the order of 1 to 1.5 kHz.

Orientation dependence

Orientation dependent measurements were carried out on $Bi_{1.95}Se_3$, $Bi_{2.00}Se_3$, and $Bi_{2.05}Se_3$ to investigate the spectral changes under crystal rotation and to compare the findings with the results obtained from the $Bi_2Se_3^{**}$ single crystal. The results are composed in Fig.8.14. All samples show a very similar behaviour. The spectra for $c \parallel B_0$ are well defined. As the relative orientation of the single crystals changes, the total intensity is reduced by about 25 to 30 %. At the magic angle, each spectrum shows a significant discrepancy from the simulation representing equation (2.38). The effect appears to be less pronounced in the low carrier sample $Bi_{1.95}Se_3$, and is very similar for all the other samples with $n \sim 10^{19}\,\mathrm{cm}^{-3}$.

Another common feature which is most pronounced for the higher carrier samples, i.e. $Bi_{2.00}Se_3$ to $Bi_{2.05}Se_3$, is a much broadened spectrum for $c \perp B_0$. With equation (8.2) and Fig.8.6, one expects the total spectrum's width to be reduced by about a factor of 2, when comparing orientations $c \perp B_0$ with $c \parallel B_0$. This is clearly not the case. The spectra are substantially broader for $c \perp B_0$ than their simulations, and show a peculiar shape with an unusual narrow resonance line in the centre.

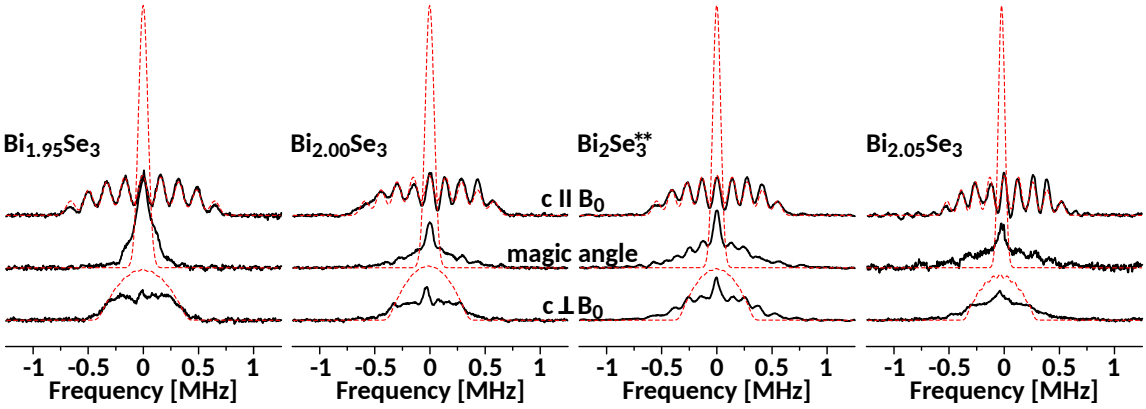

Figure 8.14 Angular dependent solid echo spectra of the single crystals shown in Fig.8.12. Red dashed lines represent first order quadrupole fitting for $c \parallel B_0$ (top) and the corresponding simulations at the magic angle (middle) and the for $c \perp B_0$ (bottom). Magnetic shifts have been subtracted.

Key results: Carrier concentration dependent ^{209}Bi NMR

- The NMR shift, the quadrupole interaction and the field dependent linewidth of ^{209}Bi in Bi_2Se_3 change systematically with the carrier concentration, n (Tab.8.1).
- A non-trivial orientation dependent quadrupole splitting is observed in all the samples. This unusual effect is less pronounced for the low carrier sample $Bi_{1.95}Se_3$ (Fig.8.14).

8.1.5 ^{209}Bi in Bi_2Se_3 powders

In Fig.8.15, spectra obtained from Bi_2Se_3 powders are shown. There are solid echo measurements with $\tau_{\pi/2} = 0.75\,\mu$s and pulse separation times $\tau_\Delta = 15\,\mu$s (Fig.8.15, top spectrum) and $45\,\mu$s (Fig.8.15, middle spectrum). Furthermore, frequency stepped Hahn echo measurements ($\tau_{\pi/2} = 10\,\mu$s and $\tau_\Delta = 45\,\mu$s) are shown in the bottom spectrum of Fig.8.15.

The powder spectra are of considerable total width, very similar to the total extent of the single crystal quadrupole pattern for $c \parallel B_0$, which is also included in Fig.8.15. This results is more independent evidence for a very unusual orientation dependence of the ^{209}Bi quadrupole splitting in Bi_2Se_3. It is in very good agreement with the orientation dependent single crystal spectra shown in Figs.8.9 and 8.10(b). Furthermore, as shown in Fig.8.15, the unusual T_2 effect observed in the single crystals, are also present in the powder.

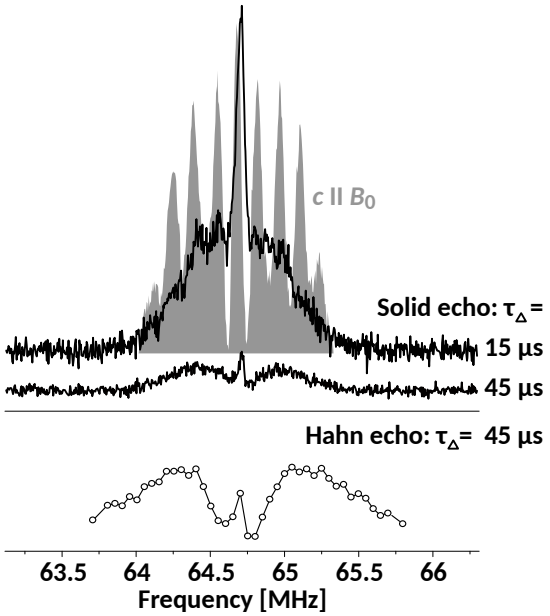

Figure 8.15 ^{209}Bi NMR of Bi_2Se_3 powder using non-selective solid echo experiments with $\tau_{\pi/2} = 0.75\,\mu$s shown in the upper panel. In the bottom panel, a spectrum obtained from frequency stepped selective Hahn echoes using with $\tau_{\pi/2} = 10\,\mu$s and $\tau_\Delta = 45\,\mu$s is shown. Measurements at 9.39 T.

8.2 Discussion

8.2.1 General analysis

NMR Shift

The shift variations under crystal rotation, i.e. the change of the resonance frequency of the centre of the quadrupole pattern as function of the crystal orientation, are small compared to the total width of the quadrupole spectra (cf. Fig.8.10(a)). From the angular dependent measurements, the shift was traced and found to be axially symmetric, in agreement with ^{77}Se, reflecting once more the cylindrical symmetry of the crystal structure. The results were presented in Tab.8.1.

The measured shift is the sum of two main components, a carrier dependent and a carrier independent NMR shift. Across the samples, significant changes of the NMR shift in terms of its isotropic, K_{iso}, and its axial, K_{axial}, component are observed. These changes must be attributed to changes in the carrier concentration, n, in agreement with earlier publications on NMR of Bi_2Se_3 [18, 21, 23, 76]. Thus, from the systematic changes of the NMR shift observed in the four samples under investigation, the samples can be ordered with respect to n. The order is in agreement with Hall effect measurements (cf. Ch.5) and follows the intention

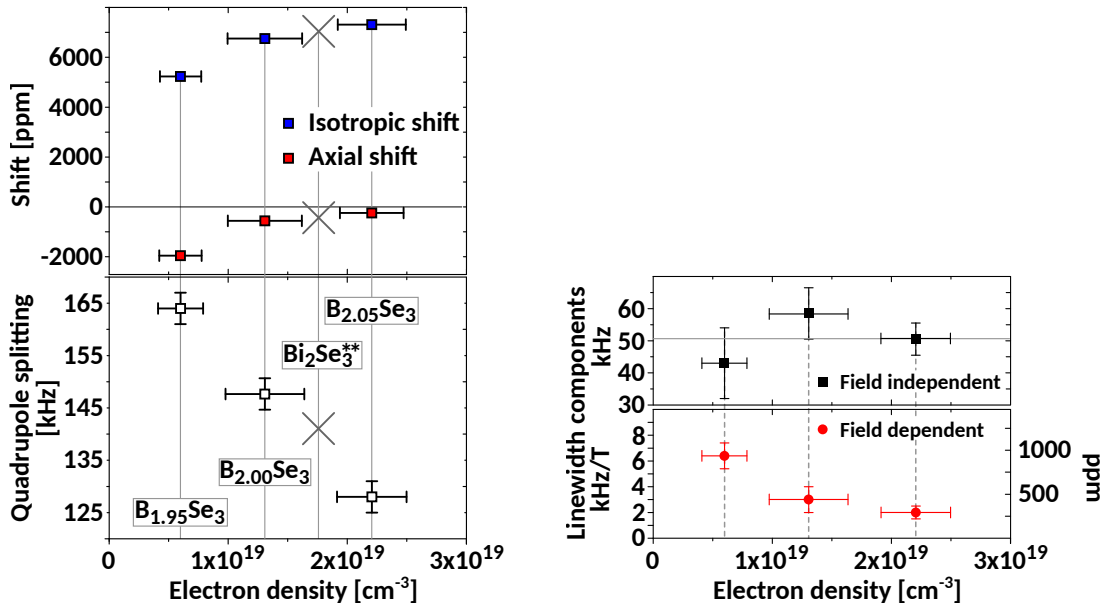

Figure 8.16 (a) The two shift components (upper panel) and the quadrupole splitting frequency (lower panel) as a function of the carrier concentration n. (b) The averaged linewidth components (Λ - field independent and b - field dependent see Tab.8.1), obtained from fittings described in the results section, as function of n.

of making samples with increasing n by increasing the relative amount of Bi in the melt. Recent results on the optical reflectivity of single crystals from the same batch as $Bi_{1.95}Se_3$, $Bi_{2.00}Se_3$, and $Bi_{2.05}Se_3$ confirm this finding and allow a coarse estimate of the carrier concentrations in the present samples [106].[4] The shift components as a function of n are given in Fig.8.16(a) upper panel.

With increasing carrier concentration, both shift components, K_{iso} and K_{axial}, change in positive direction. Thus, the carrier dependencies of K_{iso} and K_{axial} are positive. The changes observed for both shift components appear to follow a very similar square root dependence with respect to n, similar to what was reported by Mukhopadhyay et al. [21] in their supplementary information. A positive carrier dependent shift is in qualitative agreement with the calculations carrierd out by Boutin et al. [76]. Quantitative comparison is difficult due to the unknown carrier independent NMR shift. However, it can be concluded that the the carrier independent axial shift component (extrapolation to zero carriers in Fig.8.16(a)) is negative and surprisingly large.

[4]The carrier concentration from Hall effect measurements can only give an estimate as they were obtained from samples of the same synthesis batches, but not from the actual single crystals investigated with NMR.

Quadrupole interaction

For $c \parallel B_0$, the principle value, V_{ZZ}, of the of the electric field gradient's PAS is aligned with the external magnetic field. Thus, $\beta = 0$ and from equation (8.2) it follows that the splitting observed in this orientation represents the quadrupole splitting frequency, ν_Q. For each sample, the quadrupole pattern for $c \parallel B_0$ is found to be well defined, apart from some minor distortions that are attributed to instrumental limitations. The argument is based on the observations of almost the same widths of the central transition and the satellites. A distribution of EFGs will not affect the central transition, but will broaden the satellites gradually depending on their order, i.e. the 1st satellites are broadened by $\Delta\nu_Q$, the 4th satellites by $4 \times \Delta\nu_Q$. Thus, from the similar width of the individual resonances in the quadrupole patterns for $c \parallel B_0$, it must be concluded that the local environment for all Bi nuclei within one sample must be very similar, i.e. $\Delta\nu_Q < 5\,\%$. In other words, the well defined quadrupole interaction is a strong argument for rather homogeneous materials.

The quadrupole splitting is found to change systematically across the samples (Tab.8.1). There is no evidence that the lattice parameters change as a consequence of the changing doping level that results in the variations of the carrier concentration, n (cf. Ch.5). It must therefore be concluded that the quadrupole interaction changes in accordance with the carrier concentration and thus measures local charges from partially filled orbitals, rather than the background lattice. This is an important argument for the quadrupole interaction to be sensitive to the energy band inversion as will be discussed below.

Linewidths

The spectra shown in Fig.8.12, though rather well defined with respect to their quadrupole interaction, exhibit large individual linewidths (Tab.8.1). Georgieva et al. [23] have shown that the ^{77}Se linewidth in Bi_2Se_3 is governed by an unusual electronic spin susceptibility of Bloembergen-Rowland type that gives rise to a far ranging indirect nuclear dipole coupling. This can be seen as a dipole-dipole interaction that is significantly amplified as it is mediated by itinerant carriers.

In the case of ^{209}Bi nuclei, the calculations show similar extensive line broadening due to the enhanced dipole interaction. To investigate that in more detail, field dependent (7, 11.74, and 17.6 T) spectra of the samples $Bi_{1.95}Se_3$, $Bi_{2.00}Se_3$, and $Bi_{2.05}Se_3$ were evaluated. The spectra for $c \parallel B_0$ were fit with first order quadrupole patterns as shown in Fig.8.1 and Fig.8.14, from which the linewidth was obtained. In Fig.8.13, the measured widths as a function of the external magnetic field B_0 are

presented.

In both cases, significant field independent linewidths, Λ_0, are obtained from an extrapolation to $B_0 = 0$, ranging between 35 and 65 kHz. These values far exceed the line broadening due to direct dipole-dipole couplings of the Bi nuclei with neighbouring nuclear magnetic moments, especially when taking into account the low abundance ^{77}Se ($\sim$7.6 %) nearest neighbours. Furthermore, their relative orientation with respect to the external magnetic field, B_0, of 50° to 60°, reduces the coupling strength due to the $(3\cos^2(\beta) - 1)$-term (cf. (2.35) and (2.34)). Thus, the field independent NMR line broadening of ^{209}Bi nuclei cannot be explained by direct dipole-dipole interactions.

The field independent linewidth, Λ_0, varies across the samples, but shows no systematic change with the carrier concentration, n (Fig.8.16(b)). Unfortunately, the accuracy of the measurements and, thus, the accuracy of the fits is insufficient. The large values, $\Lambda_0 \approx 50(10)$ kHz, are nonetheless in good agreement with an unusual strong indirect coupling mechanism as suggested by Georgieva et al. [23] and Ramírez-Ruiz et al. [74]. However, due to large errors in Λ_0, the present results cannot strictly be taken as an additional proof of a Bloembergen-Rowland (BR) coupling. A BR mechanism is essentially independent of the carrier concentration, in contrast to the rivalling explanation of an RKKY mechanism, that depends on the density of states.

A field dependent linewidth component, b, has also been found, that appears to depend systematically on the carrier concentration (Fig.8.16(b), bottom panel). Note, b is less affected by the uncertainties mentioned above, and both fitting approaches yield almost the same results. Consistent with the observations reported by Nisson et al. [18], the lines get broader for decreasing carrier concentration, n.[5] This seems to be counter intuitive, because one would expect the higher impurity level to be accompanied by a higher degree of disorder, and thus, an increased broadening. The central question is, where does a magnetic field dependent linewidth come from in a single crystal?

As mentioned in the beginning of this discussion, the variations in shift observed across the samples are due to a change in carrier concentration. Thus, variations in linewidth could reflect distributions of the NMR shift within each sample. From the carrier dependence of the two shift components, it can be seen that a given variation of n yields a stronger effect for the low carrier samples than for the high carrier ones. This is in qualitative agreement with the larger linewidth for smaller

[5] Nisson et al. [18], however, looked at the total width, Λ, at a single field B_0

values of n. However, such a scenario seems to be in contradiction with the rather well defined and carrier dependent quadrupole interaction. A more careful study of the linewidth of ^{209}Bi in in Bi_2Se_3 is needed to resolve this problem.

Spin echo decay

The linewidth was interpreted in terms of a strong indirect nuclear coupling. Such an amplified dipole interaction must have direct consequences for the transverse relaxation of ^{209}Bi nuclei, because of their 100 % abundance. Indeed, T_2 relaxation is found to be extremely fast, down to only $\sim 15\,\mu$s for the central transition in $Bi_2Se_3^{**}$ (Fig.8.3(b)). Such a spin echo decay corresponds to a linewidth of approximately 30 kHz, which is in the same order of what is actually found, i.e. 65 kHz.

However, it is not finally proven that this most efficient spin echo decay originates from dipole couplings. Especially, the systematic variation of T_2 for different transitions as observed by selective Hahn-echoes in Fig.8.3, or by the change in lineshape of the total spectrum as depicted in Fig.8.4, cannot be understood from the sole presence of an indirect dipole interaction. It is also not reproduced by Redfield relaxation as assumed by Nisson et al. [20], though the latter approach does result in a change of transverse relaxation with growing satellite order in a quadrupole split spectrum. A comparison of $1/T_2$, as measured in this study for $c \parallel B_0$ and at the magic angle, as well as the expectation from Redfield theory [20], is presented in Fig.8.17.

In the current state of the investigations it is believed that the mechanism behind the slowing down of the spin-echo decay from the center of the quadrupole pattern to its outer regions, reflects the competition of the indirect coupling versus the quadrupole interaction, both being of a similar strength. One may include a small quadrupole broadening to support this scenario, that is, to introduce a progressively growing frequency mismatch among coupling partners from the same satellites. Further clarification, however, must be sought in future experimental investigations supported by model calculations.

Spin-lattice relaxation

The spin-lattice relaxation was measured selectively with the central transition for $c \parallel B_0$ and non-selectively at the magic angle (Fig.8.5). The results are in agreement with spin-lattice relaxation measurements reported by Young et al. [16] and Nisson et al. [18] at room temperature. The accelerated apparent relaxation of the central transition ($\sim 750\,\mu$s) at $c \parallel B_0$ compared to the non-selective T_1 at the magic

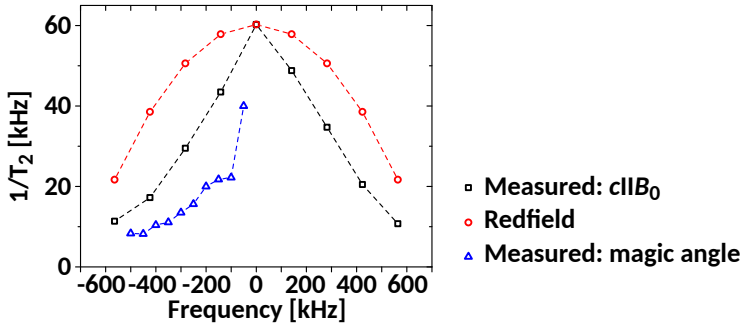

Figure 8.17 $1/T_2$ from measurements at $c \parallel B_0$ (black) and at the magic angle (blue). Also included (red) are the changes in $1/T_2$ for growing satellite order due to Redfield theory as assumed by [20].

angle ($\sim 7.5\,\mathrm{ms}$), reflects the typical behaviour of a quadrupole split system, where it makes a great difference whether a small number of spins (single transition) is brought out of equilibrium or all the spins (non-selective).

Georgieva et al. [23] found the T_1 for ^{77}Se to be on the order of a few seconds. As a spin 1/2, $^{77}T_1$ must be magnetic, i.e. the relaxation process depends on a coupling to free carriers. For bismuth, another relaxation channel via the quadrupole relaxation is possible. This was argued by Young et al. [16] for higher temperatures. However, a mixed relaxation mechanism including quadrupole and magnetic relaxation or even a pure magnetic relaxation cannot be excluded to this date, given the large number of free carriers.

Single crystals and powders

In their publication of orientation dependent ^{209}Bi NMR in Bi_2Se_3, Nisson et al. [20] reported a number of surprising results. They observed a severe loss in intensity of up to 60 %, when changing the relative orientation of the single crystal. Even More astonishingly, they reported a mismatch between averaged single crystal spectra and spectra obtained from microscopic powders and nanostructured samples. The powders showed an unusual double-hump spectrum, whereas the averaged single crystal spectrum had a more or less typical shape of a quadrupole powder pattern with the highest intensity in the center. Nisson et al. [20] mentioned the unusual T_2 effects in this system as argued by Young et al. [16]. However, it seems that they did not fully acknowledge the impact of the distributed T_2 on the overall lineshape of the quadrupole pattern (cf. Fig.8.4). Instead, they simulated the spectra using Redfield theory, which yields a much less pronounced variation of the T_2 (cf. Fig.8.17). Finally, they attributed the mismatch between single crystals and powder spectra to special screening effects due to topological surface states that give rise to a sort

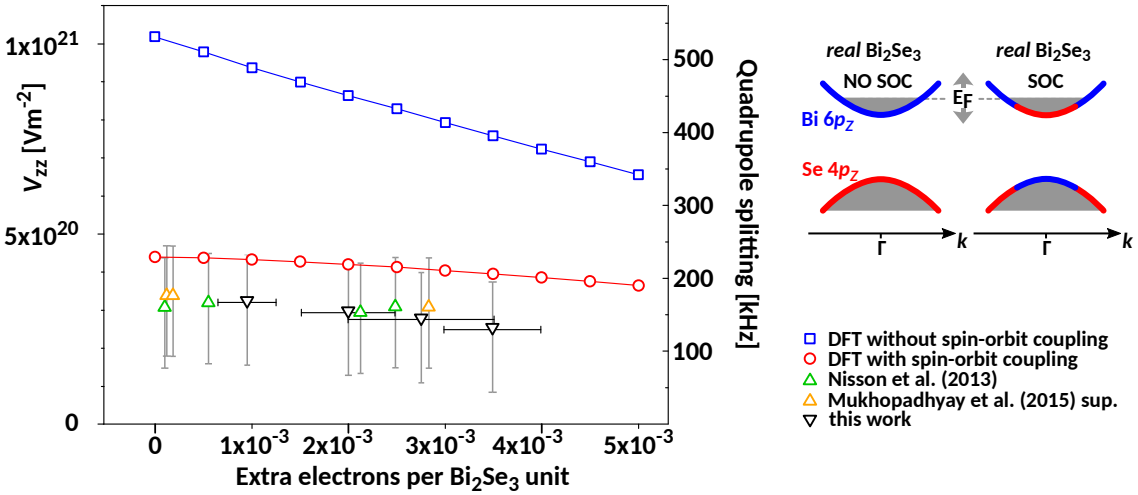

Figure 8.18 The EFG at the Bismuth site in terms of V_{ZZ} with (red) and without (blue) spin-orbit coupling obtained from DFT calculations as a function of carrier concentration (see [104] for details). Experimental results as calculated from the measured quadrupole splittings using (2.39) are included (triangles). In the upper panel on the right a scheme of the energy band structure near the Γ-point in both cases is presented.

of selection rule for the averaging of angular dependent single crystal spectra, i.e. the screening suppresses the signal intensity in some orientations.

In the current investigation, such a mismatch of single crystal and powder spectra was not observed. First, the intensity loss when changing the crystal orientation is much less than that found by Nisson et al. [20]. Second, when carefully taking into account the effect of T_2 with respect to the total lineshape, single crystal and powder spectra can easily brought into agreement. That is, when comparing the angular dependent spectra given in Fig.8.9 with the uppermost spectrum in Fig.8.15, there is no mismatch. Also, for longer pulse separation times, spectra given in Fig.8.10(b) agree with the spectrum in the middle of Fig.8.15, and those spectra presented in Fig.8.10(a), lower panel, match with the bottom spectrum in Fig.8.15. Thus, single crystal and powder spectra match, if the progress of the corresponding spin echo decay is carefully taken into account.

8.2.2 Quadrupole interaction and energy band inversion

When introducing the Bi_2Se_3 in the first chapter of this work, it was discussed that the central feature of the topologically non-trivial energy band structure is the band inversion occurring at the Γ-point in the Brillouin zone. The band inversion reverses the order of Bi $6p_z$ and Se $4p_z$ states, which gives rise to topologically protected surface states due to the opposite parity of the involved bands as shown

by Zhang et al. [7]. In Fig.8.18 on the right, a combined scheme of the band edge in real Bi_2Se_3 (from Fig.1.3) is presented, including the effect of spin-orbit coupling *and* self-doping.

In *real* Bi_2Se_3 *without* spin-orbit coupling (no band inversion), additional carriers due to native defects (grey area) will occupy predominantly Bi $6p_z$ states in the conduction band. In the case of spin-orbit coupling being switched on, the band inversion occurs and the additional electrons must be occupying Se p_4 states as well. This is, of course, a very simplified illustration of what is happening in Bi_2Se_3 due to spin-orbit coupling and self-doping. In fact, the spin-orbit coupling induces more changes, involving also p_x and p_y states. Furthermore, the change in relative occupations of the involved orbitals is below 1 %.

The quadrupole interaction, on the other hand, can be very sensitive and measure even fractions of charges changed by doping [89]. Thus, for the quadrupole interaction experienced by ^{209}Bi nuclei in Bi_2Se_3 – that measures local charges as argued above – the energy band inversion must be visible, because it makes a great difference whether additional charges occupy Bi or Se orbitals. In other words, in case of the band inversion, the Bi quadrupole interaction should be reduced as the charges move further away.

Since the spin-orbit coupling cannot be switched off in a real experiment, in order to compare both scenarios, i.e. quadrupole interaction with and without spin-orbit coupling, first principles calculations were employed. The calculations were carried out by Vojtěch Chlan form Charles University in Prague, Czech Republic, and are not part of the present work. For details the reader is referred to the publication Guehne et al. [104]. The results of the DFT calculations including quadrupole splittings as obtained in the present study and those reported by Nisson et al. [20] and Mukhopadhyay et al. [21] (where ν_Q *and* n are reported) are presented in Fig.8.18.

No spin-orbit coupling

The blue squares denote the EFG at the Bi sites in terms of V_{ZZ} for *real* Bi_2Se_3 *without* spin-orbit coupling. Here, the calculations show that predominately Bi p_z orbitals are gradually occupied which has a strong effect on the local EFG, and therefore changes ν_Q with increasing carrier concentration, n. The decrease can be interpreted as filling up Bi p_z orbitals towards a more symmetric or cubic local environment.

Spin-orbit coupling

In the case where spin-orbit coupling is enabled (red circles in Fig.8.18), a sudden drop of ν_Q occurs for the undoped system, i.e. at zero carriers. Charges are now transferred to Bi p_z states, while Se p_z states are less occupied. This is the real-space effect of the energy band inversion in terms of a redistribution of charges in the real space, reflecting Bi states being shifted into the valence band while Se states become a part of the conduction band. Adding carriers to this system changes the relative occupation of Bi p_z *and* Bi p_x and p_y states. The latter have only a minor effect on the local EFG, which is why the change of V_{ZZ} (or ν_Q) with the carrier concentration is less pronounced compared to the case without spin-orbit coupling.

The results from actual measurements (Fig.8.18 triangles) are in good agreement with the calculations when spin-orbit coupling is enabled. That the calculations do not exactly match the experiment originates from a number of uncertainties. First, the DFT calculation cannot implement van-der-Waals interactions that couple quintuple layers to each other, affecting the optimisation of crystal lattice parameters, namely the length of the c-axis. Secondly, as represented by the gray error bars, the quadrupole moment of ^{209}Bi is documented with a range of values. For calculating V_{ZZ} from the quadrupole splitting via (2.39), the standard value from 2001 of the quadrupole moment of Bismuth, $|Q_{Bi}| = 510\,\text{mb}$, was used [107]. In the same publication, values ranging between $Q_{Bi} = -370\,\text{mb}$ and $-710\,\text{mb}$ are collected that were reported in earlier papers using various experimental and theoretical approaches. Note that in the experiment only $|V_{ZZ}|$ can be determined, not its sign.[6]

8.2.3 An orientation independent quadrupole splitting due to strong spin-orbit coupling

Orientation dependent measurements of the ^{209}Bi spectra revealed a peculiar behaviour of an almost orientation independent quadrupole splitting. That is, in contradiction to the expectations given by equation (8.2), the total spectral width of the first order quadrupole spectrum does not change with β (Fig.8.9), and individual features such as the peaks of the satellites remain visible and unshifted throughout the crystal rotation. Especially the broad resonance at the magic angle does not fit into the basic understanding represented by (2.38) or (8.2). Furthermore, evidence for a non-selective excitation in the center at the magic angle was found, a fact that *is* in agreement with (8.2). Thus, an important question concerns the relative

[6] The sign of ν_Q and therefore of V_{ZZ} can only be determined at low temperatures.

intensity of the broad and the narrow resonance line at the magic angle. Or, in other words, how much of the sample is represented by the unusual broad line?

Whether the unusual broad resonance is evident or not was investigated with great care during the study. It must be noted that due to the rapid T_2 decay, found in the present system, in conjunction with limitations of the NMR spectrometers, it is difficult to provide a clear account for the relative intensity of both NMR resonance lines beyond a certain error. From the non-selective orientation dependent measurements shown in Fig.8.9 and other approaches, it is concluded that the narrow line at the magic angle represents a smaller fraction part of the whole Bi spectrum, most probably less than 10 %.

Support for the latter conclusion is provided by the following considerations. When consulting the angular dependence as shown in Fig.8.9, one finds that the narrow line emerges as soon as β approaches $\sim 20°$, (which is, again, *not* in agreement with (8.2)). However, the broad resonance that is evidently subject to quadrupole interaction, must have a corresponding central transition in its center. Hence, the narrow line (at the magic angle and elsewhere) is to a great part the central transition of the surrounding quadrupole pattern. The non-selective resonance at the magic angle, on the other hand, is over-emphasised because of its *non-selective nature* (2.43), and, thus, represents a rather small fraction of the sample.

The unusual orientation dependent spectra given by a broad distribution of resonances in Fig.8.9 is an evident property of the ^{209}Bi NMR in Bi_2Se_3. It is found in all single crystals under investigation (Fig.8.14), especially in those having higher carrier concentration ($n \sim 10^{19}\,\mathrm{cm}^{-3}$). The conclusion is supported by the extensively broadened spectrum obtained from commercial Bi_2Se_3 powder (Fig.8.15).

The total width of the Bi quadrupole spectrum under crystal rotation as shown in Fig.8.9 violates equation (8.2), because it remains essentially the same, about $\pm 600\,\mathrm{kHz}$. The reason for such a behaviour must lay in the angular dependent part of equation (8.2), rather than in a change of the quadrupole coupling strength. Most surprisingly, as indicated by the dashed blue lines in Fig.8.9, peaks and valleys that define satellite transitions for $c \parallel B_0$ are visible for any other angle β, and one is inclined to conclude that the satellites do not move at all under crystal rotation. That is to say, the splitting seems not to change, irrespective of a change in relative crystal orientation.

A simple explanation for the most unusual results is an *orientation independent* quadrupole splitting that is due the strong spin-orbit coupling of conduction electrons that yields the B_0 field direction to provide the quantisation axis for the EFG.

In the general expression of the quadrupole interaction, the EFG is given by

$$V_{ZZ} = eq = 2\langle Jm_J = J|V_0^{(2)}|Jm_J = J\rangle \ , \tag{8.6}$$

where $|J, m_J\rangle$ denotes the state of the electron with its total angular momentum J, and

$$V_0^{(2)} = \sqrt{\frac{4\pi}{5}} \int \frac{\rho_\mathrm{e}}{r_\mathrm{e}} Y_{20}(\theta_\mathrm{e}, \phi_\mathrm{e}) d\tau_\mathrm{e} \ . \tag{8.7}$$

Finally, the effective Hamiltonian of the quadrupole interaction reads

$$\mathcal{H}_\mathrm{Qeff} = \frac{3I_z^2 - I(I+1)}{2I(2I-1)} eQ \cdot \langle \psi_\mathrm{e}|V_0^{(2)}|\psi_\mathrm{e}\rangle \ , \tag{8.8}$$

with an effective electronic wave function ψ_e.[7]

In usual systems with weak or no spin-orbit coupling, the spin S of an electron can be neglected and the EFG originates from the electronic orbital momentum L. The latter, L, is obviously tied to the chemical structure, while the former, S, follows the external magnetic field.

In a strongly spin-orbit coupled system such as Bi_2Se_3, S and L cannot be regarded independently, and the total electron angular momentum, $\boldsymbol{J}$, has to be used instead. With its magnetic moment, $\boldsymbol{J}$ is quantised along the magnetic field direction, and thus the corresponding EFG (8.6) may "follow" the external field B_0.

For $c \parallel B_0$, the relative orientation of the EFG in the crystal structure is the same as in the case without spin-orbit coupling, i.e. the EFG's principle axis, V_{ZZ}, is parallel to the crystal c-axis, yielding the well defined quadrupole pattern as discussed above. When the crystal is rotated away from $c \parallel B_0$, equation (8.2) holds no longer due to the effect of the spin-orbit coupling on the EFG, that ties the electronic spin and its orbital angular momentum together. Instead, the quadrupole splitting remains chiefly unaffected by the crystal rotation, because the EFG's orientation follows B_0, and the orientation dependent NMR spectra do not undergo the expected changes with the crystal orientation (compare simulation and measurement in Figs.8.9, 8.10(a), and 8.10(b)).

This scenario provides a simplified picture of what may happen during the crystal rotation. There are a few minor aspects that are not readily explained, especially the narrow, non-selective resonance found at the magic angle. Additional evidence, however, is provided by the effective electronic g-factor of conduction electrons in

[7] For more details the reader is referred to [104].

Bi_2Se_3, as reported by Köhler and Wöchner [108]. They determined $g_{\text{eff}} = 32$ and 23 for $c \parallel B_0$ and $c \perp B_0$, respectively. Recently, Wolos et al. [109] measured the electron paramagnetic resonance (EPR) of conduction electrons in Bi_2Se_3 confirming the results reported by Köhler and Wöchner [108]. EPR, however, is an eye opener because it actually measures the Larmor precession of a spin 1/2 system, i.e. the quantisation along B_0, with a large g-factor, evidently representing the electron's total angular momentum $\boldsymbol{J}$.

8.3 Summary

The NMR of ^{209}Bi in Bi_2Se_3 single crystalline samples unveiled a whole variety of peculiarities, which potentially have far reaching implications for the NMR of topological states of matter and the NMR of strongly spin-orbit coupled systems.

The ^{209}Bi quadrupole patterns and changes of the line shape induced by unusual T_2 effects have been studied in detail. By that, the reported discrepancies between single crystal and powder spectra could be resolved. That is, single crystal and powder spectra can easily be brought in agreement when compared with each other at identical periods of time after excitation. The mechanism behind the transition selective spin-echo relaxation (T_2) is still not understood. It appears, however, that it results from the competition between dipole and quadrupole interactions, perhaps indicating a very sensitive dependence on a small quadrupolar broadening. The large magnetic field independent linewidth, which is related to the remarkably fast spin-echo decay, is a strong support for the Bloembergen-Rowland type of indirect nuclear dipole coupling as found with ^{77}Se NMR.

The quadrupole interaction experienced by the spin 9/2 nuclei of the ^{209}Bi isotopes proves to be a most powerful tool for the study of Bi_2Se_3. Most importantly with respect to the non-trivial topology of the band structure, the quadrupole coupling is sensitive to the band inversion in quantitative agreement with first-principle calculations. This means that the investigated single crystals are identified as topological insulators on a basis of an averaging over the whole macroscopic sample. This is a very different approach compared to the more common methods such as ARPES, which rely on small surface areas of the investigated sample. Thus, the effect might in future be used to investigate the energy band structure of materials where the topological non-trivial features move into the bulk such as is found in Weyl or Dirac semimetals.

Most astonishing from the NMR point of view is the finding of an orientation independent quadrupole interaction. This observation is in clear contradiction with

the expected changes in the quadrupole spectrum due to the symmetry of the electric field gradient. To account for the finding, a scenario is proposed where the electric field gradient is quantised along the external magnetic field due to the strong spin-orbit coupling of the conduction electrons, rather then being tied to the chemical structure. The implications from this scenario concern the NMR of quadrupole nuclei in strongly spin-orbit coupled systems in general. In future projects, similar effects should be researched in related materials.

Conclusions and outlook

In the present work the results of a broad study using a variety of experimental methods to investigate the bulk properties of bismuth based topological insulators is presented. Ferromagnetism in Mn doped Bi_2Te_3 is shown to disappear with grinding and sintering of the samples. A large positive magnetoresistance is observed, as well as a change in sign of the thermopower for increasing Mn content. A central result of this study is that the defect chemistry has a crucial impact on the properties of the material. The essence of the magnetic, thermopower, and magnetotransport measurements is that the samples under investigation are spatially inhomogeneous. Consequently, the results from measurements of the bulk properties such as resistivity, may not necessarily represent the whole sample, but rather a fraction.

A local probe like NMR that averages the whole sample, should provide a different perspective on the homogeneity of the materials under investigation. From the results of NMR measurements of single crystalline samples of Bi_2Te_3, however, it is difficult to decide whether the material under investigation is homogeneous or not. The chief reason is that the NMR resonance lines are dominated by an unusual strong indirect nuclear dipole coupling that causes extensive NMR line broadening. Besides, a magnetic field dependent NMR line broadening has been found. The latter must be related to a distribution of NMR shifts and, thus, could imply local variations of the carrier density. From the limited samples investigated with NMR in the present work, however, it is difficult to estimate the magnitude of these variations as this requires the relation between NMR shift and carrier density to be known. In future studies, a greater set of well characterised single crystals of Bi_2Te_3 with different carrier concentrations probed with NMR may help to determine whether the inhomogeneity of the materials as discussed in the context of magnetic, thermopower, and magnetotransport measurements is related to regions with higher and lower carrier densities or due to enhanced scattering. The latter cannot be seen with NMR.

Undetermined remains the mechanism behind the long-range interaction of magnetic moments in Mn doped Bi_2Te_3. A number of theoretical studies suggest a Ruderman–Kittel–Kasuya-Yosida (RKKY) type of coupling, i.e. an interaction through mediated by conduction electrons. However, the experimental evidence is weak, and some reports are even contradictory as there seems to be no correlations between the formation of a ferromagnetic phase and the carrier density, which would be a key requirement for RKKY. The fact that the magnetic order disappears with grinding and sintering of the samples may be an important observation for future studies.

Furthermore, with ^{77}Se NMR it has been shown that instead of an RKKY coupling, a slowly decaying Bloembergen-Rowland (BR) mechanism dominates the indirect dipolar coupling between distant nuclear magnetic moments in heavily doped Bi_2Se_3 single crystals. The corresponding model calculations hold likewise for nuclear moments in Bi_2Te_3. In the present work, the ^{125}Te NMR in Bi_2Te_3 shows evident similarities to the ^{77}Se NMR in Bi_2Se_3, especially a substantial indirect dipole coupling has been identified. Hence, it is likely that a BR coupling also dominates the ^{125}Te NMR in Bi_2Te_3. Consequently, a highly effective BR coupling would cause the long-range interaction among magnetic moments in magnetically doped Bi_2Te_3 as studied in this work. A BR coupling depends predominately on the band gap rather than on the density of states, and would therefore remain unchanged under an increase of the carrier concentration, in agreement with some experiments.

Systematic research of magnetically doped Bi_2Te_3 with a number of carrier concentrations for each doping level should be undertaken to study the mechanism of the ferromagnetic ordering through its dependence on the density of free carriers and the density of magnetic moments. NMR measurements of undoped samples should be carried out in order to verify the presence of a BR coupling. Furthermore, NMR measurements of Mn doped single crystalline samples may be used to check the suggested phase segregation because paramagnetic and ferromagnetic regions must exhibit different NMR shifts and NMR linewidths.

The reason why reports of NMR in Bi_2Se_3 and Bi_2Te_3 are so rare must clearly be sought in the difficulty to achieve reliable results within reasonable timeframe and the variety of entangled mechanisms that need to be understood separately. But with the quadrupole NMR of ^{209}Bi in Bi_2Se_3 being finally understood, a very powerful tool has been found that may allow the identification and study of topologically non-trivial states of matter through their bulk band inversions. That is, the present work proposes to view topological non-trivial band structures also from the perspec-

tive of their real-space effects. It has been shown that the quadrupole interaction experienced by ^{209}Bi nuclei measures local charges and is therefore sensitive to variations in the occupation of orbitals induced by the band inversion. It should also be noted that in related topological non-trivial material classes, such as Weyl semi metals, the Dirac-cones and thus the special electronic states are bulk features, rendering popular methods such as ARPES or STM insufficient due to their limitation to surfaces. A bulk probe like NMR could thus prove essential for the investigation topological states of matter in general.

Besides deepening the understanding of bulk electronic states in Bi_2Te_3 and Bi_2Se_3, ^{209}Bi quadrupole NMR can also be used to renew the attempt of studying nano grained powders in order to access surface electronic states. Particle size dependent quantum confinement effects in the band structure should be observable through the quadrupole splitting as well. It would further be interesting to study the Bloembergen-Rowland coupling with decreasing particle size, which is also connected to the band gap. Finally, the surface states may exhibit a very different quadrupole splitting besides their shift and spin-lattice relaxation. All these considerations, however, require very well defined nanoparticles as well as theoretical support.

Charge puddles, i.e. metallic islands in an otherwise insulating system, are another interesting consequence of the defect chemistry in highly compensated relatives of Bi_2Se_3 and Bi_2Te_3, such as Bi_2Te_2Se or $Bi_{1.08}Sb_{0.9}Sn_{0.02}Te_2S$. Especially the latter is reported to show a minimum of free carriers with the Fermi level presumably within the gap. Poorly screened band bending should then give rise to charge puddles if the conduction or valance bands cross the Fermi level. In an actual NMR experiment including low temperatures, nuclei that are located in the charge puddles must show a quite different shift, perhaps a different T_1, compared to those in actually gapped regions.

The most surprising finding of an orientation independent quadrupole splitting shown by ^{209}Bi nuclei in Bi_2Se_3 single crystals is argued to stem from the strong spin-orbit coupling of conduction electrons. The observation suggests that the electric field gradient (EFG) follows the external magnetic field, B_0, rather than being tied to the crystal structure, as is usually found in quadrupolar split systems. Since the EFG represents the local configuration of charges, its unusual rotation with B_0 seems to imply that local charge densities are to some extent affected by the external magnetic field. A more detailed experimental study in combination with a theoretical analysis may help to develop a clear understanding of how the involved electronic states are affected.

Another obvious question is whether this effect is related to the non-trivial band structure of Bi_2Se_3 or if it is a sole result of the spin-orbit coupling. The angular dependence of related heavy element compounds with and without band inversion should therefore be investigated in future projects. Clearly, ^{209}Bi in Bi_2Te_3 will be a natural next step. Also other topological insulators might be studied, such as Bi_2Te_2Se or Sb_2Te_3. Semiconductors with large g-factors such as InSb ($g_{\text{eff}} \approx -52$) or InAs ($g_{\text{eff}} \approx -15$), on the other hand, can be used as topologically trivial counterparts with strong spin-orbit coupling. This effect is clearly of fundamental relevance in the field of NMR of strongly spin-orbit coupled systems.

Appendix

Hahn echo nutation with full phase cycling

The common Hahn Echo (HE) phase cycling is given in the following Tab A1. Here, the first and second pulses are denoted as "$\pi/2$" and "π", meeting the conditions $\omega_{\mathrm{rf}}\tau = \pi/2$ and $\omega_{\mathrm{rf}}2\tau = \pi$, respectively.

Table A1 The Hahn-echo phase cycling. The first pulse is represented by the first column, the second pulse by the second column and the reading direction (phase) is given in the last column. Every row represents one experiment. During signal averaging, the four rows represent four individual experiments. After that, the starting phase is adjusted as $x \to y$ and according to that, all the other phases are "rotated" by 90°, i.e. $y \to -x$, $-x \to -y$, and $-y \to x$. Since only the relative phases are of interest, considering the four sets of phases as given in table is enough for the present investigation.

$\pi/2$	π	read
x	y	y
x	$-y$	y
x	$-x$	$-y$
x	x	$-y$

In the following discussion, a nutation experiment using the full Hahn echo phase cycling, which is 4 times the 4 cycles given in the table above, will be considered and it will be shown that the total induced signal which is proportional to the projection of the magnetization $\boldsymbol{M}$ onto the xy-plane follows a $\sin^3(\omega_{\mathrm{rf}}\tau)$ relation.

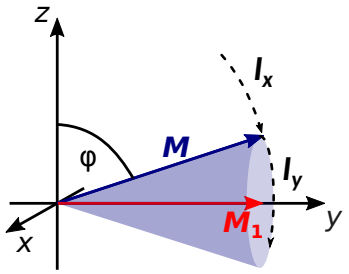

Figure A1 The I_x-pulse of length τ rotates the magnetization $\boldsymbol{M}$ (in equilibrium along the z-direction) about the x-axis by an angle $\varphi = \omega_{\mathrm{rf}}\tau$. $\boldsymbol{M}$ remains in the yz-plane. The subsequent I_y-pulse of twice the length of the former, i.e. 2τ, rotates $\boldsymbol{M}$ around the y-axis. No matter how long the second pulse is applied for, the projection of $\boldsymbol{M}$ onto the xy-axis remains unchanged and is therefore determined solely by the first pulse I_x.

Perpendicular pulses

An $I_x(\tau)$ pulse (of duration τ) is followed by a $I_{\pm y}(2\tau)$ pulse (of duration 2τ). The first pulse, I_x, rotates the magnetization, $\boldsymbol{M}$, about the x-axis by an angle $\varphi = \omega_{\mathrm{rf}}\tau$. The second, perpendicular pulse, $I_{\pm y}(2\tau)$, leaves the magnetization to move on a cone around $y-$axis for a time 2τ as indicated in Fig.A1. The angle enclosed by M and the $y-$axis, and therefore the projection of $\boldsymbol{M}$ onto the y-axis has not changed after the second pulse, and the measured magnetization, M_1, is solely determined by the first pulse with $\varphi = \omega_{\mathrm{rf}}\tau$, i.e.

$$M_1 = M_2 = M\sin(\varphi)\ , \tag{9}$$

where M is the length of the vector $\boldsymbol{M}$ representing the size of the magnetization. The result holds for both cases, a $I_y(2\tau)$ (M_1) and a $I_{-y}(2\tau)$ (M_2) second pulse, and is the same as for an FID nutation.

In-plane pulses

First, an $I_x(\tau) - I_{-x}(2\tau)$ sequence is considered. The first pulse, $I_x(\tau)$, rotates $\boldsymbol{M}$ within the yz-plane by an angle $\varphi = \omega_{\mathrm{rf}}\tau$ (see Fig.A2). The second pulse, $I_{-x}(2\tau)$ rotates $\boldsymbol{M}$ about the same axis but in opposite direction (thus $\boldsymbol{M}$ remains in the yz-plane). And since the second pulse is twice the duration as the first pulse, the angle enclosed by M and the y-axis $(\pi - \varphi)$ does not change. The magnetization and its projection onto the y-axis are now pointing in the negative y direction (true for $\omega_{\mathrm{rf}}\tau < \pi$). The measured magnetization becomes

$$M_3 = M\sin(-\varphi) = -M\sin(\varphi)\ , \tag{10}$$

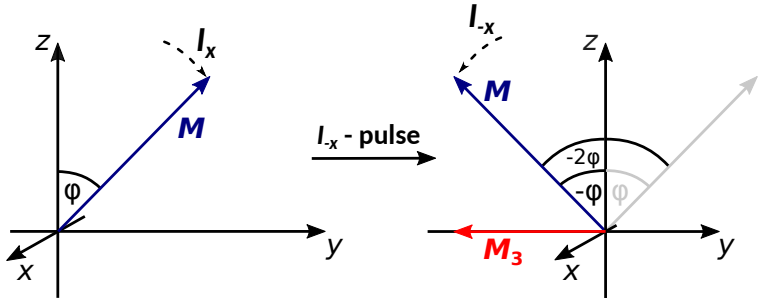

Figure A2 The first pulse $I_x(\tau)$ rotates $\boldsymbol{M}$ about the y-axis by an $\varphi = \omega_{\mathrm{rf}}\tau$. The second pulse rotates $\boldsymbol{M}$ about the same axis but in opposite direction for twice the duration of the first pulse, i.e. 2τ. The result is the mirror image of $\boldsymbol{M}$ after the first pulse at the xz-plane. Thus, the second pulse changes the sign of the projection of $\boldsymbol{M}$ onto the y-axis, not its length. The projection onto the y-axis gives the measured magnetization of size M_3.

again the same result as for an FID nutation when *read* in the $-y$ direction.

The last case concerns the $I_x(\tau) - I_x(2\tau)$ sequence. Again, the $I_x(\tau)$ pulse rotates $\boldsymbol{M}$ about the x-axis by an angle $\varphi = \omega_{\mathrm{rf}}\tau$. $\boldsymbol{M}$ can now be split into its y and z components, M_y and M_z (cf. Fig.A3), yielding

$$M_y = M\sin(\varphi) \tag{11}$$
$$M_z = M\cos(\varphi)\ . \tag{12}$$

The second pulse, $I_x(2\tau)$, is then applied to each component individually. The resulting vectors $\boldsymbol{M'_y}$ and $\boldsymbol{M'_z}$ will again have a y and a z-component:

$$M_{zy} = M_z\sin(2\varphi) = M\cos(\varphi)\sin(2\varphi) \tag{13}$$
$$M_{zz} = M_z\cos(2\varphi) = M\cos(\varphi)\cos(2\varphi) \tag{14}$$
$$M_{yz} = M_y\sin(2\varphi) = M\sin(\varphi)\sin(2\varphi) \tag{15}$$
$$M_{yy} = M_y\cos(2\varphi) = M\sin(\varphi)\cos(2\varphi)\ . \tag{16}$$

Finally, only the y-components, that is, the projections on the y-axis, are of interest. The measured magnetization becomes

$$M_4 = M_{zy} + M_{yy} = M[\cos(\varphi)\sin(2\varphi) + \sin(\varphi)\cos(2\varphi)]\ . \tag{17}$$

This results can be obtained with a much easier approach. Because the first and the second pulse are in phase, they can be combined to a single pulse of 3 times

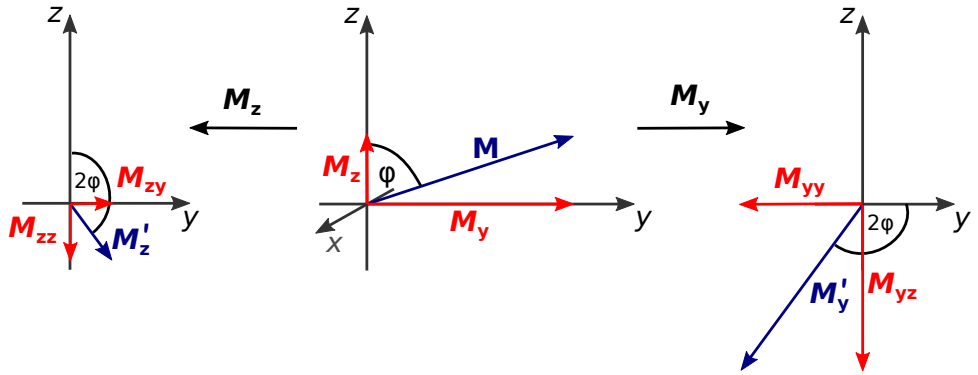

Figure A3 The first pulse $I_x(\tau)$ rotates $\boldsymbol{M}$ about the y-axis by an $\varphi = \omega_{\mathrm{rf}}\tau$ as in all the other cases (middle). In order to see what happens due to a second I_x pulse, it is helpful to divide the magnetisation $\boldsymbol{M}$ into its y and z component. The second pulse then acts individually on both components (left and right panels). The y-components of the resulting magnetizations $\boldsymbol{M}'_y$ and $\boldsymbol{M}'_z$ are finally summed up for the total magnetization M_4.

the duration of the first pulse.[8] Therefore, The HE nutation with in-phase pulses *looks* like an accelerated FID nutation with an effective $\tau' = 3\tau$. The measured magnetization should therefore follow

$$M_4 = M\sin(3\varphi)\ . \tag{18}$$

And indeed, using the tabled relations

$$\sin 2x = 2\sin x\cos x \tag{19}$$

$$\cos 2x = 1 - 2\sin^2 x \tag{20}$$

and

$$\sin^2 x + \cos^2 x = 1 \tag{21}$$

(17) becomes

$$M[\cos(\varphi)\sin(2\varphi) + \sin(\varphi)\cos(2\varphi)] \tag{22}$$

$$= M[2\sin(\varphi)\cos^2(\varphi) + \sin(\varphi)\{1 - 2\sin^2(\varphi)\}] \tag{23}$$

$$= M[\sin(\varphi)\{1 + 2\cos^2(\varphi) - 2\sin^2(\varphi)\}] \tag{24}$$

[8] transverse relaxation does reduce the M between the first and the second pulse but since this happens in all the cases described above, it can be ignored

$$= M[\sin(\varphi)\{1 + 2(1 - 2\sin^2(\varphi))\}] \quad (25)$$

$$= M[3\sin(\varphi) - 4\sin^3(\varphi)] \quad (26)$$

$$\equiv M\sin(3\varphi)\ . \quad (27)$$

Thus, the in-phase HE nutation can be looked at as a FID nutation with a single pulse of 3 times the duration of the first HE pulse.

A complete cycle

Now the individual experiments with the four different phase cycling sequences are added together. To do so, one has to take the *reading* direction into account which is given in the last column in Tab.A1. This follows the requirement, that in any case, a $\pi/2$-π pulse sequence should give the positive maximum, or, in other words, that

$$M_1(\varphi = \pi/2) = M_2(\varphi = \pi/2) = M_3(\varphi = \pi/2) \equiv M\ . \quad (28)$$

The total signal of a complete phase cycle will then be

$$M_{total} = M_1 + M_2 - M_3 - M_4 \quad (29)$$

$$= 2M\sin(\varphi) - (-M\sin(\varphi)) - M\sin(3\varphi) \quad (30)$$

$$= 3M\sin(\varphi) - M(3\sin(\varphi) - 4\sin^3(\varphi)) \quad (31)$$

$$= 4M\sin^3(\varphi) \quad (32)$$

In conclusion, the use of full phase cycling for Hahn echo nutation does not obscure the result for pulse length optimization while keeping the full advantage of phase cycling to reduce artefacts. The difference between the $\sin x$ function of an FID nutation and the $\sin^3 x$ function of a phase cycled HE nutation is presented in Fig.A4. Close to the optimal pulse length, i.e. the $\pi/2$-condition, the $\sin^3 x$ function converges to the $\sin x$ function, which is an important result as a $\pi/2$-condition is universal and does not depend on the number of pulses. Away from the maximum, the $\sin^3 x$ function deviates from a simple sine, essentially narrowing and approaching a typical zero slope for multiples of π including zero. This can be regarded as an advantage because the maximum ($\pi/2$-pulse) can thereby be easier identified and the particular form of the the $\sin^3 x$-function between $\varphi = 0°$ and π may help the fitting where a perfect excitation of the spin system is not easily achieved.

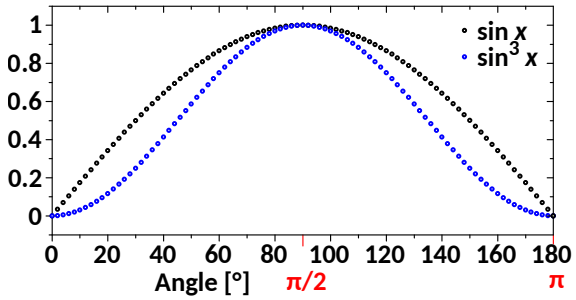

Figure A4 Comparison between the $\sin x$ (black) and the $\sin^3 x$ (function) between $x = 0$ and $x = \pi$.

Bibliography

[1] M. Z. Hasan and C. L. Kane. *Colloquium* : Topological insulators. *Rev. Mod. Phys.*, 82:3045–3067, Nov 2010. doi: 10.1103/RevModPhys.82.3045. URL `http://link.aps.org/doi/10.1103/RevModPhys.82.3045`.

[2] X.-L. Qi and S.-C. Zhang. Topological insulators and superconductors. *Rev. Mod. Phys.*, 83(4):1057, 2011.

[3] Y. Ando and L. Fu. Topological crystalline insulators and topological superconductors: from concepts to materials. *Annu. Rev. Condens. Matter Phys.*, 6(1):361–381, 2015.

[4] L. Fu and C. L. Kane. Topological insulators with inversion symmetry. *Phys. Rev. B*, 76:045302, Jul 2007. doi: 10.1103/PhysRevB.76.045302. URL `http://link.aps.org/doi/10.1103/PhysRevB.76.045302`.

[5] J. E. Moore and L. Balents. Topological invariants of time-reversal-invariant band structures. *Phys. Rev. B*, 75:121306, Mar 2007. doi: 10.1103/PhysRevB.75.121306. URL `http://link.aps.org/doi/10.1103/PhysRevB.75.121306`.

[6] R. Roy. Topological phases and the quantum spin Hall effect in three dimensions. *Phys. Rev. B*, 79:195322, May 2009. doi: 10.1103/PhysRevB.79.195322. URL `http://link.aps.org/doi/10.1103/PhysRevB.79.195322`.

[7] H. Zhang, C.-X. Liu, X.-L. Qi, Xi Dai, Z. Fang, and S.-C. Zhang. Topological insulators in Bi_2Se_3, Bi_2Te_3 and Sb_2Te_3 with a single Dirac cone on the surface. *Nature Physics*, 5(6):438–442, May 2009.

[8] D. Hsieh, D. Qian, L. Wray, YuQi Xia, Y. S. Hor, R. J. Cava, and M. Z. Hasan. A topological Dirac insulator in a quantum spin Hall phase. *Nature*, 452(7190):970, 2008.

[9] Y. Xia, D. Qian, D. Hsieh, L. Wray, A. Pal, H. Lin, A. Bansil, D. Grauer, Y. S. Hor, R. J. Cava, and M. Z. Hasan. Observation of a large-gap topological-

insulator class with a single Dirac cone on the surface. *Nature physics*, 5(6): 398, 2009. URL https://doi.org/10.1038/nphys1274.

[10] Y. L. Chen, J. G. Analytis, J.-H. Chu, Z. K. Liu, S.-K. Mo, X. L. Qi, H. J. Zhang, D. H. Lu, X. Dai, Z. Fang, S. C. Zhang, I. R. Fisher, Z. Hussain, and Z.-X. Shen. Experimental Realization of a Three-Dimensional Topological Insulator, Bi_2Te_3. *Science*, 325(5937):178–181, 2009. ISSN 0036-8075. doi: 10.1126/science.1173034. URL http://science.sciencemag.org/content/325/5937/178.

[11] D. Hsieh, Y. Xia, D. Qian, L. Wray, F. Meier, J. H. Dil, J. Osterwalder, L. Patthey, A. V. Fedorov, H. Lin, A. Bansil, D. Grauer, Y. S. Hor, R. J. Cava, and M. Z. Hasan. Observation of Time-Reversal-Protected Single-Dirac-Cone Topological-Insulator States in Bi_2Te_3 and Sb_2Te_3. *Phys. Rev. Lett.*, 103:146401, Sep 2009. doi: 10.1103/PhysRevLett.103.146401. URL https://link.aps.org/doi/10.1103/PhysRevLett.103.146401.

[12] Y. Ando. Topological Insulator Materials. *Journal of the Physical Society of Japan*, 82(10):102001, 2013. doi: 10.7566/JPSJ.82.102001. URL https://doi.org/10.7566/JPSJ.82.102001.

[13] Frank Wilczek. Majorana returns. *Nature Physics*, 5(9):614, 2009.

[14] B. Skinner, T. Chen, and B. I. Shklovskii. Why is the bulk resistivity of topological insulators so small? *Phys. Rev. Lett.*, 109:176801, Oct 2012. doi: 10.1103/PhysRevLett.109.176801. URL https://link.aps.org/doi/10.1103/PhysRevLett.109.176801.

[15] R. E. Taylor, B. Leung, M. P. Lake, and L.-S Bouchard. Spin–lattice relaxation in bismuth chalcogenides. *The Journal of Physical Chemistry C*, 116(32): 17300–17305, 2012.

[16] B.-Li Young, Z.-Yo Lai, Z. Xu, A. Yang, G. D. Gu, Z.-H. Pan, T. Valla, G. J. Shu, R. Sankar, and F. C. Chou. Probing the bulk electronic states of Bi_2Se_3 using nuclear magnetic resonance. *Physical Review B*, 86(7):075137, 2012.

[17] D. Koumoulis, T. C. Chasapis, R. E. Taylor, M. P. Lake, D. King, N. N. Jarenwattananon, G. A. Fiete, M. G. Kanatzidis, and L.-S. Bouchard. NMR probe of metallic states in nanoscale topological insulators. *Physical Review Letters*, 110(2):026602, 2013.

[18] D. M. Nisson, A. P. Dioguardi, P. Klavins, C. H. Lin, K. Shirer, A. C. Shockley, J. Crocker, and N. J. Curro. Nuclear magnetic resonance as a probe of electronic states of Bi_2Se_3. *Physical Review B*, 87(19):195202, 2013.

[19] D. Koumoulis, B. Leung, T. C. Chasapis, R. Taylor, D. King Jr., M. G. Kanatzidis, and L.-S. Bouchard. Understanding Bulk Defects in Topological Insulators from Nuclear-Spin Interactions. *Advanced Functional Materials*, 24 (11):1519–1528, 2014.

[20] D. M. Nisson, A. P. Dioguardi, X. Peng, D. Yu, and N. J. Curro. Anomalous nuclear magnetic resonance spectra in Bi_2Se_3 nanowires. *Phys. Rev. B*, 90(12): 125121, September 2014.

[21] S. Mukhopadhyay, S. Krämer, H. Mayaffre, H. F. Legg, M. Orlita, C. Berthier, M. Horvatić, G. Martinez, M. Potemski, B. A. Piot, et al. Hyperfine coupling and spin polarization in the bulk of the topological insulator Bi_2Se_3. *Physical Review B*, 91(8):081105, 2015.

[22] D. Yu. Podorozhkin, E. V. Charnaya, A. Antonenko, R. Mukhamad'yarov, V. V. Marchenkov, S. V. Naumov, J. C. A. Huang, H. W. Weber, and A. S. Bugaev. Nuclear magnetic resonance study of a Bi_2Te_3 topological insulator. *Physics of the Solid State*, 57(9):1741–1745, 2015.

[23] N. M. Georgieva, D. Rybicki, R. Guehne, G. V. M. Williams, S. V. Chong, K. Kadowaki, Ion Garate, and J. Haase. ^{77}Se nuclear magnetic resonance of topological insulator Bi_2Se_3. *Physical Review B*, 93(19):195120, 2016.

[24] K. Matano, M. Kriener, K. Segawa, Y. Ando, and Guo-qing Zheng. Spin-rotation symmetry breaking in the superconducting state of $Cu_xBi_2Se_3$. *Nature Physics*, 12(9):852, 2016.

[25] E. M. Levin, T. M. Riedemann, A. Howard, Na H. Jo, S. L Bud'ko, P. C. Canfield, and Thomas A. Lograsso. ^{125}Te NMR and Seebeck effect in Bi_2Te_3 synthesized from stoichiometric and Te-rich melts. *The Journal of Physical Chemistry C*, 120(44):25196–25202, 2016.

[26] A. O. Antonenko, E. V. Charnaya, D. Yu. Nefedov, D. Yu. Podorozhkin, A. V. Uskov, A. S. Bugaev, M. K. Lee, L. J. Chang, S. V. Naumov, Yu. A. Perevozchikova, et al. NMR studies of single crystals of the topological insulator Bi_2Te_3 at low temperatures. *Physics of the Solid State*, 59(5):855–859, 2017.

[27] A. O. Antonenko, E. V. Charnaya, D. Yu. Nefedov, D. Yu. Podorozhkin, A. V. Uskov, A. S. Bugaev, M. K. Lee, L. J. Chang, S. V. Naumov, Yu. A. Perevozchikova, et al. NMR study of topological insulator Bi_2Te_3 in a wide temperature range. *Physics of the Solid State*, 59(12):2331–2339, 2017.

[28] D. M. Choi and C. E. Lee. ^{77}Se Nuclear Magnetic Resonance Study of the Surface Effect in Topological Insulator Bi_2Se_3 Nanoparticles. *J. Korean Phys. Soc.*, 72(7):835–837, April 2018.

[29] D. M. Choi, K. W. Lee, and C. E. Lee. ^{125}Te nuclear magnetic resonance and impedance spectroscopy study of topological insulator Bi_2Te_3 nanoparticles mixed with insulating Al_2O_3 nanoparticles. *Materials Research Express*, 2018. URL `http://iopscience.iop.org/10.1088/2053-1591/aaf524`.

[30] K. v. Klitzing, G. Dorda, and M. Pepper. New Method for High-Accuracy Determination of the Fine-Structure Constant Based on Quantized Hall Resistance. *Phys. Rev. Lett.*, 45:494–497, Aug 1980. doi: 10.1103/PhysRevLett.45.494. URL `https://link.aps.org/doi/10.1103/PhysRevLett.45.494`.

[31] E. Burstein, A. H. Macdonald, and P. J. Stiles. *Contemporary Concepts of Condensed Matter Science - Topological Insulators*. Elsevier B. V., 2013. ISBN 978-0-444-63314-9.

[32] B. Andrei Bernevig and Taylor L. Hughes. *Topological insulators and topological superconductors*. Princeton University Press, 2013. ISBN 978-0-691-15175-5.

[33] S.-Q. Shen. *Topological Insulators - Dirac Equation in Condensed Matter*. Springer Nature Singapore Pre Ltd., 2nd edition, 2017. ISBN 978-981-10-4606-3.

[34] D. J. Thouless, M. Kohmoto, M. P. Nightingale, and M. den Nijs. Quantized Hall Conductance in a Two-Dimensional Periodic Potential. *Phys. Rev. Lett.*, 49:405–408, Aug 1982. doi: 10.1103/PhysRevLett.49.405. URL `https://link.aps.org/doi/10.1103/PhysRevLett.49.405`.

[35] Y. K. Kato, R. C. Myers, A. C. Gossard, and D. D. Awschalom. Observation of the Spin Hall Effect in Semiconductors. *Science*, 306(5703): 1910–1913, 2004. ISSN 0036-8075. doi: 10.1126/science.1105514. URL `http://science.sciencemag.org/content/306/5703/1910`.

[36] S. Murakami, N. Nagaosa, and S.-C. Zhang. Spin-Hall Insulator. *Phys. Rev. Lett.*, 93:156804, Oct 2004. doi: 10.1103/PhysRevLett.93.156804. URL https://link.aps.org/doi/10.1103/PhysRevLett.93.156804.

[37] C. L. Kane and E. J. Mele. Z_2 Topological Order and the Quantum Spin Hall Effect. *Phys. Rev. Lett.*, 95:146802, Sep 2005. doi: 10.1103/PhysRevLett.95.146802. URL https://link.aps.org/doi/10.1103/PhysRevLett.95.146802.

[38] C. L. Kane and E. J. Mele. Quantum Spin Hall Effect in Graphene. *Phys. Rev. Lett.*, 95:226801, Nov 2005. doi: 10.1103/PhysRevLett.95.226801. URL https://link.aps.org/doi/10.1103/PhysRevLett.95.226801.

[39] B. A. Bernevig and S.-C. Zhang. Quantum Spin Hall Effect. *Phys. Rev. Lett.*, 96:106802, Mar 2006. doi: 10.1103/PhysRevLett.96.106802. URL https://link.aps.org/doi/10.1103/PhysRevLett.96.106802.

[40] B. A. Bernevig, T. L. Hughes, and S.-C. Zhang. Quantum Spin Hall Effect and Topological Phase Transition in HgTe Quantum Wells. *Science*, 314(5806): 1757–1761, 2006. ISSN 0036-8075. doi: 10.1126/science.1133734. URL http://science.sciencemag.org/content/314/5806/1757.

[41] M. König, S. Wiedmann, C. Brüne, A. Roth, H. Buhmann, L. W. Molenkamp, X.-L. Qi, and S.-C. Zhang. Quantum Spin Hall Insulator State in HgTe Quantum Wells. *Science*, 318(5851):766–770, 2007. ISSN 0036-8075. doi: 10.1126/science.1148047. URL http://science.sciencemag.org/content/318/5851/766.

[42] L. Fu and C. L. Kane. Topological insulators with inversion symmetry. *Phys. Rev. B*, 76:045302, Jul 2007. doi: 10.1103/PhysRevB.76.045302. URL https://link.aps.org/doi/10.1103/PhysRevB.76.045302.

[43] R. J. Cava, Huiwen Ji, M. K. Fuccillo, Q. D. Gibson, and Y. S. Hor. Crystal structure and chemistry of topological insulators. *J. Mater. Chem. C*, 1:3176–3189, 2013. doi: 10.1039/C3TC30186A. URL http://dx.doi.org/10.1039/C3TC30186A.

[44] T. R. Devidas, E. P. Amaladass, Shilpam Sharma, R. Rajaraman, D. Sornadurai, N. Subramanian, Awadhesh Mani, C. S. Sundar, and A. Bharathi. Role of Se vacancies on Shubnikov-de Haas oscillations in Bi_2Se_3: A combined magneto-resistance and positron annihilation study. *EPL (Europhysics*

Letters), 108(6):67008, dec 2014. doi: 10.1209/0295-5075/108/67008. URL https://doi.org/10.1209%2F0295-5075%2F108%2F67008.

[45] F.-T. Huang, M.-W. Chu, H. H. Kung, W. L. Lee, R. Sankar, S.-C. Liou, K. K. Wu, Y. K. Kuo, and F. C. Chou. Nonstoichiometric doping and bi antisite defect in single crystal bi_2se_3. *Phys. Rev. B*, 86:081104, Aug 2012. doi: 10.1103/PhysRevB.86.081104. URL https://link.aps.org/doi/10.1103/PhysRevB.86.081104.

[46] C. B. Satterthwaite and R. W. Ure. Electrical and thermal properties of bi_2 te_3. *Phys. Rev.*, 108:1164–1170, Dec 1957. doi: 10.1103/PhysRev.108.1164. URL https://link.aps.org/doi/10.1103/PhysRev.108.1164.

[47] J. P. Fleurial, L. Gailliard, R. Triboulet, H. Scherrer, and S. Scherrer. Thermal properties of high quality single crystals of bismuth telluride—Part I: Experimental characterization. *Journal of Physics and Chemistry of Solids*, 49(10):1237 – 1247, 1988. ISSN 0022-3697. doi: https://doi.org/10.1016/0022-3697(88)90182-5. URL http://www.sciencedirect.com/science/article/pii/0022369788901825.

[48] Y. S. Hor, D. Qu, N. P. Ong, and R. J. Cava. Low temperature magnetothermoelectric effect and magnetoresistance in Te vapor annealed Bi_2Te_3. *Journal of Physics: Condensed Matter*, 22(37):375801, aug 2010. doi: 10.1088/0953-8984/22/37/375801. URL https://doi.org/10.1088%2F0953-8984%2F22%2F37%2F375801.

[49] Y. S. Hor, A. Richardella, P. Roushan, Y. Xia, J. G. Checkelsky, A. Yazdani, M. Z. Hasan, N. P. Ong, and R. J. Cava. p-type Bi_2Se_3 for topological insulator and low-temperature thermoelectric applications. *Phys. Rev. B*, 79:195208, May 2009. doi: 10.1103/PhysRevB.79.195208. URL https://link.aps.org/doi/10.1103/PhysRevB.79.195208.

[50] S. K. Kushwaha, I. Pletikosić, T. Liang, A. Gyenis, S. H. Lapidus, Yao Tian, He Zhao, K. S. Burch, Jingjing Lin, Huiwen J Wang, Wudi and, A. V. Fedorov, Ali Yazdani, N. P. Ong, T. Valla, and R. J. Cava. Sn-doped $Bi_{1.1}Sb_{0.9}Te_2S$ bulk crystal topological insulator with excellent properties. *Nature communications*, 7:11456, 2016.

[51] S.V. Chong, G.V.M. Williams, and R.L. Moody. The effect of manganese incorporation in Bi_2Se_3 on the thermal, electrical transport and magnetic

properties. *Journal of Alloys and Compounds*, 686:245 – 251, 2016. ISSN 0925-8388. doi: https://doi.org/10.1016/j.jallcom.2016.06.006. URL http://www.sciencedirect.com/science/article/pii/S0925838816317170.

[52] J. Choi, S. Choi, J. Choi, Y. Park, H.-M. Park, H.-W. Lee, B.-C. Woo, and S. Cho. Magnetic properties of Mn-doped Bi_2Te_3 and Sb_2Te_3. *physica status solidi (b)*, 241(7):1541–1544, 2004. doi: 10.1002/pssb.200304527. URL https://onlinelibrary.wiley.com/doi/abs/10.1002/pssb.200304527.

[53] C. Boulanger. Thermoelectric Material Electroplating: a Historical Review. *Journal of Electronic Materials*, 39(9):1818–1827, Sep 2010. ISSN 1543-186X. doi: 10.1007/s11664-010-1079-6. URL https://doi.org/10.1007/s11664-010-1079-6.

[54] H. Mamur, M. R. A. Bhuiyan, F. Korkmaz, and M. Nil. A review on bismuth telluride (Bi_2Te_3) nanostructure for thermoelectric applications. *Renewable and Sustainable Energy Reviews*, 82:4159 – 4169, 2018. ISSN 1364-0321. doi: https://doi.org/10.1016/j.rser.2017.10.112. URL http://www.sciencedirect.com/science/article/pii/S1364032117314855.

[55] S. X. Zhang, R. D. McDonald, A. Shekhter, Z. X. Bi, Y. Li, Q. X. Jia, and S. T. Picraux. Magneto-resistance up to 60 Tesla in topological insulator Bi_2Te_3 thin films. *Applied Physics Letters*, 101(20):202403, 2012. doi: 10.1063/1.4766739. URL https://doi.org/10.1063/1.4766739.

[56] A. Roy, S. Guchhait, S. Sonde, R. Dey, T. Pramanik, A. Rai, H. C. P. Movva, L. Colombo, and S. K. Banerjee. Two-dimensional weak anti-localization in Bi_2Te_3 thin film grown on $Si(111)-(7\times7)$ surface by molecular beam epitaxy. *Applied Physics Letters*, 102(16):163118, 2013. doi: 10.1063/1.4803018. URL https://doi.org/10.1063/1.4803018.

[57] R. Dey, T. Pramanik, A. Roy, A. Rai, S. Guchhait, S. Sonde, H. C. P. Movva, L. Colombo, L. F. Register, and S. K. Banerjee. Strong spin-orbit coupling and Zeeman spin splitting in angle dependent magnetoresistance of Bi_2Te_3. *Applied Physics Letters*, 104(22):223111, 2014. doi: 10.1063/1.4881721. URL https://doi.org/10.1063/1.4881721.

[58] J. Suh, K. M. Yu, D. Fu, X. Liu, F. Yang, J. Fan, D. J. Smith, Y.-H. Zhang, J. K. Furdyna, C. Dames, W. Walukiewicz, and J. Wu. Simultaneous Enhancement of Electrical Conductivity and Thermopower of Bi_2Te_3 by Multifunctionality of Native Defects. *Advanced Materials*, 27(24):3681–3686, 2015.

doi: 10.1002/adma.201501350. URL https://onlinelibrary.wiley.com/doi/abs/10.1002/adma.201501350.

[59] R. Sultana, P. Neha, R. Goyal, S. Patnaik, and V. P. S. Awana. Unusual non saturating giant magneto-resistance in single crystalline Bi_2Te_3 topological insulator. *Journal of Magnetism and Magnetic Materials*, 428: 213 – 218, 2017. ISSN 0304-8853. doi: https://doi.org/10.1016/j.jmmm.2016.12.011. URL http://www.sciencedirect.com/science/article/pii/S0304885316330086.

[60] Y. S. Hor, P. Roushan, H. Beidenkopf, J. Seo, D. Qu, J. G. Checkelsky, L. A. Wray, D. Hsieh, Y. Xia, S.-Y. Xu, D. Qian, M. Z. Hasan, N. P. Ong, A. Yazdani, and R. J. Cava. Development of ferromagnetism in the doped topological insulator $bi_{2-x}mn_xte_3$. *Phys. Rev. B*, 81:195203, May 2010. doi: 10.1103/PhysRevB.81.195203. URL https://link.aps.org/doi/10.1103/PhysRevB.81.195203.

[61] C. Niu, Y. Dai, M. Guo, W. Wei, Y. Ma, and B. Huang. Mn induced ferromagnetism and modulated topological surface states in bi_2te_3. *Applied Physics Letters*, 98(25):252502, 2011. doi: 10.1063/1.3601020. URL https://doi.org/10.1063/1.3601020.

[62] M. D. Watson, L. J. Collins-McIntyre, L. R. Shelford, A. I. Coldea, D. Prabhakaran, S. C. Speller, T. Mousavi, C. R. M. Grovenor, Z. Salman, S. R. Giblin, G. van der Laan, and T. Hesjedal. Study of the structural, electric and magnetic properties of Mn-doped Bi_2Te_3 single crystals. *New Journal of Physics*, 15(10):103016, oct 2013. doi: 10.1088/1367-2630/15/10/103016. URL https://doi.org/10.1088%2F1367-2630%2F15%2F10%2F103016.

[63] S. Zimmermann, F. Steckel, C. Hess, H. W. Ji, Y. S. Hor, R. J. Cava, B. Büchner, and V. Kataev. Spin dynamics and magnetic interactions of Mn dopants in the topological insulator Bi_2Te_3. *Phys. Rev. B*, 94:125205, Sep 2016. doi: 10.1103/PhysRevB.94.125205. URL https://link.aps.org/doi/10.1103/PhysRevB.94.125205.

[64] V. Sakhin, E. Kukovitskii, N. Garif'yanov, Yu. Talanov, and G. Teitel'baum. Inhomogeneous State of the Bi_2Te_3 Doped with Manganese. *Journal of Superconductivity and Novel Magnetism*, 30(1):63–67, Jan 2017. ISSN 1557-1947. doi: 10.1007/s10948-016-3801-y. URL https://doi.org/10.1007/s10948-016-3801-y.

[65] Yu. Talanov, V. Sakhin, E. Kukovitskii, N. Garif'yanov, and G. Teitel'baum. Magnetic Resonance Study of the Bi_2Te_3 Doped with Manganese. *Applied Magnetic Resonance*, 48(2):143–154, Feb 2017. ISSN 1613-7507. doi: 10.1007/s00723-016-0853-x. URL https://doi.org/10.1007/s00723-016-0853-x.

[66] V. Sakhin, E. Kukovitskii, N. Garifyanov, R. Khasanov, Yu. Talanov, and G. Teitel'baum. Local magnetic moments in the topological insulators. *Journal of Magnetism and Magnetic Materials*, 459:290 – 294, 2018. ISSN 0304-8853. doi: https://doi.org/10.1016/j.jmmm.2017.10.047. URL http://www.sciencedirect.com/science/article/pii/S0304885317321467. The selected papers of Seventh Moscow International Symposium on Magnetism (MISM-2017).

[67] M. A. Ruderman and C. Kittel. Indirect Exchange Coupling of Nuclear Magnetic Moments by Conduction Electrons. *Phys. Rev.*, 96:99–102, Oct 1954. doi: 10.1103/PhysRev.96.99. URL https://link.aps.org/doi/10.1103/PhysRev.96.99.

[68] T. Kasuya. A Theory of Metallic Ferro- and Antiferromagnetism on Zener's Model. *Progress of Theoretical Physics*, 16(1):45–57, 07 1956. ISSN 0033-068X. doi: 10.1143/PTP.16.45. URL https://dx.doi.org/10.1143/PTP.16.45.

[69] K. Yosida. Magnetic Properties of Cu-Mn Alloys. *Phys. Rev.*, 106:893–898, Jun 1957. doi: 10.1103/PhysRev.106.893. URL https://link.aps.org/doi/10.1103/PhysRev.106.893.

[70] J. S. Lee, A. Richardella, D. W. Rench, R. D. Fraleigh, T. C. Flanagan, J. A. Borchers, J. Tao, and N. Samarth. Ferromagnetism and spin-dependent transport in n-type Mn-doped bismuth telluride thin films. *Phys. Rev. B*, 89: 174425, May 2014. doi: 10.1103/PhysRevB.89.174425. URL https://link.aps.org/doi/10.1103/PhysRevB.89.174425.

[71] B. C. Chapler, K. W. Post, A. R. Richardella, J. S. Lee, J. Tao, N. Samarth, and D. N. Basov. Infrared electrodynamics and ferromagnetism in the topological semiconductors Bi_2Te_3 and Mn-doped Bi_2Te_3. *Phys. Rev. B*, 89:235308, Jun 2014. doi: 10.1103/PhysRevB.89.235308. URL https://link.aps.org/doi/10.1103/PhysRevB.89.235308.

[72] R. Růžička, O. Caha, V. Holý, H. Steiner, Volobuiev V., A. Ney, G. Bauer, T. Duchoň, K. Veltruská, I. Khalakhan, V. Matolín, E. F. Schwier, H. Iwasawa, K. Shimada, and G. Springholz. Structural and electronic properties

of manganese-doped Bi_2Te_3 epitaxial layers. *New Journal of Physics*, 17 (1):013028, jan 2015. doi: 10.1088/1367-2630/17/1/013028. URL https://doi.org/10.1088%2F1367-2630%2F17%2F1%2F013028.

[73] S. Hosokawa, J. R. Stellhorn, T. Matsushita, N. Happo, K. Kimura, K. Hayashi, Y. Ebisu, T. Ozaki, H. Ikemoto, H. Setoyama, T. Okajima, Y. Yoda, H. Ishii, Y.-Fa Liao, M. Kitaura, and M. Sasaki. Impurity position and lattice distortion in a Mn-doped Bi_2Te_3 topological insulator investigated by x-ray fluorescence holography and x-ray absorption fine structure. *Phys. Rev. B*, 96:214207, Dec 2017. doi: 10.1103/PhysRevB.96.214207. URL https://link.aps.org/doi/10.1103/PhysRevB.96.214207.

[74] J. Ramírez-Ruiz, C. Gauvin-Ndyae, and I. Garate, 2017. personal communication.

[75] N. Bloembergen and T. J. Rowland. Nuclear Spin Exchange in Solids: Tl^{203} and Tl^{205} Magnetic Resonance in Thallium and Thallic Oxide. *Phys. Rev.*, 97: 1679–1698, Mar 1955. doi: 10.1103/PhysRev.97.1679. URL https://link.aps.org/doi/10.1103/PhysRev.97.1679.

[76] S. Boutin, J. Ramírez-Ruiz, and I. Garate. Tight-binding theory of NMR shifts in topological insulators and. *Phys. Rev. B*, 94:115204, September 2016.

[77] N. W. Ashcroft and N. D. Mermin. *Solid State Physics*. Cengage Learning, 1976.

[78] A. M. Bratkovsky. Tunneling of electrons in conventional and half-metallic systems: Towards very large magnetoresistance. *Phys. Rev. B*, 56:2344–2347, Aug 1997. doi: 10.1103/PhysRevB.56.2344. URL https://link.aps.org/doi/10.1103/PhysRevB.56.2344.

[79] P. A. Grünberg. Nobel Lecture: From spin waves to giant magnetoresistance and beyond. *Rev. Mod. Phys.*, 80:1531–1540, Dec 2008. doi: 10.1103/RevModPhys.80.1531. URL https://link.aps.org/doi/10.1103/RevModPhys.80.1531.

[80] T. McGuire and R. Potter. Anisotropic magnetoresistance in ferromagnetic 3d alloys. *IEEE Transactions on Magnetics*, 11(4):1018–1038, July 1975. ISSN 0018-9464. doi: 10.1109/TMAG.1975.1058782.

[81] G. Bergmann. Weak localization in thin films: a time-of-flight experiment with conduction electrons. *Physics Reports*, 107(1):1 – 58, 1984. ISSN 0370-1573. doi: https://doi.org/10.1016/0370-1573(84)90103-0. URL http://www.sciencedirect.com/science/article/pii/0370157384901030.

[82] A. A Abrikosov. Quantum linear magnetoresistance. *Europhysics Letters (EPL)*, 49(6):789–793, mar 2000. doi: 10.1209/epl/i2000-00220-2. URL https://doi.org/10.1209%2Fepl%2Fi2000-00220-2.

[83] D. Freude and J. Haase. *Quadrupole Effects in Solid-State Nuclear Magnetic Resonance*, volume 29 of *Special Applications. NMR Basic Principles and Progress*, chapter 1, pages 1 – 90. Springer, Berlin, Heidelberg, 1993.

[84] J. H. Van Vleck. The Dipolar Broadening of Magnetic Resonance Lines in Crystals. *Phys. Rev.*, 74:1168–1183, Nov 1948. doi: 10.1103/PhysRev.74.1168. URL https://link.aps.org/doi/10.1103/PhysRev.74.1168.

[85] C. P. Slichter. *Principles of Magnetic Resonance*. SpringerVerlag, New York, 3rd edition, 1990.

[86] N. F. Ramsey and E. M. Purcell. Interactions between Nuclear Spins in Molecules. *Phys. Rev.*, 85:143–144, Jan 1952. doi: 10.1103/PhysRev.85.143. URL https://link.aps.org/doi/10.1103/PhysRev.85.143.

[87] N. F. Ramsey. Electron Coupled Interactions between Nuclear Spins in Molecules. *Phys. Rev.*, 91:303–307, Jul 1953. doi: 10.1103/PhysRev.91.303. URL https://link.aps.org/doi/10.1103/PhysRev.91.303.

[88] Pascal P. Man, Jacek Klinowski, Arlette Trokiner, Hélène Zanni, and Pierre Papon. Selective and non-selective nmr excitation of quadrupolar nuclei in the solid state. *Chemical Physics Letters*, 151(1):143 – 150, 1988. ISSN 0009-2614. doi: https://doi.org/10.1016/0009-2614(88)80085-X. URL http://www.sciencedirect.com/science/article/pii/000926148880085X.

[89] J. Haase, O. P. Sushkov, P. Horsch, and G. V. M. Williams. Planar Cu and O hole densities in high-T_c cuprates determined with NMR. *Phys. Rev. B*, 69:094504, Mar 2004. doi: 10.1103/PhysRevB.69.094504. URL https://link.aps.org/doi/10.1103/PhysRevB.69.094504.

[90] J. Van Kranendonk. Theory of quadrupolar nuclear spin-lattice relaxation. *Physica*, 20(7):781 – 800, 1954. ISSN 0031-8914. doi: https://doi.org/10.1016/

S0031-8914(54)80191-1. URL http://www.sciencedirect.com/science/article/pii/S0031891454801911.

[91] A. Suter, M. Mali, J. Roos, and D. Brinkmann. Mixed magnetic and quadrupolar relaxation in the presence of a dominant static Zeeman Hamiltonian. *Journal of Physics: Condensed Matter*, 10(26):5977–5994, jul 1998. doi: 10.1088/0953-8984/10/26/022. URL https://doi.org/10.1088%2F0953-8984%2F10%2F26%2F022.

[92] E. L. Hahn. Nuclear Induction Due to Free Larmor Precession. *Phys. Rev.*, 77:297–298, Jan 1950. doi: 10.1103/PhysRev.77.297.2. URL https://link.aps.org/doi/10.1103/PhysRev.77.297.2.

[93] E. L. Hahn. Spin echoes. *Phys. Rev.*, 80:580–594, Nov 1950. doi: 10.1103/PhysRev.80.580. URL https://link.aps.org/doi/10.1103/PhysRev.80.580.

[94] J. Haase and E. Oldfield. Spin-Echo Behavior of Nonintegral-Spin Quadrupolar Nuclei in Inorganic Solids. *J. Magn. Reson. Ser. A*, 101(1):30–40, January 1993.

[95] J.G. Powles and P. Mansfield. Double-pulse nuclear-resonance transients in solids. *Physics Letters*, 2(2):58 – 59, 1962. ISSN 0031-9163. doi: https://doi.org/10.1016/0031-9163(62)90147-6. URL http://www.sciencedirect.com/science/article/pii/0031916362901476.

[96] P. Mansfield. Multiple-Pulse Nuclear Magnetic Resonance Transients in Solids. *Phys. Rev.*, 137:A961–A974, Feb 1965. doi: 10.1103/PhysRev.137.A961. URL https://link.aps.org/doi/10.1103/PhysRev.137.A961.

[97] J. Haase, D. Freude, H. Pfeifer, E. Lippmaa, and P. Sarv. Two-pulse free induction decay quadrupole nmr. *Chemical Physics Letters*, 152(2):254 – 257, 1988. ISSN 0009-2614. doi: https://doi.org/10.1016/0009-2614(88)87363-9. URL http://www.sciencedirect.com/science/article/pii/0009261488873639.

[98] R. K. Harris, E. D. Becker, S. M. C. De Menezes, P. Granger, R. E. Hoffman, and K. W. Zilm. Further Conventions for NMR Shielding and Chemical Shifts (IUPAC Recommendations 2008). *Magnetic Resonance in Chemistry*, 46(6):582–598, 2008. doi: 10.1002/mrc.2225. URL https://onlinelibrary.wiley.com/doi/abs/10.1002/mrc.2225.

[99] O. Lutz, H. Oehler, and P. Kroneck. 63cu and65cu fourier transform nuclear magnetic resonance studies. *Zeitschrift für Physik A Atoms and Nuclei*, 288 (1):17–21, Mar 1978. ISSN 0939-7922. doi: 10.1007/BF01408195. URL https://doi.org/10.1007/BF01408195.

[100] O. Lutz, H. Oehler, and P. Kroneck. Chemical Shifts and Coupling Constants in Copper (I)-Compounds by 63Cu and 65Cu FT-NMR Studies. *Zeitschrift für Naturforschung A*, 33(9):1021–1024, 1978.

[101] V. N. Antonov, L. V. Bekenov, S. Uba, and A. Ernst. Electronic structure and x-ray magnetic circular dichroism in Mn-doped topological insulators Bi_2Se_3 and Bi_2Te_3. *Phys. Rev. B*, 96:224434, Dec 2017. doi: 10.1103/PhysRevB.96.224434. URL https://link.aps.org/doi/10.1103/PhysRevB.96.224434.

[102] Xiaolin Wang, Yi Du, Shixue Dou, and Chao Zhang. Room Temperature Giant and Linear Magnetoresistance in Topological Insulator Bi_2Te_3 Nanosheets. *Phys. Rev. Lett.*, 108:266806, Jun 2012. doi: 10.1103/PhysRevLett.108.266806. URL https://link.aps.org/doi/10.1103/PhysRevLett.108.266806.

[103] M. M. Parish and P. B. Littlewood. Classical magnetotransport of inhomogeneous conductors. *Phys. Rev. B*, 72:094417, Sep 2005. doi: 10.1103/PhysRevB.72.094417. URL https://link.aps.org/doi/10.1103/PhysRevB.72.094417.

[104] R. Guehne, V. Chlan, G. V.M. Williams, S. V. Chong, K. Kadowaki, A. Pöppl, and J. Haase. Unusual ^{209}Bi NMR quadrupole effects in topological insulator Bi_2Se_3. *Journal of Magnetic Resonance*, 302:34 – 42, 2019. ISSN 1090-7807. doi: https://doi.org/10.1016/j.jmr.2019.03.008. URL http://www.sciencedirect.com/science/article/pii/S1090780719300564.

[105] J. Haase, M. S. Conradi, C. Grey, and A. Vega. Population Transfers for NMR of Quadrupolar Spins in Solids. *J. Magn. Reson. Ser. A*, 109:90–97, 1994.

[106] B. Mallet and B. Buckley, 2019. personal communication.

[107] J. Bieroń and P. Pyykkö. Nuclear Quadrupole Moments of Bismuth. *Phys. Rev. Lett.*, 87(13):189–4, September 2001.

[108] H. Köhler and E. Wöchner. The g-factor of the conduction electrons in Bi_2Se_3. *physica status solidi (b)*, 67(2):665–675, 1975.

[109] A. Wolos, S. Szyszko, A. Drabinska, M. Kaminska, S. G. Strzelecka, A. Hruban, A. Materna, M. Piersa, J. Borysiuk, K. Sobczak, and M. Konczykowski. g-factors of conduction electrons and holes in Bi_2Se_3 three-dimensional topological insulator. *Physical Review B*, 93(1):155114, April 2016.